

**SEARCH FOR LIGHT NEUTRAL BOSONS IN THE TREK/E36
EXPERIMENT AT J-PARC**

A Dissertation
by
DONGWI HANDIIPONDOLA DONGWI

Submitted to the Graduate College of Hampton University in
partial fulfillment of the requirements for the degree of

DOCTOR OF PHILOSOPHY

August 2020

This dissertation submitted by Dongwi Handiipondola Dongwi in partial fulfillment of the requirements for the degree of Doctor of Philosophy at Hampton University, Hampton, Virginia is hereby approved by the committee under whom the work has been completed.

Michael Kohl, Ph.D.
Committee Chair

José L. Goity, Ph.D.

Michael Hasinoff, Ph.D.

Alberto Accardi, Ph.D.

Narbe Kalantarians, Ph.D.

Michelle Penn-Marshall, Ph.D.
Dean, The Graduate College

Date

Copyright by
DONGWI HANDIPONDOLA DONGWI
2020

ABSTRACT

Search for Light Neutral Bosons in the TREK/E36 Experiment at J-PARC

(August 2020)

Dongwi Handiipondola Dongwi, B.A., Westminster College;

Ph.D. Hampton University

Chair of Advisory Committee: Dr. Michael Kohl

The Standard Model (SM) represents our best description of the subatomic world and has been very successful in explaining how elementary particles interact under the influence of the fundamental forces. Despite its far reaching success in describing the building blocks of matter, the SM is still incomplete; falling short to explain dark matter, baryogenesis, neutrino masses and much more. The E36 experiment conducted at J-PARC in Japan, allows for sensitivity to search for light $U(1)$ gauge bosons, in the muonic K^+ decay channel. Such $U(1)$ bosons could be associated with dark matter or explain established muon-related anomalies such as the muon $g - 2$ value, and perhaps the proton radius puzzle. A realistic simulation study was employed for these rare searches in a mass range of 20 MeV to 100 MeV. Currently, about $\sim 8\%$ of the data has been analyzed and upper limits for the A' branching ratio $\mathcal{Br}(A')$ have been extracted at 95% CL.

Dedicated to my parents.

ACKNOWLEDGEMENTS

This dissertation is the culmination of many years of hard work and strenuous effort. I would like to sincerely thank my collaborators and everyone, who in one way or another, has contributed to my doctoral degree.

Firstly, I want to express my most sincere gratitude to my advisor Dr. Michael Kohl for his endless support, patience, motivation, and constructive criticism. Under his tutelage, I have accrued a wealth of knowledge in terms of problem solving, data analysis and how to present scientific results in an academic setting. Without his supervision, I would not have achieved this important milestone in my academic career. Additionally, I am also indebted to my Ph.D. committee members: Dr. Goity, Dr. Hasinoff, Dr. Accardi and Dr. Kalantarians, for their careful reading and criticism of the manuscript. I would also like to thank the Hampton University Graduate College: Dr. Penn-Marshall and Ms. Cansler for their support and correspondence.

I would also like to thank the entire Hampton University Physics Department, as well as the following individuals: Dr. Gueye (fmr. chair), Ms. Monique Howard (fmr. secretary), Ms. Rashinda Morris (fmr. secretary) and Ms. Edna Hogan Hilton for all their support regarding administrative tasks especially enabling me to comfortably perform my tasks while in Japan. I cannot forget the MK group: Dr. Tongtong Cao, Dr. Peter Monaghan, Dr. Ishara Fernando, Dr. Thir Gautham, Mr. Malinga Rathnayake, Ms. Sahara Nazeer, Ms. Tanvi Patel, Ms. Angel Christopher and Mr. Letrell Harris, who have been a great source of support and provided a vibrant environment to exchange ideas.

I am indebted to the HU International Office, both current and former staff members: Ms. Ebony Majeed, Mrs. Leah Pfitzinger, Dr. Francisco Coronel, Mr. Nikola Mundzic, Ms. Laura Tanganelli, Ms. Angel Boyd, Samaria Haysbert and especially Mrs. Georgiana Lau for her support and kindness. I would also like to express my

most sincere and heartfelt gratitude to the KEK and J-PARC User's Office representatives: Ms. K. Shimomura, Ai Sanao, K. Yamaguchi, and A. Kuniyasu for making my transition to living in Japan smooth. Additionally, I would like to thank J. Beanblossom, Tomioka-san, Dr. T. Kobayashi, Dr. T. Komatsubara, Dr. M. Sekine, Y. Isozaki, T. Isozaki, Ryosuke Isozaki, Ms. M. Sakamoto, Ms. C. Fujita, Sakata-san, Ms. Noriko Ouchi and Ouchi-san, and many more, who have welcomed me to Japan and have truly been and continue to be an incredible support system for me.

I am grateful to the unconditional support of Jack Segal, Walter Kellner and Sylvia, Debaditya Biswas, Anuruddha Rathnayake, Gray Nelson, Rodney, Dan, Tandi, Patrick and Shandi Rozzell, Pong and Mark and Barbara Walls, they have truly provided me with strong support system. My undying gratitude to Narbe, Stephanie and Emmit Kalantarians cannot be overstated, because they have often provided respite during very stressful periods and have opened their doors to me. I would like to extend my most sincere gratitude to Dr. Brad Sawatzky and Dr. Douglas Higinbotham for their creative insights and for helping me with the development of the simulation code. Additionally I cannot overstate the gratitude I have for Dr. Jun Imazato, who has been a great mentor for me while in Japan and for his enthusiastic support.

I am most grateful to the unconditional love and support of my brother and best friend Dr. Eyob Sebsibe Demeke, with whom I have been joined at the hip since high school, and has been a voice of encouragement throughout my graduate school career.

Finally I would like to thank my entire family, my parent and siblings: Absalom, Hafeni, Megameno, Diimineni, Beata, Lineekela, Emma, Karin, Fillemon, Iyaloo, Shetu, Lavinia and Jeremia, who have truly supported and believed in me, I would not have made it this far without them. I would like to extend a special thanks my aunt and uncle, Monica and Thomas Dongwi, who have raised and supported me.

This work has been supported by DOE awards DE-SC0003884 and DE-SC0013941.

TABLE OF CONTENTS

Chapter	Page
ABSTRACT	iv
DEDICATION	v
ACKNOWLEDGEMENTS	vi
TABLE OF CONTENTS	viii
LIST OF TABLES	xii
LIST OF FIGURES	xiii
1 Introduction	1
2 Physics Motivation	5
3 Literature Review	9
3.1 Dark Matter from Cosmology	9
3.1.1 Rotation Curves	9
3.1.2 Gravitational Lensing	11
3.1.3 Bullet Cluster	13
3.1.4 Cosmic Microwave Background (CMB)	14
3.1.5 Positron Excess	16
3.2 Particle Physics Anomalies	18
3.2.1 The Muon Magnetic Moment	19
3.2.2 The ${}^8\text{Be}$ Decay: Protophobic Photon	20
3.2.3 The Proton Radius Puzzle	22

Chapter	Page
3.3 New Physics Models	25
4 Experiment Setup and Commissioning	31
4.1 Overview	31
4.2 Beamline	33
4.3 Beam Collimation	34
4.4 Central Detector System	35
4.4.1 Central Detector: Target	36
4.4.2 Central Detector: Spiral Fiber Tracker	37
4.4.3 Central Detector: TOF1 & TOF2	39
4.4.4 Central Detector: Aerogel Čerenkov	40
4.4.5 Central Detector: CsI(Tl)	42
4.5 Spectrometer	45
4.6 Gap Veto Counters	47
4.7 Tracking Detectors	47
4.8 Lead-Glass Counters	48
5 Geant4 Geometry	51
5.1 Central Detector System	54
5.1.1 Central Detector: Target	54
5.1.2 Central Detector: TOF1	58
5.1.3 Central Detector: AC and AC mirror	58
5.2 Geant4 Verification	60
5.2.1 Propagation and Magnetic Field	60
5.2.2 Multiple Scattering	65
5.2.3 Energy Loss	69

Chapter	Page
6 Calibration and Data Analysis	76
6.1 Overview	76
6.2 Cooker Framework	76
6.3 Calorimeter Calibration	80
6.3.1 CsI Timing Study	87
6.3.2 Cluster Analysis: Overview	92
6.3.3 Cluster Analysis: $K_{\pi 2}$ Evaluation	92
7 Results and Conclusion	101
7.1 Acceptance and N_K Determination	102
7.2 Light Neutral Boson A' Signal Search	105
7.3 Conclusion and Outlook	112
REFERENCES	115
APPENDIX	128
A Author's Contributions To TREK/E36	130
B Detector Installation and Commissioning	132
B.1 Installation Day 1	133
B.2 Installation Day 2	133
B.3 Installation Day 3	136
B.4 Installation Day 4	136
B.5 Installation Day 5	138
B.6 Installation Day 6	140
B.7 Installation Day 7	142
B.8 Installation Day 8	144

Chapter	Page
B.9 Installation Day 9	144
B.10 Installation Day 10	146
B.11 Installation Day 11	146
B.12 Installation Day 12	149
VITA	152

LIST OF TABLES

Table	Page
1.1 Summary of R_K measurements	2
4.1 Parameters for the target array and WLS fibers	37
4.2 Main parameters for the SFT layers	39
4.3 Main parameters for the time-of-flight counters	40
4.4 Specifications of the CsI(Tl) photon detector	44
4.5 Parameters of planar C-tracking detectors	49
4.6 Parameters of the lead-glass counters	49
5.1 Central detector dimensions	60
6.1 Prominent K^+ decay modes	82
7.1 Data candidates and acceptance	102
7.2 The K^+ decay channels and the corresponding branching ratios .	103
7.3 The π^0 decay channels and corresponding branching ratios . . .	103
7.4 Acceptances and number of data events	110

LIST OF FIGURES

Figure	Page
2.1 Plausible new physics explanations for observed dark matter phenomena [23].	6
3.1 Rotation curves of galaxies. (a) Average velocities in the plane of the galaxy, as a function of the linear distance from the nucleus (kpc) [40]. (b) Rotation curve for galaxy NGC 6503 showing disk and gas contributions plus the dark matter halo contribution needed in order to match the data [22].	10
3.2 Gravitational lensing. On the left panel, the foreground cluster of galaxies gravitationally lenses the blue background galaxy seemingly creating multiple images. On the right is a computer reconstruction of the lens showing a smooth background component not accounted for when considering only the the mass of luminous objects [44].	12
3.3 The Bullet Cluster. A collision of galactic cluster showing baryonic matter in pink, separate from dark matter in blue, whose distribution was deduced from gravitational lensing [22, 45].	13
3.4 Mollweide map. A map of the cosmic microwave background created from WMAP data [42].	15
3.5 Power spectrum. Planck's power spectrum of temperature fluctuations in the cosmic microwave background. The anisotropy in fluctuations are shown at different angular scales on the sky. Here the red dots with error bars are the Planck data and the green curve shows the standard model of cosmology. The peak at 1 degree is consistent with a flat geometry of the universe, the height of the second peak with 5%, and the second and third peaks with 26% dark matter [42].	16
3.6 Positron and electron flux. Spectral indices of the electron flux γ_{e^-} and of the positron flux γ_{e^+} as a function of energy [47].	17
3.7 Energy regimes and possible mass ranges. Mass ranges for dark matter and mediator particle candidates and experimental anomalies.	18
3.8 One-loop magnetic moment correction.	20

Figure	Page
3.9 ${}^8\text{Be}$ angular measurement decays. Measured angular correlations (red) alongside previous measurements (blue) of the e^+e^- pairs originated from the decay of the 18.15 MeV ground state transition in ${}^8\text{Be}$. The black line represents the background, while the green one is the sum of the signal and background [72].	21
3.10 Invariant mass distribution for ${}^4\text{He}$ transition [74].	23
3.11 The proton charge radius r_p . The top panel. The recent PRad value [77] [H], is shown alongside other measurements of r_p obtain using various techniques: CODATA = [78]; [A] = [79]; [B] = [76]; [C] = [80]; [D] = [78]; [E] = [78]; [F] = [81]; [G] = [82]; [H] = [77]. The middle panel. Results were obtained from data in the following references: [77, 82] and [I] = [83] used the the Schlessinger Point Method (SPM) as described in [84–86]. The bottom panel. “SPM ep final” is the combined result from SPM extractions.	24
3.12 A' production amplitude. Feynman diagram showing the channel of interest $K^+ \rightarrow \mu^+\nu_\mu A'$ [48].	28
3.13 Mass limits on particles with scalar and pseudoscalar (a), and polar and axial vector (b) couplings due to constraints placed by $K^+ \rightarrow \mu X$ searches. The solid curve is the result for a single particle with both polar (scalar) and axial vector (pseudoscalar) couplings. In (a) the contributions of scalar coupling is represented by the dashed curve and the dash-dotted curve represents the pseudoscalar coupling. In (b) the dashed curve is the result for separate polar and axial vector particles with equal masses, and in both (a) and (b) the green region represents the experimental limit (horizontal line) [12].	29
3.14 Strong signal to background prediction. The QED background prediction for $K^+ \rightarrow \mu^+\nu e^+e^-$ (red dashed curve) and the prediction with a 30 MeV lepton universality violating A' of the Carlson model [16].	30
4.1 TREK/E36 apparatus. General cross-sectional and longitudinal views of the detector system.	31
4.2 Screenshot of the high voltage slow control graphical user interface.	33
4.3 Layout of the K1.1BR beamline. There was only a single electrostatic separator (ESS), the existence of a vertical focus (IFY) before the ESS played an important role in increasing the K/π ratio [1].	34

Figure	Page
4.4 TREK/E36 target. Highly segmented 256 scintillating fiber target bundle along with embedded wavelength shifting fibers in the SciFiber grooves.	36
4.5 SFT schema with only the 4th layer winding shown for simplicity. The cross-sectional view shows the all 4 layers of coiled ribbons with wedging	38
4.6 Cross-sectional drawing of the central detector perpendicular to the K^+ beam axis. The shaded region (blue) represents the aerogel radiator block. The AC counters were installed between the TOF1 counter and the inner wall of the CsI(Tl) calorimeter	41
4.7 Two aerogel counters with length of 178 mm, produced for the TREK/E36 experiment.	42
4.8 The highly segmented CsI(Tl) photon detector [20].	43
4.9 Side view of the toroidal magnet and lead glass wheel	45
4.10 Input toroidal geometry for TOSCA calculation of the magnetic field	46
4.11 Schematic view of the MWPC construction showing the cathode strip orientation with respect to the anode wires.	48
5.1 Data structure of the <i>e36g4MC</i> ROOT file. The leaves store the necessary information for each detector as needed by the user.	52
5.2 The TREK/E36 detector apparatus. The real TREK/E36 geometry (a) and the <i>e36g4MC</i> geometry using Geant4 (b).	53
5.3 The central detector system produced using the <i>e36g4MC</i> . The CsI barrel with all 768 crystals (a) and the geometry that sits inside the calorimeter (b).	55
5.4 The highly segmented target fibers. The real geometry of the TREK/E36 target (a) and (b) shows the <i>e36g4MC</i> target geometry and embedded WLS fibers.	56
5.5 Target support. The target and Al target support tube as well as the TOF1 counter.	57
5.6 TOF1 and wrapping material. A TOF1 counter and the additional polyethylene material demonstrating the accounting of the material budget within the <i>e36g4MC</i> geometries.	58

Figure	Page
5.7 The aerogel Čerenkov detector and the mirror. Mirror raised above above the AC (a) and placed neatly on to the AC (b). Due to the complicated nature of the AC mirror, the mirror was produced using a CAD program and that CAD file was imported into e36g4MC.	59
5.8 Kalman Filter algorithm [105,106]. A schematic view of the Kalman filter algorithm implementation in the TREK/E36 experiment, which shows a starting state vector point x_0 and propagating to the target and then using a smoother to improve the state vector positions for the various C tracking elements.	61
5.9 TOSCA generated field map.Three dimensional plot of the field map used in both e36g4MC and the tracking package.	62
5.10 Implementation of TOSCA field. Successful implementation of a TOSCA generated toroidal field in the e36g4MC toolkit.	63
5.11 <i>Geantino</i> state vector evaluation. The differences in state vector at C2 between the tracking package and the e36g4MC toolkit, evaluated with geantino simulated data. The top panel shows the differences of C2 position coordinates ($\Delta X, \Delta Y, \Delta Z$), and the bottom plane shows the differences of direction cosines ($\Delta NX, \Delta NY, \Delta NZ$). This result helped to establish that the propagation and treatment of the magnetic field in both packages are consistent.	64
5.12 Single Track. Single track event trajectory for the tracking package, dotted line, and e36g4MC, solid line. Both tracks used simulation data and the dotted line was reconstructed using simulation data and plotted from C2 to C4 tracking elements [109].	67
5.13 Physics comparison. State vector differences evaluated at C2 with $K_{\mu 2}$ muons, was carried out by studying the effects of turning various physics processes on and off: all physics turned on (red), multiple scattering turned off (blue) and only multiple scattering turned on (green), between the tracking package and the e36g4MC toolkit.	68
5.14 Geant4 energy loss. Stopping power ($-dE/dx$) for positive muons in copper as a function of $\beta\gamma = p/Mc$ over nine orders of magnitude in momentum. Solid curves indicate the total stopping power. Data below the break at $\beta\gamma \approx 0.1$ are taken from bands indicate boundaries between different approximations discussed in the text. The short dotted line labeled “ μ^- ” illustrate the “Barkas effect”, the dependence of stopping power on the projectile charge at very low energies [8].	70

Figure	Page
5.15 Energy loss in the e36g4MC. Comparison of energy loss due to only ionization (red) and energy loss due to both ionization and bremsstrahlung (blue). For heavy particles like μ^+ only energy due to ionization is considered thereby explaining the consistency between the red and blue histograms, because energy loss due to radiation is negligible.	71
5.16 C2 anode wires. Anode planes were replaced with anode wires in all the C tracking elements in order to correct for the discrepancy in energy loss between the tracking the package and the e36g4MC.	73
5.17 Energy loss correction. In (a) the energy loss discrepancy between the tracking package and the e36g4MC before the anode plane was replaced with anode wires in the e36g4MC. In (b) the energy loss correction after anode wires were used in the e36g4MC, and the energy loss has improved as a result.	75
6.1 Cooker structure overview showing directory hierarchy. Top level .h files are located in the <code>include</code> directory and the corresponding .cpp are located in the <code>src</code> directory.	77
6.2 The low-level CsI(Tl) plugin hierarchical structure.	78
6.3 High-level analysis plugin for the CsI.	79
6.4 CsI detector electronics block diagram.	81
6.5 Typical VF48 single pulse waveform with fitting function. The figure at the bottom is the % residual.	83
6.6 An example of a double pulse along with fitting function.	84
6.7 CsI(Tl) pulse height distribution	85
6.8 Energy loss in the central detector (CD) system as measured in the e36g4MC. The mean energy loss was calculated to be $\mu = 8.89$ MeV and $\sigma = 2.97$ MeV.	86
6.9 Incident energy dE of a $K_{\mu 2}$ muon (blue) upon striking a given CsI crystal. The cyan histogram T_μ is obtained after correcting for the energy lost by the muon as it traverses the central detector (CD) system.	88
6.10 Peak time distribution for select calibration runs (a) and production runs (b).	89

Figure	Page
6.11 Typical VF48 waveform and fit. The figure has been annotated with the variables used to perform the timing study.	90
6.12 CsI timing study using the CFD50. The top row shows the CFD50 for the reference channels as well as the differences between them: $CsI_{ref1} - CsI_{ref2}$ (blue), $CsI_{ref1} - CsI_{ref3}$ (gray) and $CsI_{ref2} - CsI_{ref3}$ (red)). The bottom row shows the CFD50 times of the signal channels, as well as the determined CsI time, by taking the differences between the three reference channels and the signal channels.	91
6.13 Two dimensional histograms depicting the relationship between the energy and the CFD50 time. In (a) we have single crystal events and a noticeable amplitude walk is observed, whilst in (b) we have select $K_{\mu 2}$ events and a more centralized amplitude is observed.	93
6.14 The μ^+ CFD50 time resolution corrected for the reference time T_0 . The time resolution was found to be $\sigma = 14.1318$ ns, by fitting a Gaussian.	94
6.15 CsI event viewer (a) showing various cluster distributions displayed using <code>visco</code> and the screen print (b) with angles evaluated in radians.	95
6.16 Flow charge showing the cluster algorithm for the CsI(Tl).	96
6.17 Momentum distribution for charged particle tracks, as analyzed by the toroidal spectrometer. The interval indicates a generous cut around the $K_{\pi 2}$ momentum.	97
6.18 Plots of total energy, invariant mass of 2γ clusters, opening angle of 2γ 's, $\cos(\theta_{\gamma\gamma})$, and opening angle of $\pi^+\pi^0 \cos(\theta_{\pi^+\pi^0}) \leq -.99$; where the blue histograms are the data and the red histograms are from the e36g4MC.	99
6.19 Plots of total energy, invariant mass of 2γ clusters, opening angle of 2γ 's, $\cos(\theta_{\gamma\gamma})$, and opening angle of $\pi^+\pi^0 \cos(\theta_{\pi^+\pi^0}) \leq -.99$. Better agreement between data and simulation was achieved by requiring that only a single TOF1 has registered a hit per event.	100
7.1 The acceptance (%) for assumed A' masses, demonstrating the low and high $m_{A'}$ yield suppression.	104
7.2 Mean values of e36g4MC reconstructed $m_{A'}$ as a function of assumed A' masses. The golden bands represent a $1\sigma_m(m_{A'})$ cut around the mean $m_{A'}$ values.	105

Figure	Page
7.3 TOF1 multiplicity (a) indicating the number of counters that registered a hit per event. Charged particle momentum distribution (b) under three cut conditions: good gap (blue); $K_{\pi 2}$ momentum region (green) and TOF1 multiplicity (red).	106
7.4 Invariant mass m_{ee} distributions under three cut conditions: good gap (blue); $K_{\pi 2}$ momentum region (green) and extra TOF1 (red).	108
7.5 The e36g4MC endpoint momentum distributions for assumed A' masses and the two prominent K^+ decays. The momentum spectrum of the data was used for the condition that at least 3 TOF1 counters had fired.	109
7.6 Upper limit of $Br(K^+ \rightarrow \mu^+ \nu A')$ under the condition that three TOF1 counters have fired.	110
7.7 Signal loss percentage as a function of assumed $m_{A'}$. The signal loss drops to zero at high A' masses as a result of kinematic suppression in the $K^+ \rightarrow \mu^+ \nu A'$ decay.	111
7.8 The invariant mass M_{ee} under the condition that at three TOF1 counters have registered a hit (red). The yellow histogram shows the M_{ee} once the endpoint momentum cut was applied, as a means of reducing the $K_{\mu 2}$ contamination.	112
7.9 Upper limit of $\mathcal{B}r(A')$ under the condition that three TOF1 counters have fired and a 230 MeV/c was applied.	113

CHAPTER 1

INTRODUCTION

The TREK/E36 experiment was conducted at the Japan Proton Accelerator Research Complex (J-PARC), with physics data-taking occurring from September to December 2015, and has been decommissioned as of March 2016. TREK/E36 was part of the TREK program at J-PARC, where TREK stands for Time Reversal Experiment with Stopped Kaons. The primary goal of the TREK/E36 experiment was to provide a high precision electroweak measurement in order to test lepton universality, which is expressed as an identical coupling constant of the charged lepton family (e , μ , and τ). Lepton universality is a staple of the Standard Model (SM) and any violation of this would be clear evidence of New Physics (NP) beyond the SM.

Data analysis of two-body leptonic decays of stopped kaons K_{l2} is currently being performed in order to provide a precise measurement of the decay width ratio $R_K = \Gamma(K^+ \rightarrow e^+\nu)/\Gamma(K^+ \rightarrow \mu^+\nu)$ to test lepton universality [1]. Due to the $V - A$ structure of charged current couplings, the ratio R_K is helicity-suppressed in the SM and is therefore sensitive to beyond SM physics [2]. The K_{l2} decay width is calculated as [1]

$$\Gamma(K_{l2}) = g_l^2 \frac{G^2}{8\pi} f_K^2 m_K m_l^2 \left(1 - \frac{m_l^2}{m_K^2}\right)^2 \quad (1.0.1)$$

where g_l is the coupling constant of the lepton current, G is the Fermi constant, f_K is the kaon form factor and m_K and m_l are the kaon and lepton masses respectively. The SM value for R_K is very precise because to a first approximation the strong interaction dynamics from equation 1.0.1 cancel [1, 3]

$$\begin{aligned}
R_K^{SM} &= \frac{\Gamma(K^+ \rightarrow e^+\nu)}{\Gamma(K^+ \rightarrow \mu^+\nu)} \\
&= \frac{m_e^2}{m_\mu^2} \left(\frac{m_K^2 - m_e^2}{m_K^2 - m_\mu^2} \right)^2 (1 + \delta_r) \\
&= (2.477 \pm 0.001) \times 10^{-5}
\end{aligned} \tag{1.0.2}$$

where δ_r represents radiative corrections, detailed calculations of which were carried out in [4]. Thus the SM value for R_K^{SM} has been calculated to high accuracy ($\Delta R_K/R_K \sim 0.4 \times 10^{-4}$) thereby making it possible to search for NP effects by conducting a precise measurement of R_K [3].

Experimental measurements of the ratio R_K were performed with KLOE [5] and NA62 [6, 7], both results are consistent with the SM value and are summarized in table 1.1 below. The PDG value of $2.488 \pm 0.009 \times 10^{-5}$ represents the world average.

Table 1.1

Summary of R_K measurements

Measurement	Kaon beam	$R_K (\times 10^{-5})$	$\Delta R_K/R_K$
PDG2018 [8]		2.488 ± 0.009	0.4%
NA62 [6]	In-flight K^\pm	$2.488 \pm 0.007 \pm 0.007$	0.4%
KLOE [5]	In-flight K^\pm	$2.493 \pm 0.025 \pm 0.019$	1.3%
TREK [1]	Stopped K^+		0.25%
SM [3]		2.477 ± 0.001	0.04%

TREK/E36 was designed to measure the ratio R_K with a total uncertainty of 0.25% using stopped kaons [1]. For this reason, TREK/E36 would be able to provide a complementary method to the in-flight decay measurements of KLOE and NA62 which are governed by different systematics.

Additionally, the TREK/E36 experiment is sensitive to by product searches for light neutral particles in exotic kaon decay modes of $K^+ \rightarrow \mu^+\nu A'$ and/or $K^+ \rightarrow \pi^+ A'$, followed by a prompt decay of $A' \rightarrow e^+e^-$. In this document the subject of discussion is centered around A' searches in the muonic channel, namely $K^+ \rightarrow \mu^+\nu A'$. This A' is often dubbed a dark photon, but could also be construed as a light neutral $U(1)$ boson, and might be a hidden force carrier of the dark sector associated with dark matter [9]. An A' that is weakly coupled to the SM and is sufficiently light could decay into observable di-lepton pairs, electron-positron pairs, which can be used to reconstruct its invariant mass. Furthermore, the A' could help resolve the proton radius puzzle [10–13]. Such hypothetic particles can also be conceived without violating existing constraints if they are fine-tuned and non-universally coupled [11–16]. In this case there would be a prediction of a strong observable signal in kaon decays, in particular in the calculable leptonic radiative mode $K^+ \rightarrow \mu^+\nu e^+e^-$ [12, 13].

TREK/E36 was set up and fully commissioned at the K1.1BR kaon beamline between the fall 2014 and spring 2015. Production data for the TREK/E36 experiment was completed by the end of 2015, which made use of an upgraded version of the KEK-PS E246 12-sector superconducting toroidal spectrometer used in a previous T-violation experiment via transverse muon polarization of muons in $K^+ \rightarrow \mu^+\nu\pi^0$ ($K_{\mu 3}$) decays at KEK [1, 17]. The TREK/E36 apparatus upgrade from E-246 consisted of:

- scintillating fiber target used to stop the incoming kaon beam had a smaller diameter to minimize multiple scattering and energy loss of the outgoing decay particles [1]
- addition of Spiral Fiber Tracker [1, 18]
- redundancy in particle ID systems used to distinguish between e and μ with high efficiency and low misidentification probability [1]
- faster readout electronics of the CsI(Tl) calorimeter with a pile-up capable data acquisition system using FPGA based waveform digitization [1, 19].

The incoming K^+ was tagged with a Fitch Čerenkov detector [1], in order to distinguish it from a π^+ , before stopping and decaying at rest in the active target, a matrix of 256 scintillating fibers oriented longitudinally along the beam, which determines the location of the kaon stop in the transverse plane. Surrounding the target was the a Spiral Fiber Tracker (SFT), which consisted of two pairs of fiber layers spiraling in *left/right* helicity and provided the z -coordinate of the outgoing decay particle(s) [18]. The target-SFT system was surrounded by 12 time-of-flight counter (TOF1) and 12 aerogel Čerenkov counters (AC) aligned with the 12 sectors of the toroidal spectrometer. This entire inner system is called the *Central Detector* system (CD).

A highly segmented and large acceptance CsI(Tl) calorimeter barrel which consisted of 768 crystal and covered about 75% of 4π [20] was used to identify and correct for structure dependent (SD) background events and also search for light neutral bosons A' . The calorimeter featured 12 holes (known as *muon holes*) aligned with the sectors of the spectrometer allowing for charged particles such as e^+ , μ^+ and π^+ to be tracked through 1 of the 12 toroidal magnet gaps, and momentum analyzed with Multi-Wire Proportional Chambers (MWPC) C2, C3 and C4. The A' search necessitated a charged particle tracked in the gap that has a vertex originating within the fiducial volume of the target (*good gap event*) and 2-clusters in the CsI calorimeter along with at least 3 TOF1 counters that registered a charged particle (ideally: e^+ , e^- and a good gap μ^+). At the exit of each magnet gap were sets of fast scintillator detectors (TTC and TOF2) and lead glass counters (PGCs) [21] that provided both trigger signals and e^+/μ^+ particle ID. The full suite of particle ID systems and tracking can also be deployed to suppress background events in the invariant mass spectrum when performing the A' search.

CHAPTER 2

PHYSICS MOTIVATION

At present our knowledge of the building blocks of matter is encompassed in the Standard Model (SM) of particle physics. While the SM has been successful in describing the physics of ordinary matter to high precision, in a wide variety of environments, and over a large energy range, it is nonetheless still incomplete. Particularly, the SM does not explain neutrino masses, the matter-antimatter asymmetry in the universe and dark matter; for which new physics must be responsible. Our best evidence for dark matter comes from cosmological and astrophysical measurements in many different contexts and over a wide range of scales. These scales range from the cosmic microwave background (CMB) power spectrum, to cluster and galactic rotation curves and gravitational lensing. There is no suitable SM particle that reconciles these cosmological observations and thus dark matter arguably represents a hint of physics beyond the Standard Model. The Standard Model of cosmology (often called the Concordance Model) states that the universe consists of 5% ordinary baryonic matter, $\sim 26\%$ dark matter (DM), and $\sim 69\%$ dark energy [22]. Unlocking the fundamental nature of dark matter (its cosmological origin, its constituents and their interactions) is one of the foremost open questions in elementary particle physics today, with tremendous potential to deepen our understanding of the fundamental laws of nature. This quest to unlock the particulate nature of dark matter has generated a great deal of enthusiasm in the community, bringing about vast and diverse schools of thought to explain the dark matter problem as summarized in figure 2.1.

It is the job of the particle physicist to interpret the gravitational impact of dark matter on cosmology and astrophysics, in terms of its identity and non-gravitational interactions; where terrestrial bench tests of these interpretations can be performed in particle accelerator experiments. That dark matter is a thermal relic from the hot



Figure 2.1. Plausible new physics explanations for observed dark matter phenomena [23].

early universe inspires the possibility that motivates non-gravitational interactions between dark and ordinary matter, hints of which were arguably seen by DAMA/LIBRA [24] and PAMELA [25] collaborations. Canonically, neutral weakly interacting massive particles (WIMPs $\mathcal{O}(\text{GeV})$) [26, 27] which arose as natural supersymmetric extensions of the Standard Model have been introduced to explain the relic abundance of dark matter. Setting WIMPs aside, much theoretical work has been undertaken to introduce new gauge forces existing in the MeV-GeV scale that could be due to a possible light mediator $U(1)$ between dark matter and ordinary matter [28–31].

Models of MeV-GeV mass scale dark matter coupled to the SM through a sub-GeV mediator [30–32] have been proposed to as possible explanations of the 511 keV emission [33] observed from the galactic center with annihilating dark matter [34]. Strikingly however, there are few model independent constraints on light, leptonically coupled mediators in the MeV-GeV mass range, Ref. [35] contains a good review.

A new $U(1)$ gauge boson A' was shown long ago to weakly mix with the kinetic terms of the SM hypercharge “kinetic mixing” in an extended Lagrangian [36]:

$$\mathcal{L} = \mathcal{L}_{SM} - \frac{1}{4}V_{\mu\nu}^2 + \frac{1}{2}m_{A'}^2 V_\mu^2 + \kappa V_\mu J_\mu^{EM} + \dots \quad (2.0.1)$$

where $V_{\mu\nu}$ is the field strengths of the A' and κ is the mixing angle parameter. The conservation of the electromagnetic current and the noticeable absence of any intrinsic parity/flavor/CP violation in the interaction of A' with the SM fermions can shield this force from very powerful symmetry tests. Given that astroparticle physics explanations for the positron excess and gamma ray burst being attributable to dark matter annihilation are rather speculative, additional motivation for new light gauge bosons is provided by the high energy and particle physics frontier as summarized in [37]. Additionally, there is also vigorous motivation to interpret various particle physics anomalies, chiefly the proton radius problem, the long-standing measurement of the anomalous magnetic moment of the muon and excited ${}^8\text{Be}$ decay in terms new light neutral mediators between dark matter and ordinary matter. There are two broad classes of dark sector models which are of current interest:

- *Hidden-Sector Dark Matter*: candidates are completely neutral under Standard Model forces, but interact through a new force, allowing for sub-GeV scale mediators [37]
- *Ultra-light Dark Matter* candidates have masses from 10^{-22} eV to about a keV, and can for example be produced during inflation or phase transitions in the very early Universe. The QCD axion dark matter is well motivated to solve the strong CP problem, which is an important milestone in coupling sensitivity as a function of mass [37]

Possible scenarios for hidden-sector dark matter include models that violate lepton universality [10], dark photon model with right-handed couplings to muons [38] and the Carlson model [12, 16] which includes vector and axial vector couplings to muons and protons in order to simultaneously explain proton radius puzzle and obey the constraints set by $(g - 2)_\mu$ discrepancy which have sizeable contributions in rare K -decays. In the TREK/E36 we are sensitive to these light neutral bosons in the mass range of $20 \text{ MeV}/c^2$ to $300 \text{ MeV}/c^2$, and can therefore probe the Carlson model which predicts a strong signal peak over a continuous background in the $K^+ \rightarrow \mu^+ \nu A'$ decay channel as will be discussed in 3.3. The analysis for upper limit extraction of the A' branching ratios $\mathcal{Br}(A')$, and the subsequent analysis of a peak search in the invariant mass are both model-independent.

CHAPTER 3

LITERATURE REVIEW

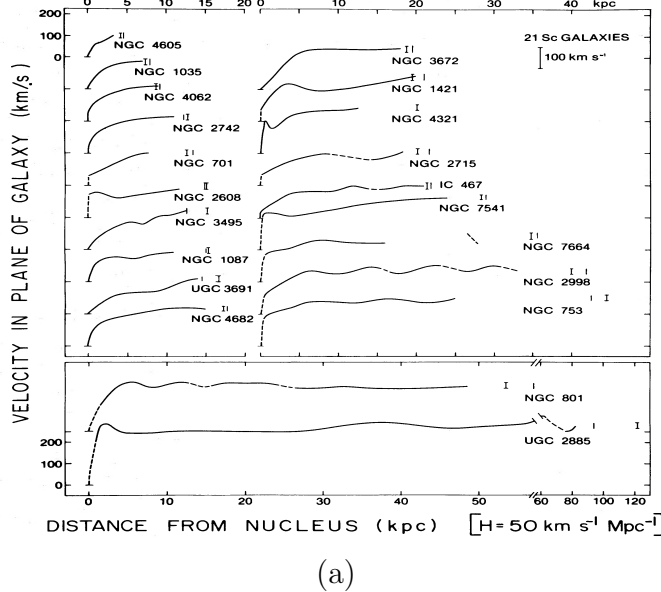
3.1 Dark Matter from Cosmology

The longest open problem in all of modern physics is perhaps the dark matter problem, which dates back to the work of Knut Lundmark, in Sweden and Fritz Zwicky, at Caltech, who coined the term “dark matter”. To date, our best hints of dark matter come from various cosmological and astrophysical measurements. Such measurements range from the cosmic microwave background (CMB) power spectrum to cluster and galactic rotation curves, and gravitational lensing. All of these data are quintessentially gravitational, and therefore tell us little directly about the particle nature of dark matter. A generic key property of dark matter in the Concordance Model is that it is cold, i.e. non relativistic at the epoch of structure formation, and with a free streaming length much smaller than the size of galaxies [23]. It follows then that there exists a large number of sub-dwarf galaxy dark structures in galactic halos [23]. If it is the case that dark matter is warm, or perhaps generally if its power spectrum is suppressed at small astrophysical scales, then it is possible to discern it by probing the actual number of substructures in the universe [22].

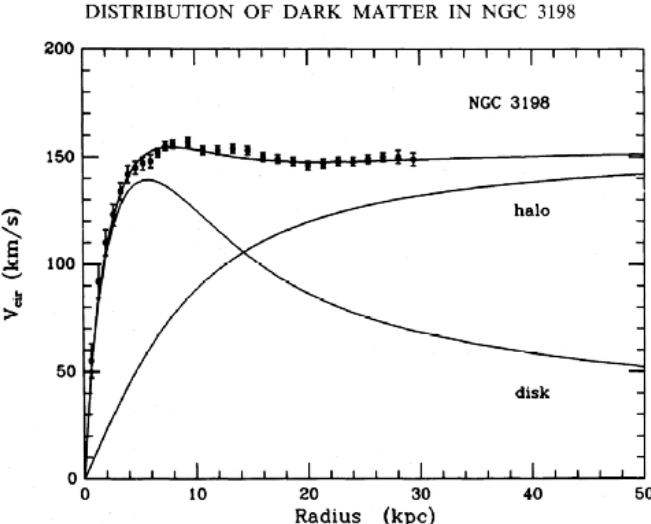
3.1.1 Rotation Curves

While studying the rotation curves of galaxies, Zwicky noticed that galaxies in the Coma Cluster were moving too rapidly and that the amount of stellar material in cluster could not mitigate this conundrum [39]. He thereby postulated that additional mass in the form of something dark, non-absorbing and non-luminescent, must be providing additional gravitational pull to speed up the orbits [39]. Subsequent work continued to find similar evidence, but the work of Ford and Rubin in the 1970’s

provided the breakthrough by showing that the same unexplained rapid orbits were found to exist in each galaxy [40] as shown in figure 3.1 (a).



(a)



(b)

Figure 3.1. Rotation curves of galaxies. (a) Average velocities in the plane of the galaxy, as a function of the linear distance from the nucleus (kpc) [40]. (b) Rotation curve for galaxy NGC 6503 showing disk and gas contributions plus the dark matter halo contribution needed in order to match the data [22].

Rotation curves of galaxies are flat, and as a result the scientific consensus for dark matter emerged. The velocities of objects (stars or gas) orbiting the centers of

galaxies, rather than decreasing as a function of the distance from the galactic centers as was expected, rather remain constant out to very large radii [40].

Similar observations of flat rotation curves have been found for all galaxies studied, including our Milky Way. A simple explanation for these results is that galaxies contain much more mass than can be explained by the luminous stellar objects residing in galactic disks [22]. It is this mass that provides the force to speed up the orbits. In order to explain the data, galaxies must have enormous dark halos made up of unknown dark matter. Current consensus in cosmology stipulates that more than 95% of the mass of galaxies consists of dark matter [41, 42]. Rotation curves are limited because one can only look out as far as there is light or neutral hydrogen (21 cm), namely to distances of tens of kpc [22]. This implies that although we can see the beginnings of dark matter haloes, we cannot trace where most of the dark matter is. One way to overcome these limitations are by lensing experiments which will be discussed in the following section.

3.1.2 Gravitational Lensing

Einstein’s theory of general relativity predicts that mass bends the space around it thereby bending or “lensing” light. Effects from lensing can be used to verify the existence of a mass even when it does not emit light. Through lensing measurements, the existence of enormous quantities of dark matter both in galaxies and in clusters of galaxies have been confirmed [22]. Observations are made of distant bright objects such as galaxies or quasars. As the result of intervening matter, the light from these distant objects is bent towards the regions of large mass [22]. As a result there may be multiple images of the distant objects and/or if these images cannot be individually resolved, the background object may appear brighter [43]. In some cases the images may appear to be distorted or sheared. The Sloan Digital Sky Survey used weak lensing (statistical studies of lensed galaxies) to conclude that galaxies, including the

Milky Way, are even larger and more massive than previously thought, and require even more dark matter out to great distances [43]. Again, the predominance of dark matter in galaxies was observed [43]. A good example of lensing is shown in the figure 3.2 below.

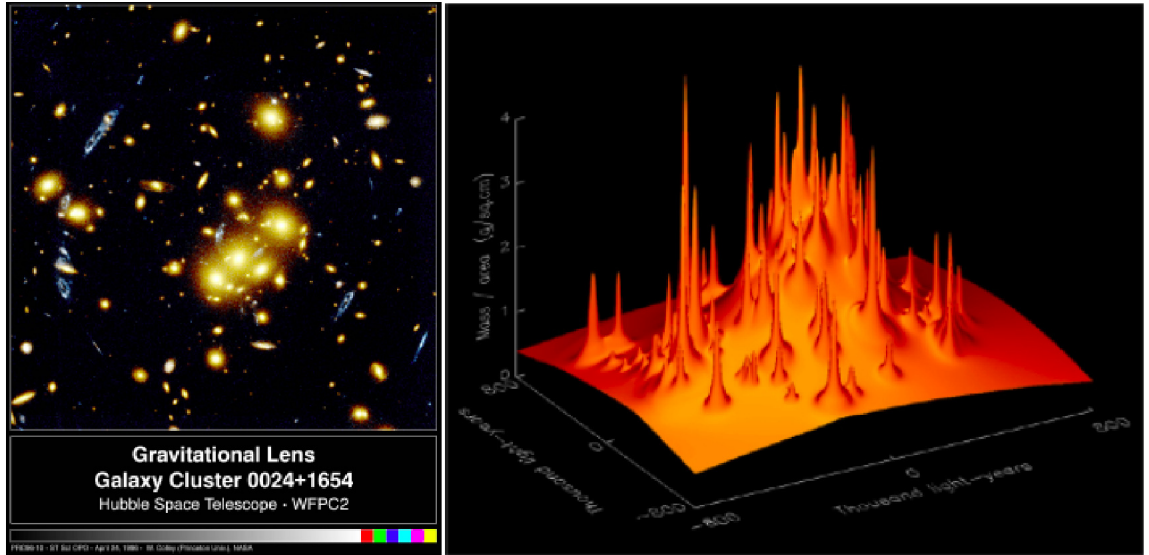


Figure 3.2. Gravitational lensing. On the left panel, the foreground cluster of galaxies gravitationally lenses the blue background galaxy seemingly creating multiple images. On the right is a computer reconstruction of the lense showing a smooth background component not accounted for when considering only the the mass of luminous objects [44].

In figure 3.2 the panel on the right shows a computer reconstruction of a foreground cluster inferred by lensing observations using the Hubble Space Telescope [44]. This cluster contains a wealth of many galaxies, which are indicated by the peaks in the figure. In addition to these galaxies, there is a noticeable smooth component, representing the dark matter contained in clusters in between the galaxies [44]. A major success of the lensing of dark matter to date is the evidence that dark matter has been observed out to much larger distances than could be probed by rotation curves: the dark matter has been seen in galaxies far out to 200 kpc from the centers of galaxies, in agreement with N-body simulations [22].

3.1.3 Bullet Cluster

The Bullet Cluster was formed from the collision of two smaller clusters. During the collision, the hot baryonic gas forming most of the clusters' mass was shocked and decelerated, while the galaxies in the clusters proceeded along ballistic trajectories [45]. Gravitational lensing indicates that most of the total mass also moved ballistically, thereby demonstrating that dark matter self-interactions are indeed weak. An image of the Bullet Cluster taken by the Chandra X-ray observatory is shown in figure 3.3 below. Shown in pink is baryonic matter; in blue is an image of the dark matter, deduced from gravitational lensing [22, 45].

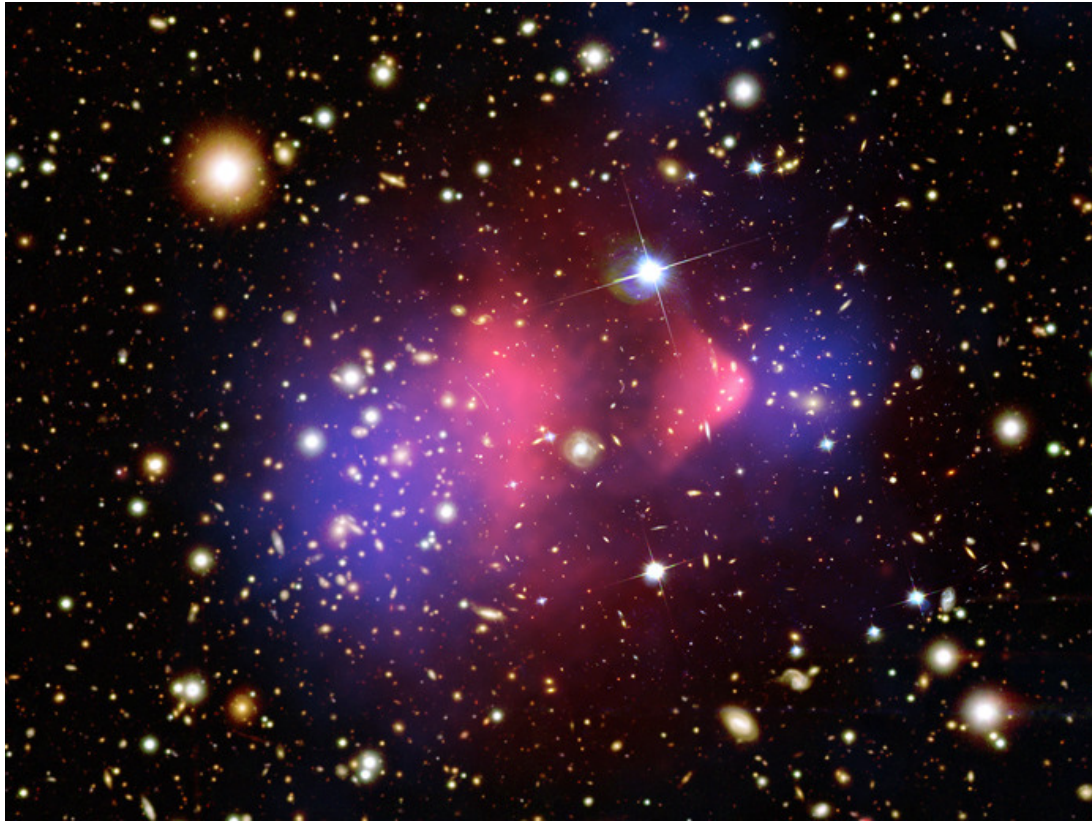


Figure 3.3. The Bullet Cluster. A collision of galactic cluster showing baryonic matter in pink, separate from dark matter in blue, whose distribution was deduced from gravitational lensing [22, 45].

During the merging process of the two smaller clusters, the dark matter had already passed through the collision point, while the baryonic matter was slowed down due to friction and coalesced to a single region at the center of the new cluster [22]. The evidence that most of the mass of galaxies and clusters is made of some unknown component of dark matter is overwhelming [22]. The next section covers the cosmic microwave background which contains a wealth of information about the early universe as well as irrefutable evidence for dark matter.

3.1.4 Cosmic Microwave Background (CMB)

Perhaps more concrete evidence for dark matter comes from measurements on cosmological scales of anisotropies in the cosmic microwave background. In short, the CMB is the remnant radiation from the hot early days of the universe. The photons decoupled from baryonic matter as electrons and protons formed neutral hydrogen, and continued to travel freely without interacting. As the universe continued to expand the wavelengths of these photons became larger and their energy became less, redshifting, falling into the microwave region of the electromagnetic spectrum [41, 42, 46].

Plank was a third generation space mission dedicated to measuring the temperature fluctuations of the CMB anisotropies. The early structure of the universe as seen in the anisotropy of the CMB temperature can be represented by an angular power spectrum, a plot that shows how the temperature pattern in the early universe varies with progressive measurements of smaller and smaller patches of the sky [41, 42, 46]. In turn, these measurements reveal the amount of energy emitted by different sized “ripples” of sound echoing through the early matter of the universe at given angles. The angular scale and height of the peaks (and troughs) of these oscillations provide powerful probes of cosmological parameters, including the total energy density,

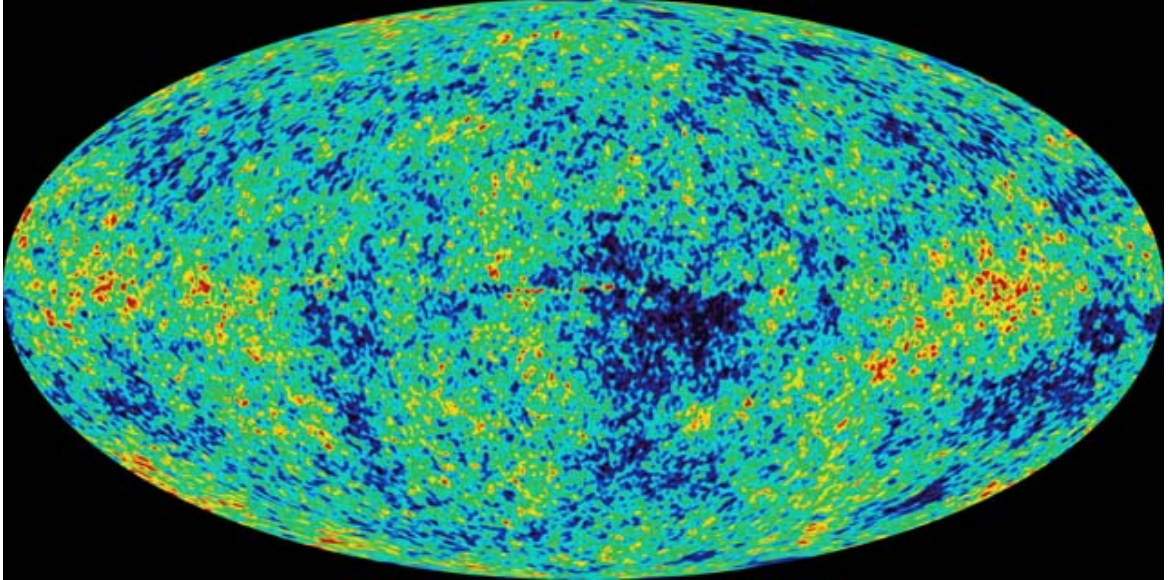


Figure 3.4. Mollweide map. A map of the cosmic microwave background created from WMAP data [42].

the baryonic fraction, and the dark matter component, as shown in the figure 3.5 below [46].

The sound horizon, which is the distance sound waves could have traveled in the time before the recombination epoch, at last scattering provides a ruler stick for the geometry of the universe: if the light travels in a straight line (as would be the case for a flat geometry), then the angular scale of the first Doppler peak was expected to be found at 1° ; this was indeed found to be correct [42, 46]. It can therefore be concluded that the geometry is flat, corresponding to an energy density of the universe of $\sim 10^{-29}$ gm/cm [42, 46]. The height of the second peak implies that 5% of the total is ordinary atoms, while matching all the peaks implies that 26% of the total is dark matter, leaving dark energy to account for the remainder of the energy of the universe [42, 46]. In truth the CMB as a single measurement already provides conclusive evidence for dark matter. Given this striking evidence for dark matter, we now turn to important implications of the nature of dark matter interactions and/or

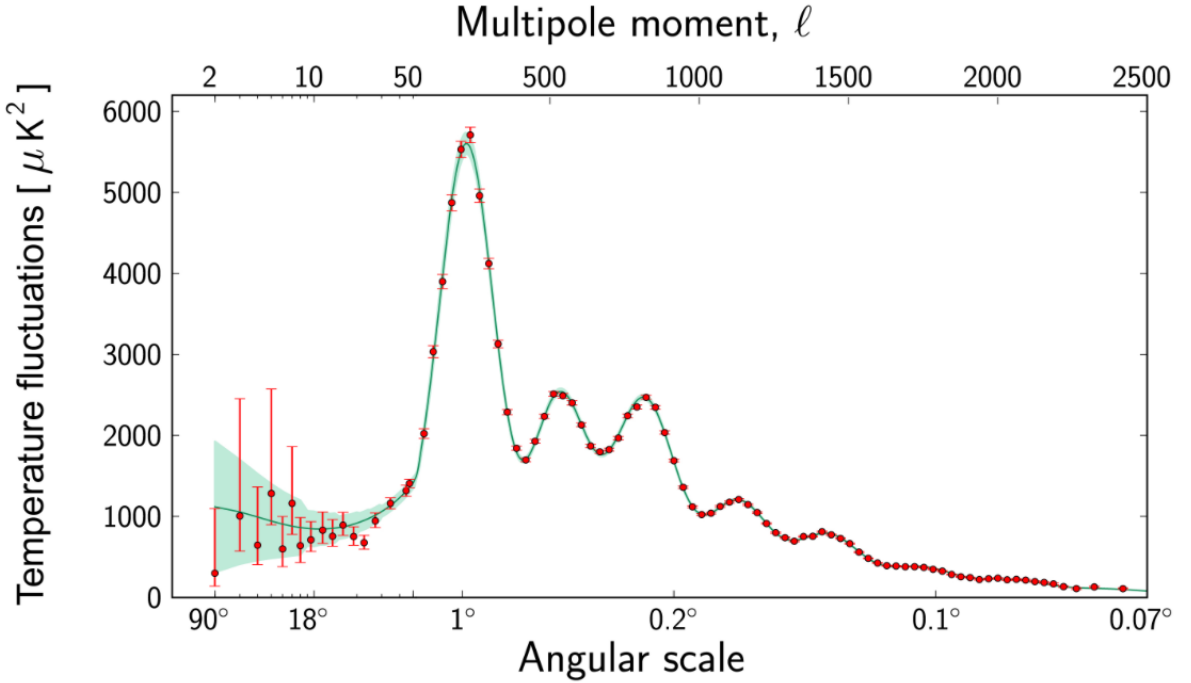


Figure 3.5. Power spectrum. Planck’s power spectrum of temperature fluctuations in the cosmic microwave background. The anisotropy in fluctuations are shown at different angular scales on the sky. Here the red dots with error bars are the Planck data and the green curve shows the standard model of cosmology. The peak at 1 degree is consistent with a flat geometry of the universe, the height of the second peak with 5%, and the second and third peaks with 26% dark matter [42].

decays and its implications for particle physics by focusing on the positron excess observed by the Alpha Magnetic Spectrometer (AMS) collaboration [47].

3.1.5 Positron Excess

Adding to the already growing list of astrophysical anomalies, the AMS [47] experiment on board the International Space Station (ISS), and PAMELA [25], measured the electron flux and the positron flux in primary cosmic rays, and have found an abundance “excess” of positrons. Positrons are known to be produced in secondary production processes resulting from the interaction between cosmic-ray nuclei and interstellar gas. Bjorken *et al.* interpreted this signal as possibly due to dark matter

annihilation in the galactic halo or in the magnetospheres of near-by pulsars [9]. The source of this excess e^+/e^- can be explained by dark matter charged under new $U(1)'$ annihilating in an A' as noted above in chapter 2.

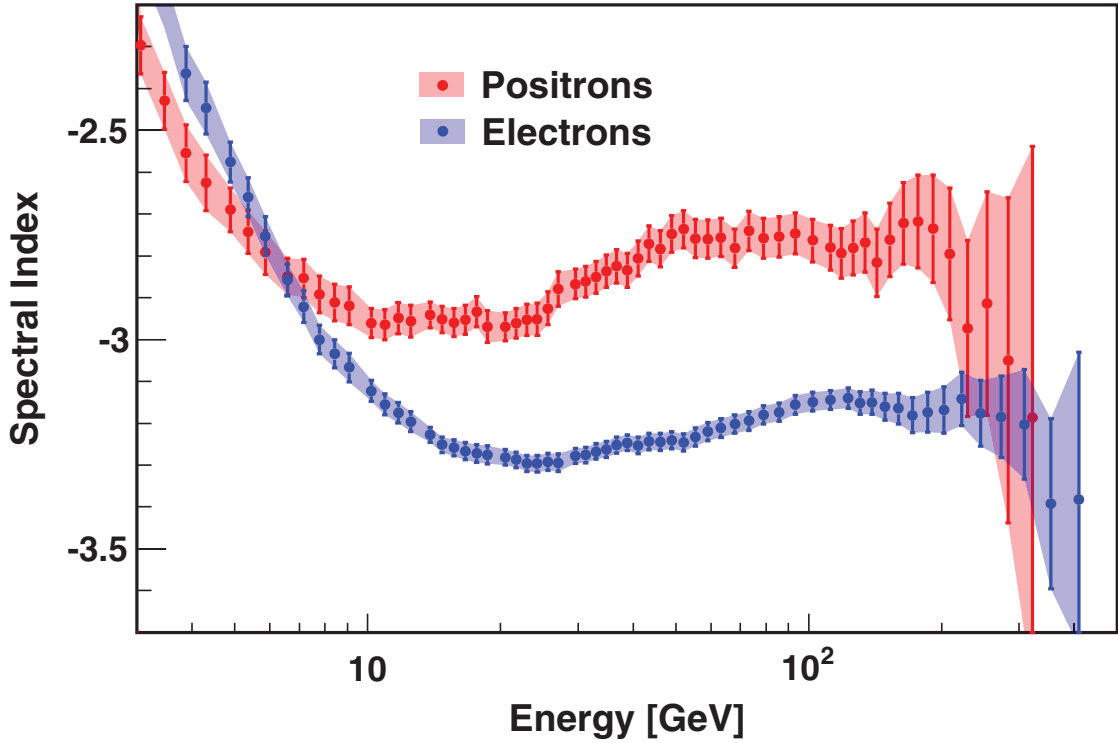


Figure 3.6. Positron and electron flux. Spectral indices of the electron flux γ_{e^-} and of the positron flux γ_{e^+} as a function of energy [47].

Figure 3.6 shows the positron and electron flux as a function of energy. The measurements are based on 41×10^9 events collected between May 19, 2011, and November 26, 2013, and cover the energy ranges 0.5 to 700 GeV for electrons and 0.5 to 500 GeV for positrons [47]. A ratio of positron and electron fluxes (Φ_{e^+}/Φ_{e^-}), the positron fraction, $\Phi(e^+)/(\Phi(e^+) + \Phi(e^-))$, can be used as a means of investigating possible primary sources [47]. If secondary production is the dominant source, the positron fraction is expected to fall as a smooth function of increasing energy, but was instead found to be steadily increasing from 10 to ~ 250 GeV [47]. These observations from AMS and PAMELA on the positron fraction generated widespread interest and

discussions on the origin of high-energy positrons, especially in the particle physics community where possible resolutions to this conundrum could also explain known particle physics anomalies which will be discussed in following section.

3.2 Particle Physics Anomalies

The possibility of explaining anomalies in astrophysics and particle physics via the extension of the SM by an additional $U(1)$ gauge group manifesting itself in a massive gauge boson A' (“dark photon”) in the MeV to GeV mass range motivated strong activity in both theoretical and experimental physics. Figure 3.7 shows the various activities in the explorations of these anomalies [37].

Dark Sector Candidates, Anomalies, and Search Techniques

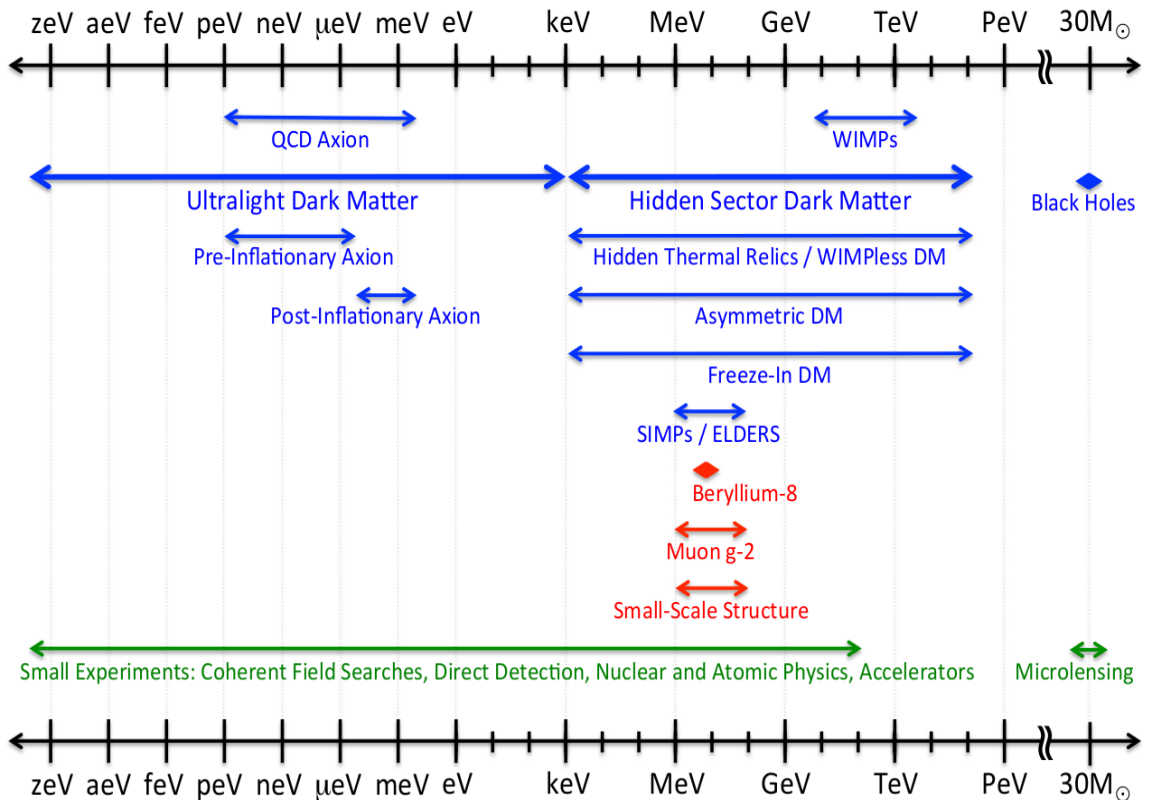


Figure 3.7. Energy regimes and possible mass ranges. Mass ranges for dark matter and mediator particle candidates and experimental anomalies.

A plethora of work, where new physics scenarios were explored as a possible explanation of the proton charge radius problem, as well as a resolution to the anomalous magnetic moment of the muon; in this thesis the constraints from rare kaon decays were examined. The work by Beranek and Vanderhaeghen [48] used these rare kaon decays to find constraints on the A' parameters, whereas the work by Carlson and Rislow [12] used rare kaon decays to explore solutions for both the proton radius puzzle as well as the anomalous magnetic moment of the muon $(g - 2)_\mu$. The A' couples to the electromagnetic current via kinetic mixing giving rise to a QED-like vertex term. The following sub-sections cover muon anomalies, namely the proton radius puzzle and the muon anomalous magnetic moment, and their possible solutions in light of A' .

3.2.1 The Muon Magnetic Moment

There is a longstanding discrepancy in the measured and calculated values for the anomalous magnetic moment of the muon, which points to beyond SM physics. Experimentally, the $(g - 2)_\mu$ value is precisely measured and the theory calculation for the anomalous moment is likewise accurate, with the bulk of the error coming from contributions in hadronic uncertainties [12]. There is a longstanding, non-negligible, enduring discrepancy between experiment and the SM value. The SM value for a_μ^{SM} was calculated in [49]

$$\begin{aligned} a_\mu^{exp} &= (116\ 592\ 089 \pm 63) \times 10^{-11} \text{ [0.5 ppm]}, \\ a_\mu^{SM} &= (116\ 591\ 810 \pm 43) \times 10^{-11} \text{ [0.5 ppm]}, \\ \Delta a_\mu &= (279 \pm 76) \times 10^{-11} \text{ [2.1 ppm} \pm 0.7 \text{ ppm]}. \end{aligned} \tag{3.2.1}$$

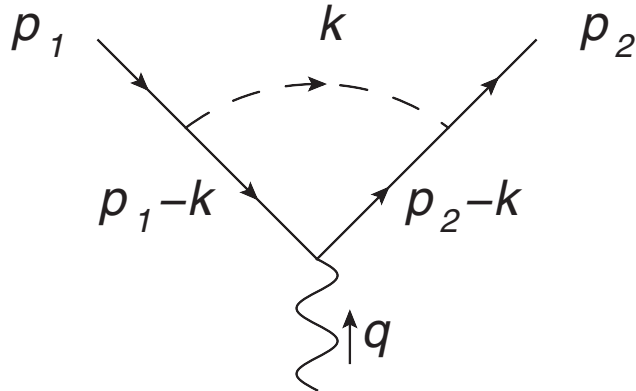


Figure 3.8. One-loop magnetic moment correction.

The SM value calculated by Aoyama *et al.* is base on Refs. [50–69], and corresponds to a 3.7σ discrepancy with experimental measurement [70]. This discrepancy is four orders of magnitude, in fractional terms, smaller than the one due to the Lamb shift. Every particle that contributes to the Lamb shift also contributes to the magnetic moment at the one-loop level [12] as is show in figure 3.8.

A possible explanation for the the $(g - 2)_\mu$ discrepancy could be kinetically mixed dark photons, decaying predominantly into dark-sector states such as $A' \rightarrow \chi_2 \chi_1$, $\chi_2 \rightarrow \chi_1 + \text{SM}$ (for and invisible χ_1) [37]. Carlson and Rislow [12] on the other hand consider contributions of the pseudoscalar and axial vector, whose couplings are not constrained by the Lamb shift, have opposite sign to those from the scalar and polar vector, and can be tuned to respect this much smaller discrepancy. They also considered the scalar and pseudoscalar particles to have the same masses.

3.2.2 The ${}^8\text{Be}$ Decay: Protophobic Photon

Presently, there are four known forces of nature namely, the strong, electromagnetic, weak and gravity; which are mediated by the gluon, photon, W^\pm and Z , and graviton, respectively. Curiously and/or possibly a fifth force which is mediated by

an as-yet-unknown gauge boson has been of interest to the community since the introduction of Yang-Mills gauge theories [71]. In the event that such a force exists, it must either be weak or short-ranged, or perhaps both in order to be consistent with the cornucopia of experimental data. Recently, an anomaly in the nuclear decay of ${}^8\text{Be}$ has been observed to 6.8σ in the opening angle and invariant mass distribution of e^+e^- pairs [72].

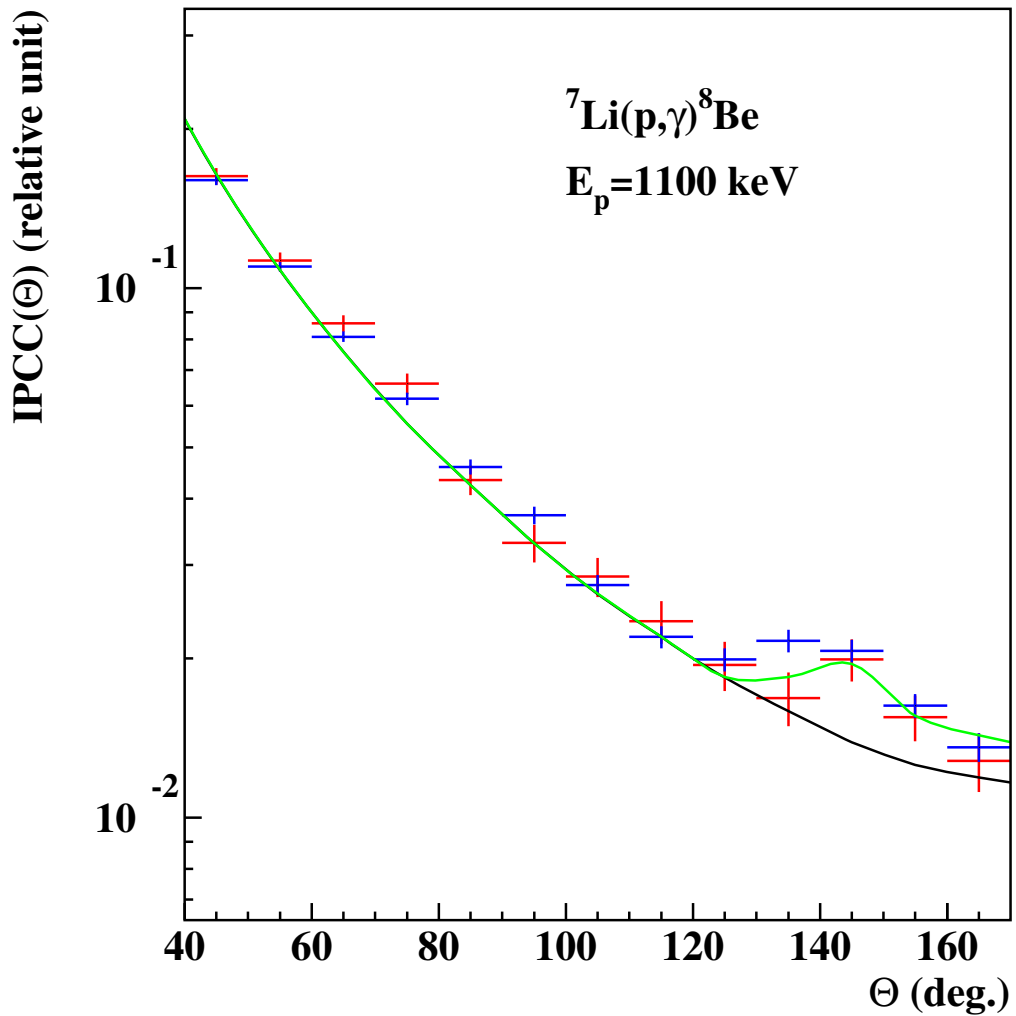


Figure 3.9. ${}^8\text{Be}$ angular measurement decays. Measured angular correlations (red) alongside previous measurements (blue) of the e^+e^- pairs originated from the decay of the 18.15 MeV ground state transition in ${}^8\text{Be}$. The black line represents the background, while the green one is the sum of the signal and background [72].

In the experiment, excited states of ${}^8\text{Be}$ were selectively populated by ${}^7\text{Li}(\text{p},\gamma)$ ${}^8\text{Be}$ and the differential internal pair conversion coefficients were studied for the 17.6 MeV, and 18.15 MeV ($J^\pi = 1^+ \rightarrow 0^+$) M1 transitions in ${}^8\text{Be}$ [72]. A significant peak-like enhancement of the internal pair creation was seen at large angles in the angular correlation of the 18.15 MeV transition, but not in the 17.6 MeV one, in figure 3.9 [72]. Given this staggering observation, Krasznahorkay *et al.* [72] fit a new boson X with mass $m_X = 16.70 \pm 0.35 \text{ (stat)} \pm 0.5 \text{ (sys)} \text{ MeV}$. Feng *et al.* [73] proposed a new vector protophobic X gauge boson which mediates the fifth force with a characteristic scale of 12 fm. In fulfilling the requirements of the signal as well as constraints from the wealth of experimental data that probe these low energy scales, that constrain the mass of the X boson to small ranges, its mass was found to be $m_X \approx 17 \text{ MeV}$ [73].

Astonishingly, Krasznahorkay *et al.* [74] have reported new observations in a ${}^4\text{He}$ transition whose kinematics are consistent with the same 17 MeV mass observed in ${}^8\text{Be}$ results.

These results presented in figure 3.10 led Feng *et al.* [75] to scrutinize the possibility of simultaneously explaining both ${}^4\text{He}$ and ${}^8\text{Be}$ results with a the new particle X that has either scalar, pseudoscalar, vector, or axial vector boson coupling to nucleons and electrons. They found that if the X boson is a vector then the protophobic rates required by the ${}^8\text{Be}$ results predicts rates for ${}^4\text{He}$ transitions.

3.2.3 The Proton Radius Puzzle

Being the dominant component of the visible universe, it is imperative to understand both the basic properties of the proton, such as the charge radius r_p and its anomalous magnetic moment, neither of which is as yet well established. The proton charge radius problem, which resulted in furious activities in the fields of theoretical and experimental physics, has its origins in the Lamb shift measurements of

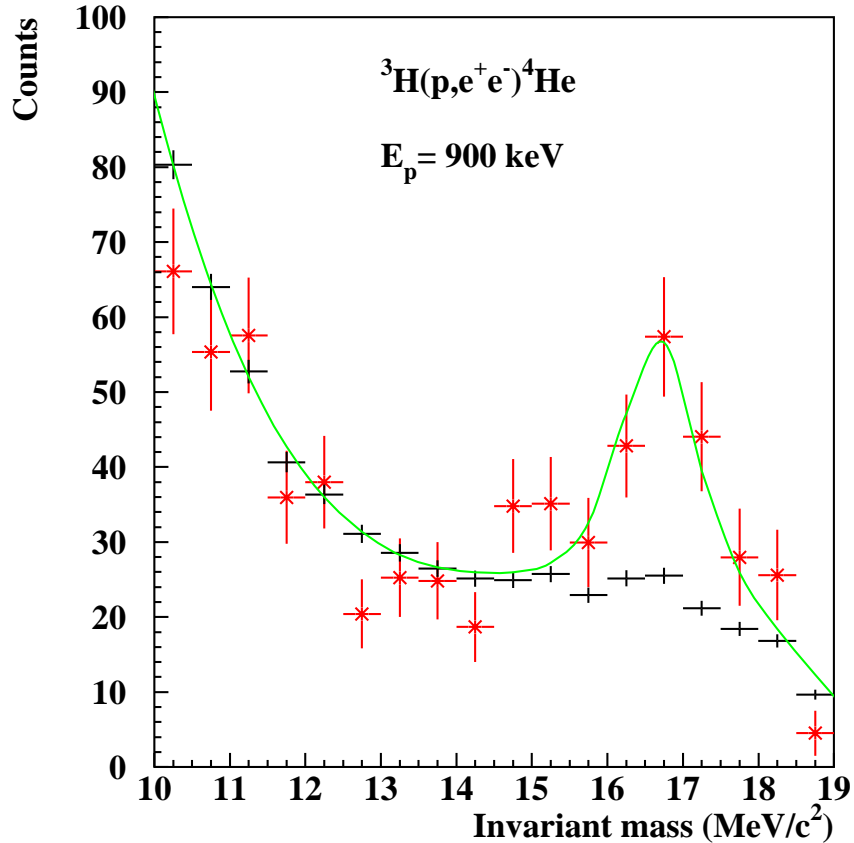


Figure 3.10. Invariant mass distribution for ${}^4\text{He}$ transition [74].

muonic hydrogen (μH). The measurement of the μH Lamb shift yielded a proton charge radius that was 5σ smaller than the 2006 Committee on Data for Science and Technology (CODATA) value available at the time of its publication and this value was later found to be an alarming 7σ smaller than the 2010 CODATA update, which at the time had incorporated the latest proton radius determinations from electron scattering [76]. This surprising result was dubbed the *the proton radius puzzle*. Since then experiments exploring the nature of this discrepancy have been conducted and figure 3.11 shows the current status of r_p measurements including the newest results from the PRad collaboration [77].

Although the PRad result points to small value for r_p , which is 2.7σ smaller than the CODATA recommended value for e–p experiments, it should be noted that by

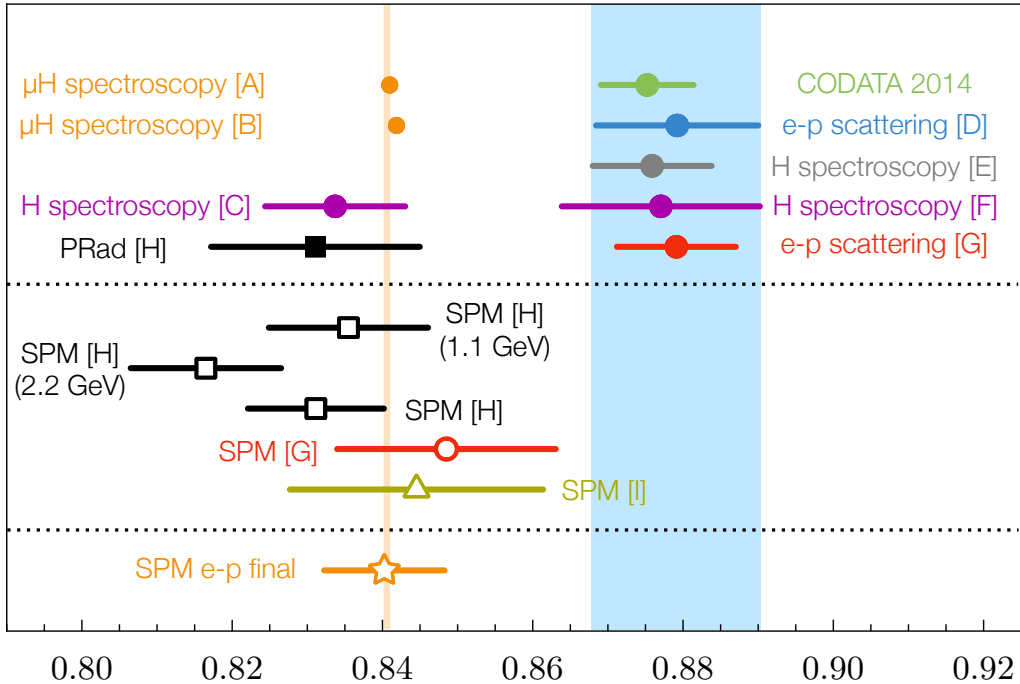


Figure 3.11. The proton charge radius r_p . The top panel. The recent PRad value [77] [H], is shown alongside other measurements of r_p obtain using various techniques: CODATA = [78]; [A] = [79]; [B] = [76]; [C] = [80]; [D] = [78]; [E] = [78]; [F] = [81]; [G] = [82]; [H] = [77]. The middle panel. Results were obtained from data in the following references: [77, 82] and [I] = [83] used the the Schlessinger Point Method (SPM) as described in [84–86]. The bottom panel. “SPM ep final” is the combined result from SPM extractions.

2010 e–p results agreed with each other. It is still possible that perhaps this surprising μ H result is due to new physics beyond the Standard Model resulting in μ –e non-universality. Plenty of new physics proposals have been considered to explain the discrepancy. Batell et al. [38] propose that a hidden photon could be responsible for the Lamb shift discrepancy by requiring it to couple only to right-handed muons. This boson also mixes with the photon so that the couplings contained additional model dependence. In order to account for the muon anomalous magnetic moment (next section) constraint, they were forced to introduce and fine-tune the mass of a new scalar particle. Carlson and Rislow explored the possibility that fine-tuned particle couplings, free from the phenomenological demands of hidden photons, can satisfy

both the anomalous magnetic moment of the muon and K-decay as well as other constraints [12]. They considered two separate possibilities. In the first scenario, they considered two new particles that interact with muons and protons through fine-tuned scalar and pseudoscalar couplings, respectively. In the second case, they considered two new particles that interact with muons and protons through fine-tuned polar and axial vector couplings, respectively. The TREK/E36 has sensitivity to both possibilities, making it the ideal place to test the validity of these particles and their respective couplings.

3.3 New Physics Models

The aforementioned overwhelming evidence of dark matter from the CMB as well as the observed gamma ray burst and positron excess from astrophysics along with particle physics anomalies such as the $(g - 2)_\mu$, brought about the idea of an $U(1)'$ extension of the Standard Model. This $U(1)'$ gauge group would manifest itself as a massive gauge boson A' in the MeV-GeV mass range, commonly referred to as a dark photon, has invited much theoretical activity in attempts to explicate the proton radius puzzle, $(g - 2)_\mu$ and the anomalous ${}^8\text{Be}$ decay. The A' shares many of the properties of the QED photon, and couples to the electromagnetic current via kinetic mixing giving rise to a QED-like vertex term $i\varepsilon e\gamma$, where ε is the kinetic mixing parameter describing the coupling strength of the electromagnetic current by

$$\varepsilon^2 = \alpha'/\alpha_{QED} \text{ with } \alpha_{QED} \equiv e^2/4\pi [35].$$

The scenarios in which the A' decays directly into SM particles can be tested in electron and proton fixed target experiments such as APEX [87] which recently took production data. An exhaustive list of A' searches at the Thomas Jefferson National Accelerator Facility can be found in Ref. [88]. Hadron collider searches for A' decays

are covered in [35, 89, 90], a comprehensive summary for dark photon searches at the LHC are well summarized in [91].

Mention should be made that the A' need not necessarily be dark matter itself, rather it could mediate interactions between visible and hidden and/or possibly dark sectors, thereby giving rise to a slew of addition particles that interact weakly with the SM hypercharge. For example, in order to explain the ${}^8\text{Be}$ anomaly Feng *et al.*, introduced a 17 MeV spin-1 protophobic boson X mediating the weak force with a range of 12 fm [73, 92]; having found that dark photons were disfavored experimental constraints primarily the null results from $\pi^0 \rightarrow A'\gamma$ [92]. This new boson X would constitute a new fundamental force of nature, fifth force, directly elucidating the need for New Physics.

New Physics explanations of the muonic hydrogen Lamb shift involving new particles must include larger couplings to muon, directly violating lepton universality. Jaeckel and Roy [93], as part of a broader examination into deviations of Coulomb's law, have showed that the ubiquitous $U(1)'$ dark photon model was in conflict with Lamb shift measurements from ordinary hydrogen and could therefore not be explanation of the proton radius puzzle. Furthermore, these NP explanations must also obey constraints placed by the discrepancy in the measured and calculated value of the anomalous magnetic moment of the muon. Several lepton universality violating models involving preferential scalar or vector couplings to muons and protons have been proposed [10–14, 16, 94]. Barger *et al.* [95] have demonstrated the constraints placed on explanations involving scalar, vector and tensor couplings by meson decays.

Batell *et al.* [11] have resurrected the $U(1)'$ dark photon model by inserting an additional coupling to right-handed muons. Although the additional coupling to right-handed muons was sufficient to explain the proton radius puzzle, a simultaneous explanation of both r_p and the $(g - 2)_\mu$ discrepancy would require a tight correlation between scalar and vector masses.

The Carlson model [13] introduces two new particles with polar and axial vector couplings to protons and muons respectively, in order to explain the proton radius puzzle while also obeying the $(g - 2)_\mu$ discrepancy. The coupling strength of polar vector was chosen to explain the proton radius puzzle. The axial vector coupling enters the expression for the anomalous magnetic moment with an opposite sign to the polar vector, and was fine tuned to explain the $(g-2)_\mu$ discrepancy [12]. Rare kaon decays provide a good laboratory to test NP explanations for the proton radius puzzle. Beranek and Vanderhaeghen [48] have calculated constraints that the dark photon via kinetic mixing as well as lepton universality violating couplings are expected to contribute to the $K^+ \rightarrow \mu^+ \nu e^+ e^-$ decay. Carlson and Rislow [12, 13] calculated their light neutral boson's contribution to the $K^+ \rightarrow \mu^+ \nu e^+ e^-$ amplitude by modifying the photon's propagator and charged fermion couplings as follows [13]

$$\frac{-i}{q^2} \rightarrow \frac{-i}{q^2 - m_{A'}^2 + im_{A'}\Gamma}, \quad (3.3.1)$$

$$-ie\gamma^\nu \rightarrow \gamma^\nu \varepsilon(C_V(m_{A'}) + C_A(m_{A'})\gamma^5), \quad (3.3.2)$$

where $C_V(m_{A'})$ and $C_A(m_{A'})$ are the polar and axial vector couplings to muons calculated in [12]. The couplings $C_{V,A}$ were chosen so as to obtain an extra $310 \mu\text{eV}$ muonic hydrogen Lamb shift from an electrophobic spin-0 or spin-1 particle as described in [12]. Figure 3.12 shows the muonic kaon decay involving an $A' K^+ \rightarrow \mu^+ \nu A'$ followed promptly by $A' \rightarrow e^+ e^-$.

Carlson and Rislow have allowed for the possibility that the new particle has scalar and pseudoscalar couplings to muons and protons. They have modeled its contribution to the $K^+ \rightarrow \mu^+ \nu e^+ e^-$ amplitude by modifying the photons propagator as before and modifying the charged fermion couplings as [12]

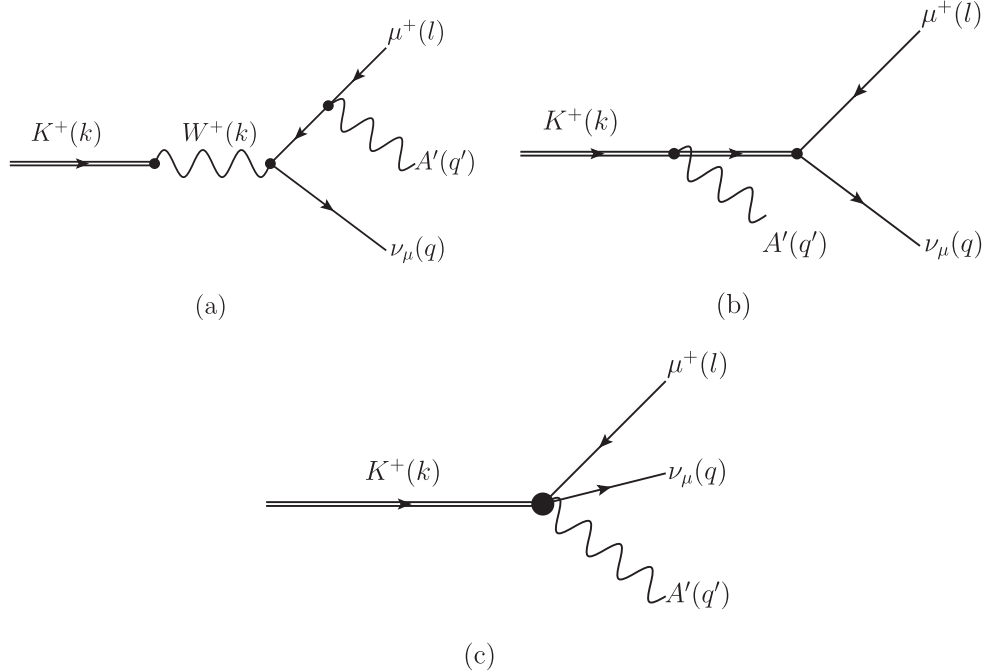


Figure 3.12. A' production amplitude. Feynman diagram showing the channel of interest $K^+ \rightarrow \mu^+ \nu_\mu A'$ [48].

$$-ie\gamma^\mu \rightarrow -i\varepsilon(C_S(m_{A'})) + iC_P(m_{A'}\gamma^5), \quad (3.3.3)$$

where $C_S(m_{A'})$ and $C_P(m_{A'})$ are the scalar and pseudoscalar couplings to muons as calculated in [12]. They have also calculated mass limits on polar and axial vector (as well as scalar and pseudoscalar) particles due to constraints placed by searches of muonic kaon decays $K^+ \rightarrow \mu X$. Their results are presented in figure 3.13. The solid curve in both figure 3.13 (a) and (b) is the result for a single particle with both polar (scalar) and axial vector (pseudoscalar) couplings. The horizontal line indicates the experimental limit, and ϕ can be taken to represent the A' .

Carlson and Rislow have calculated the branching ratio $\mathcal{B}r(K^+ \rightarrow \mu^+ \nu A')$ to be $\mathcal{O}(-5)$ for polar and axial vector couplings. Their prediction indicate that a strong

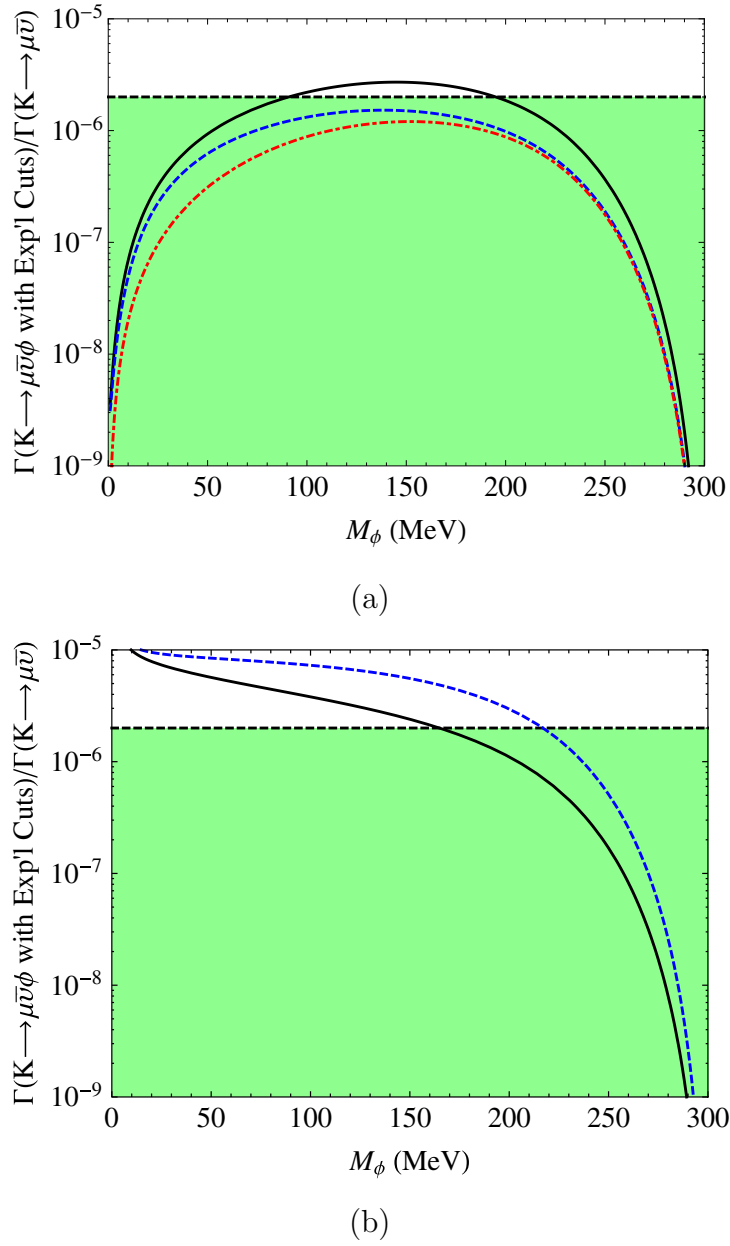


Figure 3.13. Mass limits on particles with scalar and pseudoscalar (a), and polar and axial vector (b) couplings due to constraints placed by $K^+ \rightarrow \mu X$ searches. The solid curve is the result for a single particle with both polar (scalar) and axial vector (pseudoscalar) couplings. In (a) the contributions of scalar coupling is represented by the dashed curve and the dash-dotted curve represents the pseudoscalar coupling. In (b) the dashed curve is the result for separate polar and axial vector particles with equal masses, and in both (a) and (b) the green region represents the experimental limit (horizontal line) [12].

signal peak over the SM background would be observed experimentally as shown in figure 3.14.

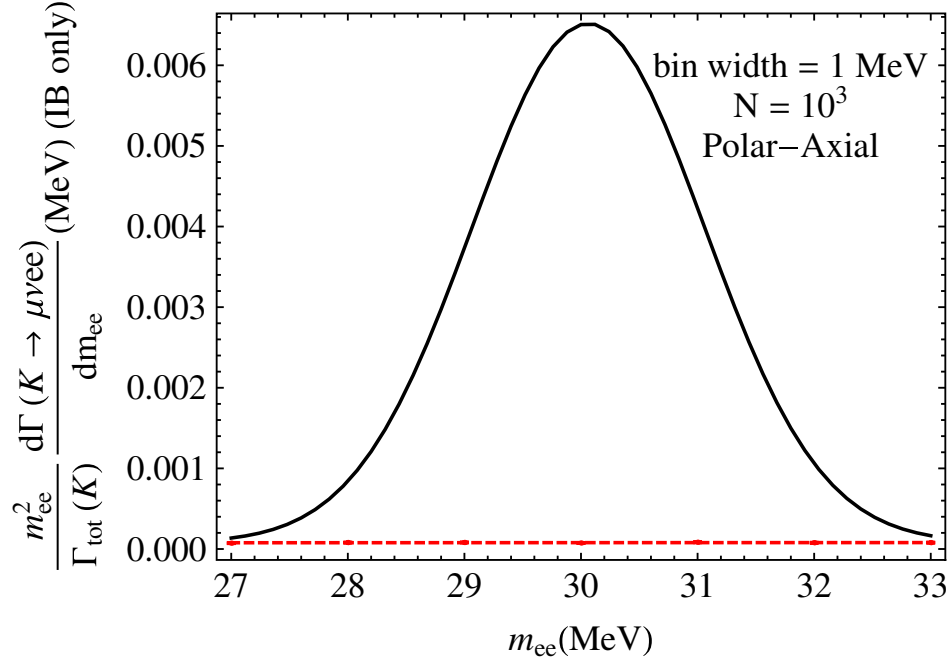


Figure 3.14. Strong signal to background prediction. The QED background prediction for $K^+ \rightarrow \mu^+ \nu e^+ e^-$ (red dashed curve) and the prediction with a 30 MeV lepton universality violating A' of the Carlson model [16].

Given the strong signal to background expectation of the Carlson model, the TREK/E36 experiment which is sensitive to light neutral bosons below 300 MeV would be able to test the efficacy of the Carlson model. The search would include a charged μ^+ that is detected in the spectrometer gap and two clusters in the CsI barrel from $e^+ - e^-$ pairs, from which a peak search will be conducted in the invariant mass spectrum M_{ee} .

CHAPTER 4

EXPERIMENT SETUP AND COMMISSIONING

4.1 Overview

The TREK/E36 experiment was conducted at the Japan Proton Accelerator Research Complex (J-PARC) and made use of stopped K^+ mesons in-conjunction with a 12 sector iron core superconducting toroidal spectrometer to study lepton universality. Two-body leptonic kaon decays $K^+ \rightarrow e^+\nu$ (K_{e2}) and $K^+ \rightarrow \mu^+\nu$ ($K_{\mu 2}$) events were accepted by analyzing the momenta of charged particles using the superconducting spectrometer. The ratio R_K will be derived from the numbers of the accepted K_{e2} and $K_{\mu 2}$ events after correcting for the detector acceptance. The schematic longitudinal and end views of the detector system are shown in figure 4.1.

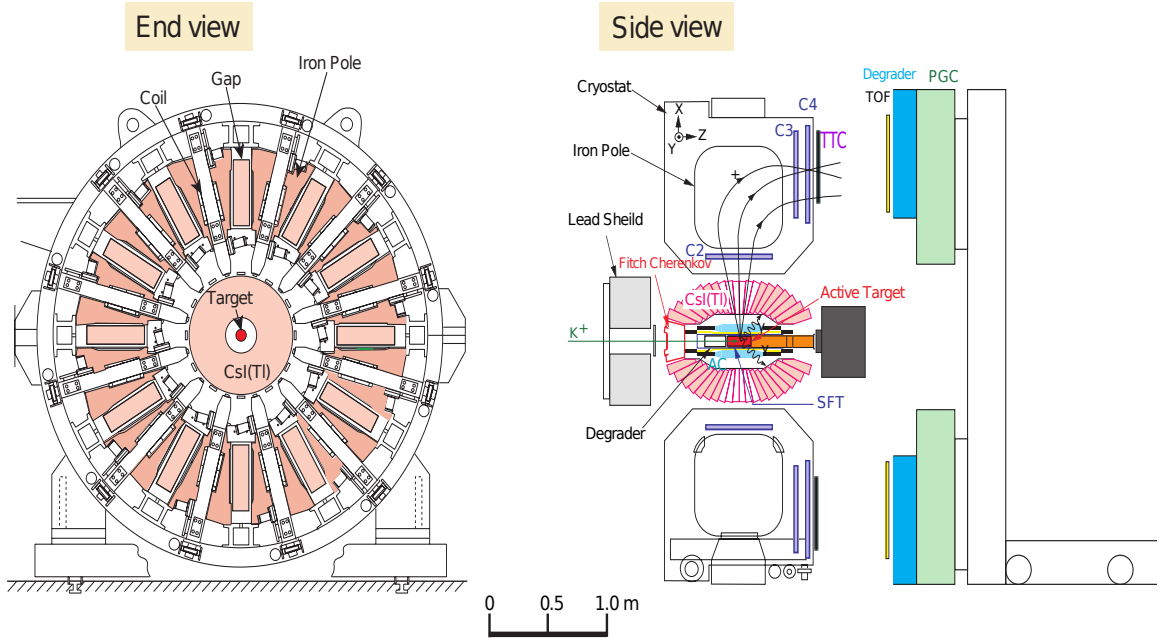


Figure 4.1. TREK/E36 apparatus. General cross-sectional and longitudinal views of the detector system.

A separated 780 MeV/ c ($\pm 2\%$) K^+ beam was extracted using the J-PARC K1.1BR beam line. The beam was slowed down by a degrader and stopped in an active scintillating fiber target, which provides the x and y coordinates of the vertex [96]. K^+ charged particle decays exiting the target were tracked and momentum analyzed using spiral fiber trackers (SFT) and three multi-wire proportional chambers (C2, C3, C4) in each of the toroidal sectors [97]. The SFT bundle was placed around the target and provides the z -coordinate of the stopping vertex [18]. In conjunction with the target, this provides 3 dimensional information of the K^+ decay vertex. The C2 and C3-C4 chambers were placed at the entrance and exit of the magnet gaps respectively [1]. Discrimination between e^+ and μ^+ was determined by a concert of PID detectors, the aerogel Čherenkov (AC) counters and lead-glass counters (PGC), and by measuring the time-of-flight (TOF) between the TOF1 and TOF2 counters [1]. The TOF1 counters surrounded the SFTs and the TOF2 counters were located behind the C4 chambers and the thin trigger counters (TTC). Photons were detected with an assembly of 768 CsI(Tl) crystals, covering 75% of the total solid angle [96]. Due to the electromagnetic showers produced by photons, their energy is shared among several crystals [1]. Photon energy and hit position were therefore obtained by summing the energy deposits and by determination of the energy-weighted centroid, respectively [97]. Gap veto (GV) counters consisting of Pb-plastic sandwich were set at the outer radius of the magnet pole to monitor photons passing through the CsI(Tl) holes [1].

The author played an instrumental in the detector installation and commissioning phases of TREK/E36, by assembling detector supports and participating in installing various detectors. The author was also heavily involved with detector maintenance, having repaired two C3 chamber with tripped signal wires and worked with Dr. Jun Imazato to repair light leakage in the TOF2 counters. The author set-up a high voltage slow control (figure4.2) and participated in the shift-taking during both the engineering and production run periods.

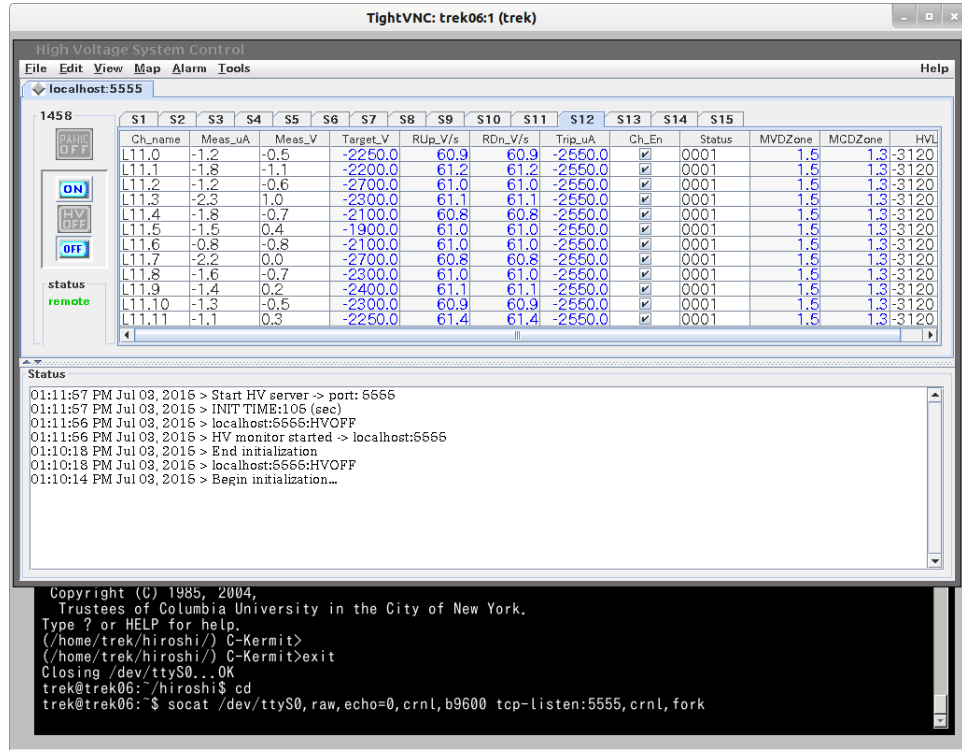


Figure 4.2. Screenshot of the high voltage slow control graphical user interface.

4.2 Beamline

In order to perform the stopped K^+ method used in the TREK/E36 experiment, a low momentum K^+ beam of $780 \text{ MeV}/c \pm 2\%$ was extracted from the K1.1BR [17]. The layout of the beamline is shown in the figure 4.3. A single electro-static separator (ESS) was used along with a vertical focus (IFY). Having the IFY before the ESS served an important role in increasing the K/π ratio [1]. In order to suppress the pion background, a horizontal focus was used after the sector type D3 magnet [1]. A circular beam was obtained at the final focus (FF) with a full width at half maximum of approximately 2.5 cm horizontally and vertically [1].

The important aspects of the $780 \text{ MeV}/c$ beam are [17]:

- Vertical focus at MS, which has a vertical and mass slit, removed most of the deflected pions

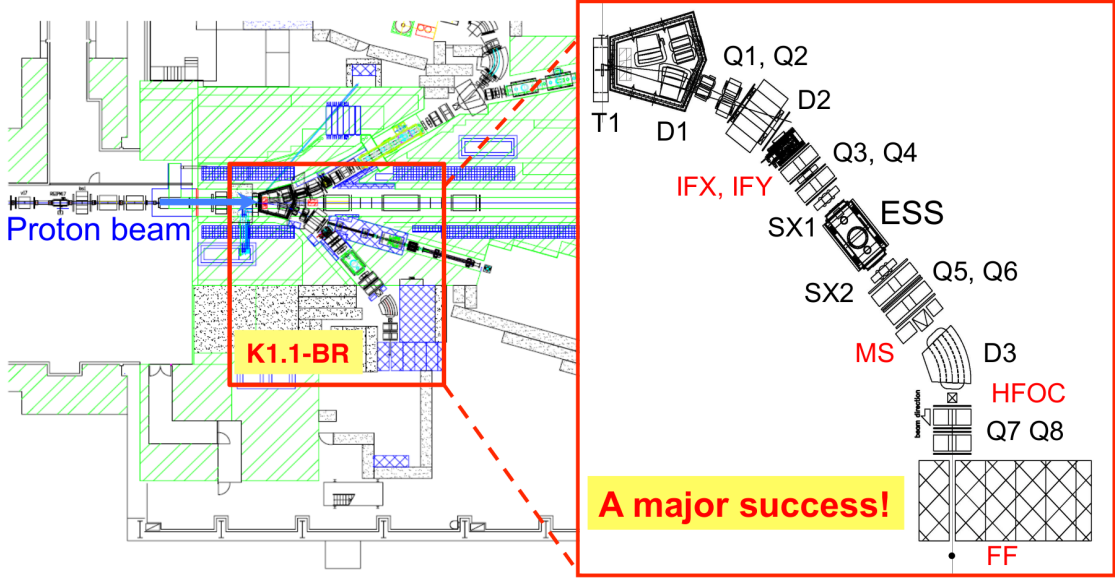


Figure 4.3. Layout of the K1.1BR beamline. There was only a single electro-static separator (ESS), the existence of a vertical focus (IFY) before the ESS played an important role in increasing the K/π ratio [1].

- Dispersion free horizontal focus at HFOC played an important role in removing any remaining pions
- Final Focus (FF) was 1.5 m downstream of the last quadrupole
- The length of the beamline was 19.0 m
- Momentum acceptance of $4.6\% \Delta p/p$ FWHM and $7\% \Delta p/p$ FWQM (Q=quarter)
- Total angle momentum acceptance of about 6.0 to 6.5 msr% $\Delta p/p$, which compared to 48 msr% $\Delta p/p$ for the LESB3 beam at Brookhaven
- Final full spot size was smaller than $2.5 \times 2.5 \text{ cm}^2$

4.3 Beam Collimation

An important cause of the pion (π) contamination in a single stage separated beam was found to be due to the presence of a π halo near the production target, as a result of neutral K meson decays, which presented a large vertical and horizontal source to the K^+ beam [1]. Therefore a collimator system was inserted between the last quadrupole of the K1.1BR channel and the beam Čerenkov counter. This consisted

of a 45 cm thick lead wall with a rectangular hole as well as an additional insert made of Hevimet for shaping the beam profile [97]. The thickness was determined in order to trim away the 780 MeV/ c π halo [97]. The shape of the insert was designed to transmit the K^+ profile while also blocking the π^+ halo in the CsI(Tl) region [97]. As a result the collimator system cut the π^+ halo background by 70% while only sacrificing 15% of the K^+ yield [97]. The collimated beam was counted by a beam hodoscope, and entered the Fitch-type beam Čerenkov counter system. The passage of a K^+ generated a light cone which was counted by a ring of photomultiplier tubes (PMTs) giving a signal for a K^+ [96]. After passing through the Čerenkov counter the beam was slowed down by a degrader system [1] consisting of 65 mm of Al followed by 242 mm of BeO located close to the stopping target. The 60 mm diameter was enough to cover the beam profile. The use of light element materials was essential to achieve high stopping power with minimum multiple scattering; in addition, using BeO near the target helped to reduce the interaction of photons from the target in the degrader while the use of Al further upstream served to reduce the cost [96]. The combination of lengths was optimized for a stopping distribution centered in the 200 mm long fiducial region of the target. The beam was accompanied by a π halo which was the main source of accidental hits on the CsI(Tl) crystals.

4.4 Central Detector System

The central detector (CD) system was comprised of a scintillating fiber target (target), spiral fiber tracker (SFT), time of flight counters (TOF1), aerogel Čerenkov (AC) counters and the CsI(Tl) barrel. The CsI barrel is highly segmented with 768 crystals covering a large solid angle of approximately 75% of 4π , surrounding the stopping target and was optimized for photon energy in the range of 10 to 250 MeV/ c [97]. This high degree of segmentation allowed for good kinematic resolution for the π^0 's [97].

4.4.1 Central Detector: Target

The 200 mm long, and 58 mm diameter active target which consisted of 256 (3.053×3.053 mm 2) scintillating fibers (SciFiber) was constructed at the TRIUMF national laboratory in Vancouver, BC. Each SciFiber had a groove into which a 1 mm thin wavelength shifting (WLS) fiber was embedded [1]. This high degree of segmentation along with the target SciFiber grooves and embedded WLS fibers are shown in figure 4.4 below.

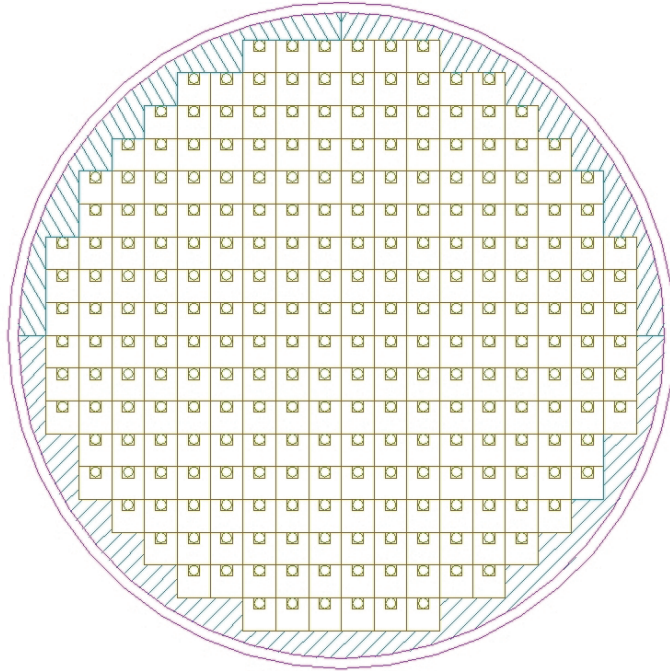


Figure 4.4. TREK/E36 target. Highly segmented 256 scintillating fiber target bundle along with embedded wavelength shifting fibers in the SciFiber grooves.

Highly segmented, the active target was used to identify the stopped K^+ decay vertex and provided the initial tracking information for the decay products of the K^+ . A K^+ track identified by the early time fibers with high energy deposits and the K^+ stopping position was determined by the intersection of the K^+ track and the outgoing lepton in most cases. Light from the WLS fibers was read out by multi-pixel proportional counters (MPPC) [97]. The segmentation level was a trade-off between

position resolution and rate handling from fine segmentation on the one hand, and energy and timing resolution from minimum ionizing decay muons and lower cost from coarse segmentation on the other hand [97]. Table 4.1 contains a summary of the target and WLS geometric parameters and material composition.

Table 4.1

Parameters for the target array and WLS fibers

Target parameters	
No. of SciFibers	256
Fiber dimensions	$3.053 \times 3.053 \times 200 \text{ mm}^3$
Diameter	58 mm
WLS parameters	
Diameter	1 mm
WLS type	BC408
PMT-WLS coupling	Optical glue

4.4.2 Central Detector: Spiral Fiber Tracker

The spiral fiber tracker (SFT) detector was designed and constructed by a Japanese company. It was assembled at KEK. The SFT detector was needed to determine the z coordinate of the stopped K^+ and needed to be accommodated within the central detector system. This was limited by the diameter of the CsI(Tl) aperture which was 225 mm [97]. As a result the SFT detector was limited to a thickness of no more than 5 mm [18]. Several criteria were taken into account in designing the SFT detector [18]:

- In order to ensure high detector efficiency as well as to extract the hit position information, several layers of ribbons were necessary
- The fibers were wound with two helicities of positive θ_L and negative θ_R which were required in order to obtain a crossing point ($\theta_{L/R}$ is the angle at the fibers are wound)

- Fiber lengths were minimized because of the light attenuation of the fibers
- The fiber ribbons were flexible to be wound around the bobbin (diameter of 79 mm)
- Maximized the number of channels

Plastic scintillating fiber Kuraray SCSF-78MJ of 1 mm diameter were used for the construction of the SFT fibers due to their high degree of geometric adaptability and because they are intrinsically fast [18, 98]. The four fiber ribbons had different lengths because each fiber ribbon had a different diameter. Furthermore different ribbon widths were adopted for left-helicity and right-helicity ribbons, such that $N_L = 17$ and $N_R = 15$ [18]. The active area of the 4th layer of the SFT had 14 turns of the 17-fiber ribbon, which meant that there were a total of 238 fibers in the fiducial region of 240 mm. The outer diameter of the SFT was 86 mm [18]. A schematic of the SFT is shown in figure 4.5 below, with only the 4th layer winding shown for simplicity [18].

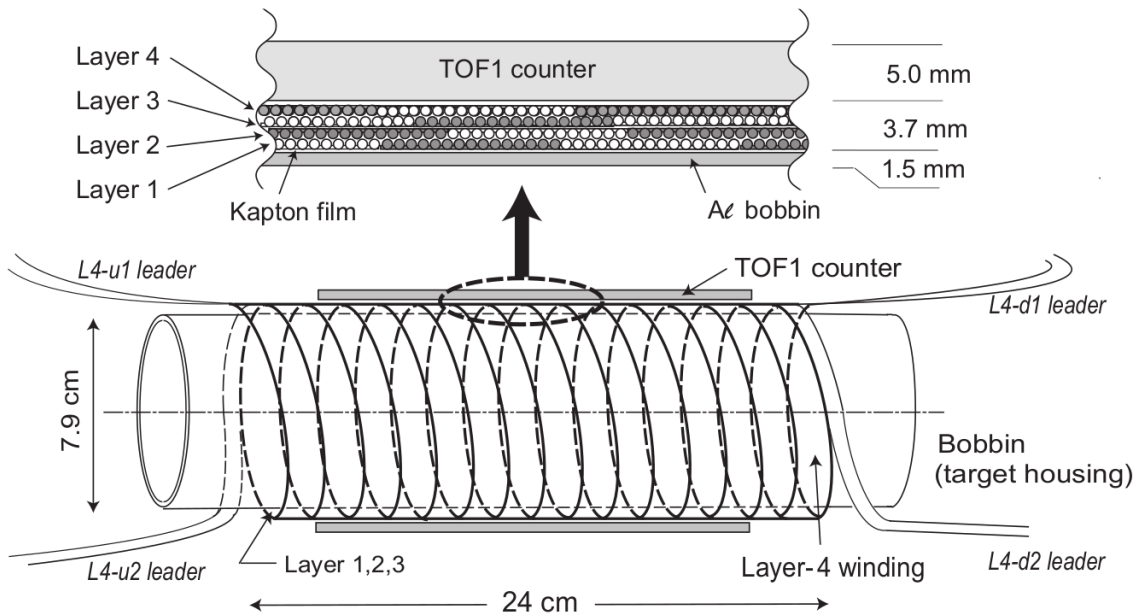


Figure 4.5. SFT schema with only the 4th layer winding shown for simplicity. The cross-sectional view shows the all 4 layers of coiled ribbons with wedging

Table 4.2 below shows the respective fiber length and ribbon size for a given layer [18].

Table 4.2

Main parameters for the SFT layers

SFT parameters	Layer 1	Layer 2	Layer 3	Layer 4
Helicity	right	right	left	left
SciFiber length	5215 mm	5307 mm	4623 mm	4702 mm
CF length	2, 203, 900	2, 203, 900	2, 203, 900	2, 203, 900
No. of fibers	15	15	17	17
Ribbon width	15.75 mm	15.75 mm	17.85 mm	17.85 mm
Layer diameter	80.5 mm	82.2 mm	84.2 mm	85.9 mm
No. of ribbon turns	17	17	14	14

4.4.3 Central Detector: TOF1 & TOF2

Time of flight measurements between TOF1 and TOF2 provided additional discrimination between e^+ and μ^+ , along with other particle identification (PID) systems. Each TOF1 counter had a thickness of 5 mm and was 188 mm long and 25 mm wide. The TOF2 counters were had a length of 800mm long, a width of 150 mm and thickness of 20 mm. Shorter TOF chambers were placed in gaps 5 and 7, due to their interference with floor rails, and had the same dimensions as the other counters except that they had a length of 680 mm. Twelve TOF1 counters were located around the outer layer of the SFT and twelve TOF2 counters were located at the exit of the spectrometer after C4 and the thin trigger counter (TTC) as shown in figure 4.1. Although time-walk, which is the uncertainty of light propagation time from the hit position of a particle to the PMT, was suppressed by reading signals from both ends of the TOF1 counters, non-negligible disagreements were found in time of flight and corrections are being applied. In the TREK/E36 experiment, an optimal separation of K_{e2} and $K_{\mu 2}$ requires a timing resolution of $\sigma_t = 100$ ps [1]. Table 4.3 shows a summary of the properties and main parameters of the time-of-flight detectors.

Table 4.3

Main parameters for the time-of-flight counters

Counter properties	TOF1	TOF2
Size	$188 \times 25 \text{ mm}^2$	$800 \times 150 \text{ mm}^2$
Thickness	5 mm	20 mm
Scintillator	BC404	BC404
PMT	H3171 – 03	H1161
Resolution	60 ps	80 ps

4.4.4 Central Detector: Aerogel Čerenkov

The aerogel Čerenkov (AC) detectors were manufactured at Chiba University, using silica aerogel, an amorphous and porous substance comprised of silica (SiO_2) particles and air-filled pores [99]. There was limited available space allotted to the height of the AC counters, with approximately 7 cm between the TOF1 counters and the CsI(Tl) barrel inner diameter [99]. A cross-sectional drawing of the central detector perpendicular to the kaon beam axis, where the aerogel radiator block has been shaded in blue is shown in figure 4.6. The AC counters were installed between the TOF1 counter and the inner wall of CsI(Tl) calorimeter.

Twelve identical AC counters were used in the experiment, in keeping with the 12 muon holes of the CsI(Tl) barrel and the 12 gaps of the toroidal spectrometer. In order to effectively reject in-flight muon decay events, the AC counters were placed close to the stopping target [99]. For this reason, the AC counters had a trapezoidal shape in order to fit around the target. The AC counters had a length of 178 mm, and a width of 46.2 mm for the upper-base and 24.8mm for the lower-base, and a thickness of 40 mm [99]. Figure 4.7 shows two AC radiators.

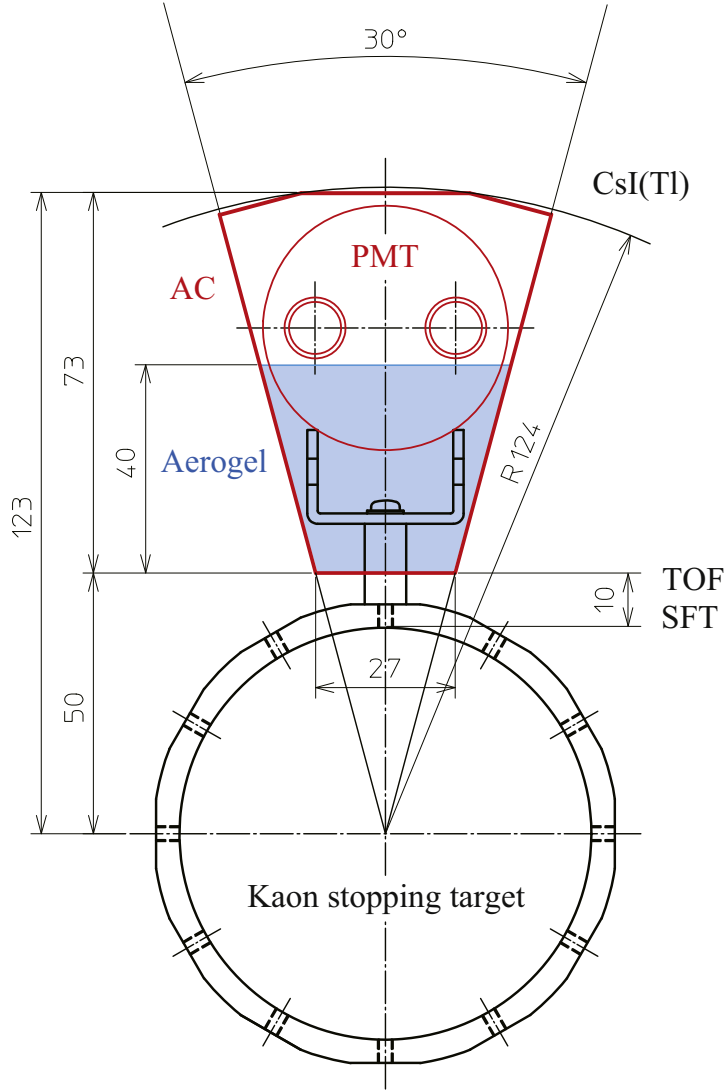


Figure 4.6. Cross-sectional drawing of the central detector perpendicular to the K^+ beam axis. The shaded region (blue) represents the aerogel radiator block. The AC counters were installed between the TOF1 counter and the inner wall of the CsI(Tl) calorimeter

Two PMTs were attached to both the upstream and downstream ends of the counters. The refractive index (n) of the aerogel radiator needed to be less than 1.095 in order to reject muons with a momentum (P) of 236 MeV/ c from the $K_{\mu 2}$ decays [99]. In general it was desirable to keep a high n value because aerogel radiators with higher n values produce more Čerenkov photons [99]. The design of the AC counters

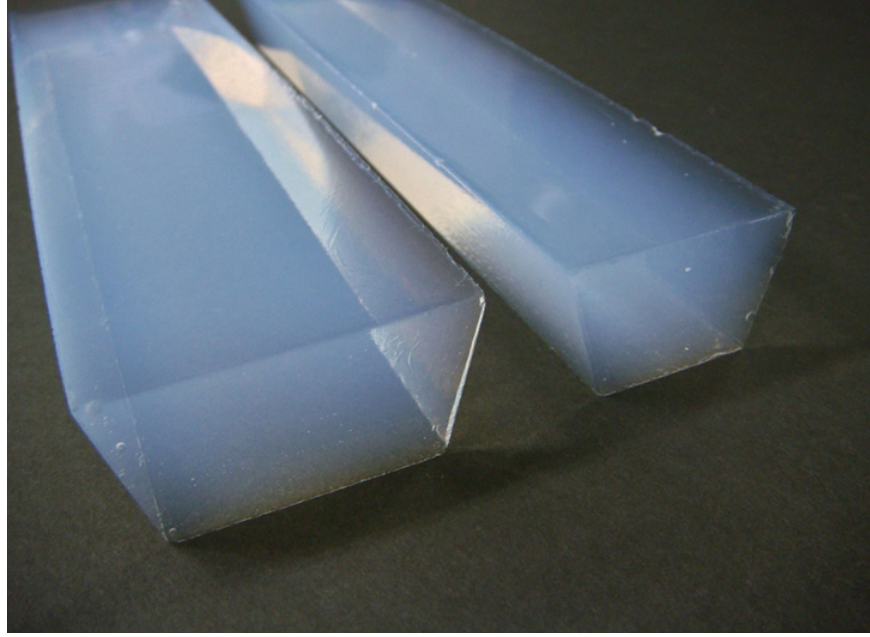


Figure 4.7. Two aerogel counters with length of 178 mm, produced for the TREK/E36 experiment.

utilized a reflective aluminized Mylar sheet and the radiator index of refraction was $n = 1.08$ [99].

4.4.5 Central Detector: CsI(Tl)

The photon detector was highly segmented and consisted of 768 CsI(Tl) crystals covering a large solid angle, surrounding the kaon stopping target, of approximately 75% of 4π [20]. Originally manufactured for the KEK-PS E246 experiment, the calorimeter detected gammas from $\pi^0 \rightarrow 2\gamma$ decays in the $K^+ \rightarrow \pi^0 \mu^+ \nu_\mu$ decay [100]. The calorimeter was optimized for photon energies in the range of 10–250 MeV/ c and the high degree of segmentation provided good kinematic resolution [97]. There were 12 symmetrically spaced holes through which charged particles escaped into the toroidal magnetic spectrometer gaps, which is shown in figure 4.8.

The CsI detector has the capability to detect photons which emerge from the target in the polar angle range of $15^\circ - 165^\circ$ and 2π in the azimuthal angle, with the

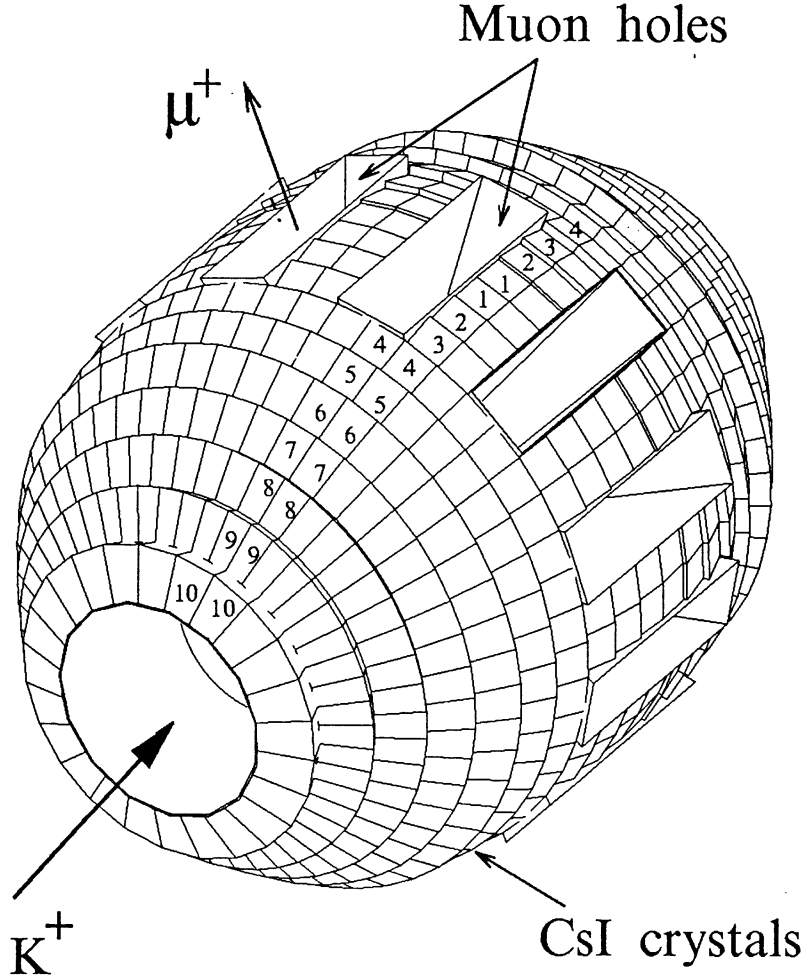


Figure 4.8. The highly segmented CsI(Tl) photon detector [20].

exception of the muon holes [20]. Each crystal covers about 7.5° along both the polar and azimuthal angles [96]. The length of a given crystal was 25 cm, which was long enough to neglect shower leakage from the rear end [20]. In order to reject background from pion cloud as well as other beam-associated accidentals, it was imperative to have good timing resolution. Table 4.4 contains a summary of the CsI geometry as well as single crystal module specifications.

PIN photodiodes (PIN diodes) were employed to readout scintillation light from CsI(Tl) crystals, because the calorimeter had to be operated under a strong fringing field from the toroidal magnet where PMTs would be difficult to use [100]. Each

Table 4.4

Specifications of the CsI(Tl) photon detector

Barrel	
Segmentation	$\Delta\theta = \Delta\phi = 7.5^\circ$
Total Crystal weight	1700 Kg
Inner diameter	40 cm
Outer diameter	100 cm
Detector length	141 cm
Solid angle coverage	75% of 4π
Modules	
Crystal length	25 cm
Surface treatment	Mirror polished (partial sanded)
Reflector	Two layers of 120 μm thick GSWP00010
Mean light yield (Type 1-9)	10920 p.e/MeV
Mean light yield (Type 10)	17400 p.e/MeV
Container	100 μm thick Al can
PIN diode	$18 \times 18 \text{ mm}^2$, 300 μm (type 1-9) $25 \times 25 \text{ mm}^2$, 500 μm (type 10)
Power consumption	0.25 W per pre-amplifier

crystal and its corresponding PIN diode and pre-amplifier were assembled in a 0.1 mm thick Al container. A charge sensitive pre-amplifier with a time constant of 600 μs and a gain of 0.5V/pC was attached directly to the PIN diode [19]. The output signal from the pre-amplifier was fed into a shaping amplifier with a 1 μs shaping time. Waveforms of the shaping amplifier outputs were recorded by VF48 flash ADCs produced at TRIUMF [19]. The VF48 has a time range of 10 μs and was operated with a 25 MHz external clock signal [19].

4.5 Spectrometer

The TREK/E36 experiment made use of a large acceptance spectrometer based on a superconducting toroidal magnet with iron cores, originally designed for hypernuclear spectroscopy and rare decay studies using stopped K mesons [101]. The spectrometer is capable of analyzing positively charged particles in the momentum range of 100 to 300 MeV/c with a large solid angle of 1.5 str [97]. The magnet assembly was comprised of 12 identical sectors and each sector was composed of an iron core and a coil cryostat [101]. The maximum design field in the gap was 1.8 T [96], however only approximately 1.45 T was used in the current experiment in order to obtain the optimum acceptance for K_{e2} electrons and $K_{\mu 2}$ muons. This 12 sector geometry is shown in the figure 4.9 below.

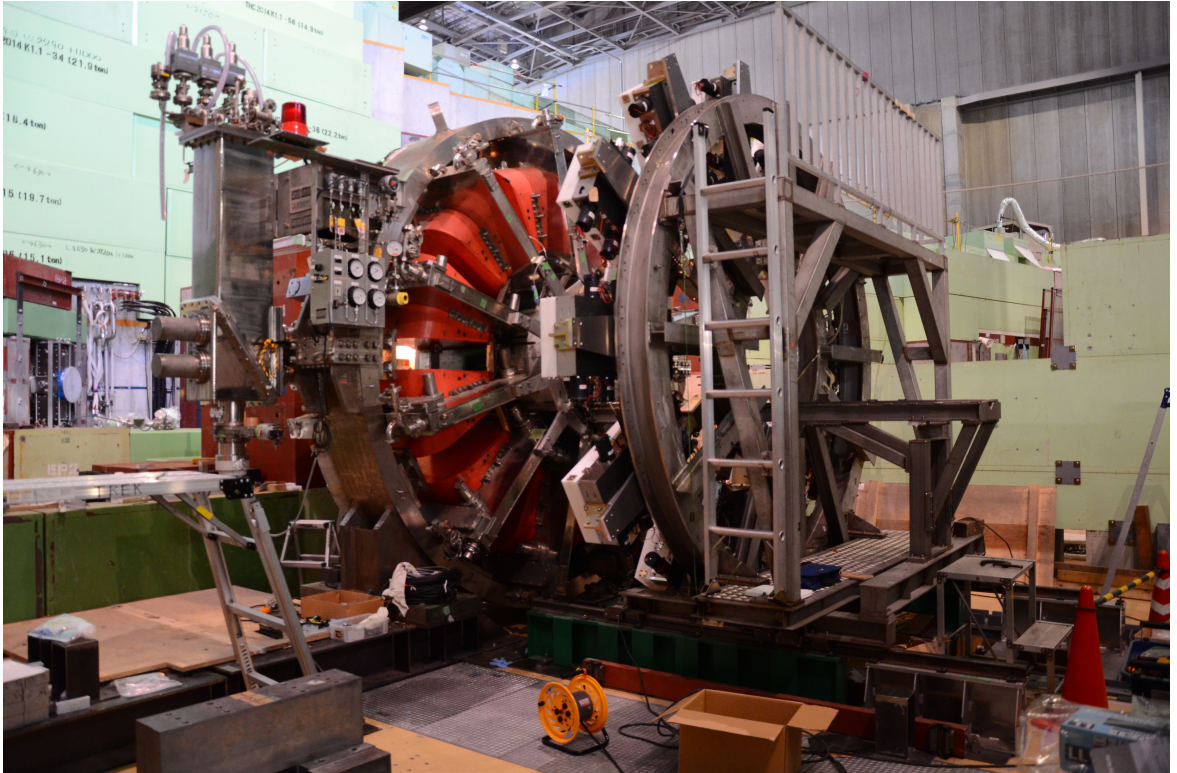


Figure 4.9. Side view of the toroidal magnet and lead glass wheel

High precision was used to manufacture the magnet, in order to obtain good 12-fold rotational symmetry [96]. The number of sectors, 12, was determined by optimizing the solid angle of acceptance and the magnetic field strength [102]. Each sector had uniform gap dimensions, 20 cm, with a rectangular pole face, 82×76 cm², in the radial and beam-axial directions [102]. In order to realize both a flat and a wide momentum acceptance, quasi-focal plane optics were employed at the gap exit so that a wide momentum range could be covered with relatively small detectors [102]. Each pole gap was equipped with a set of tracking and PID detectors. TOSCA software was used to calculate the three dimensional field map. The value of the magnetic field component along the y-axis, BY, has been evaluated on rectangular area with limits $x = 70$ cm to $x = 150$ cm and $z = -25$ cm to $z = +25$ cm, at the $y = 0$ cm point; i.e. in the middle of the pole gap [103]. The field was superposed of the dipole field from the iron core and the toroidal field from the magnet coils [102].

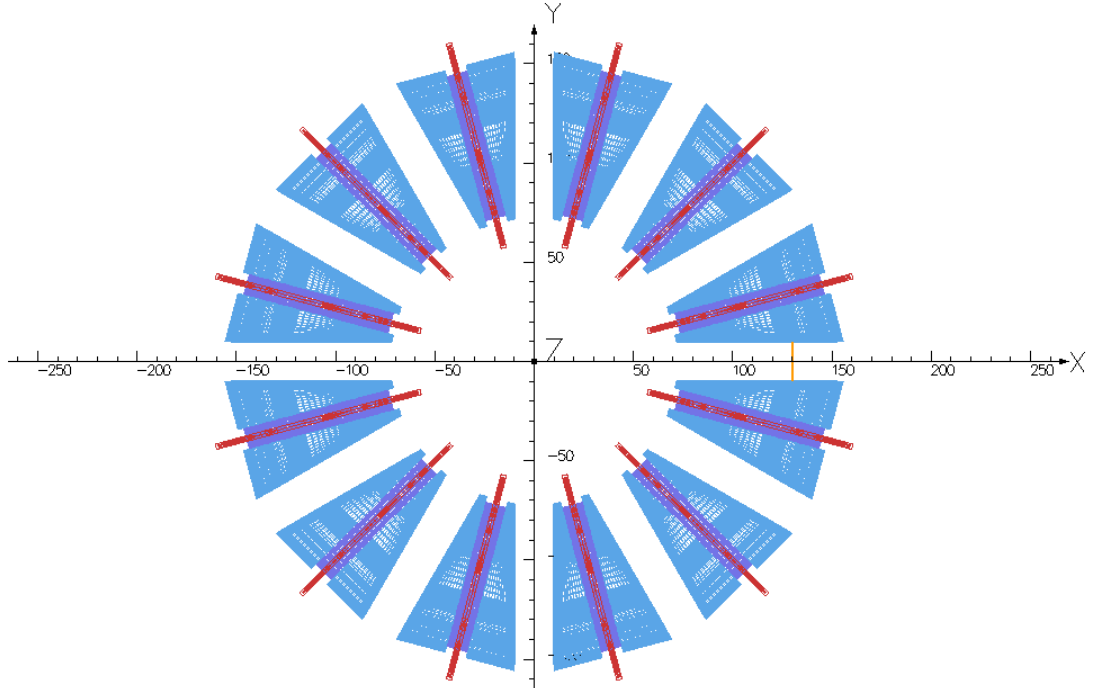


Figure 4.10. Input toroidal geometry for TOSCA calculation of the magnetic field

Figure 4.10 shows the precise input geometry of the toroidal spectrometer which was used to calculate and generate the TOSCA field map. This map was used in both the tracking and simulation software toolkits.

4.6 Gap Veto Counters

Twelve gap veto (GV) counters comprised of a Pb-plastic sandwich were installed at the outer radius of the magnet gaps. GV counters were used to monitor photons passing through the muon gaps in the CsI detector and consequently veto those photons that passed through the magnet gaps [1]. A given GV counter had a thickness of 2.6 radiation lengths and about 40% of the photons that escaped through the magnet gaps were monitored by the GV counters [1].

4.7 Tracking Detectors

Three sets of planar multi-wire proportional chambers (C2, C3 & C4) were installed in each of the 12 toroidal spectrometer gaps. The C2 chambers were installed at the entrance of the magnet gap, and the C3-C4 chambers were installed at the gap exit. A cathode readout was employed in order to save readout space around the chambers as well as offer high position resolution [97]. Each chamber had two sets of cathode planes: one for the azimuthal coordinate and the other for the radial coordinate. Figure 4.11 is a schematic showing the cathode strip orientation with respect to the anode wires.

Gold (Au) coated tungsten (W) anode wires, with a $20\text{ }\mu\text{m}$ diameter, had a 2 mm spacing parallel to the magnet gap median plane in order to provide high position resolution for the cathode plane that measured the most sensitive coordinate for the momentum reconstruction [97]. Cathode strips that ran perpendicular to the anode wires were 9 mm wide, spaced 1 mm apart, and consist of an $18\text{ }\mu\text{m}$ thick Cu coating

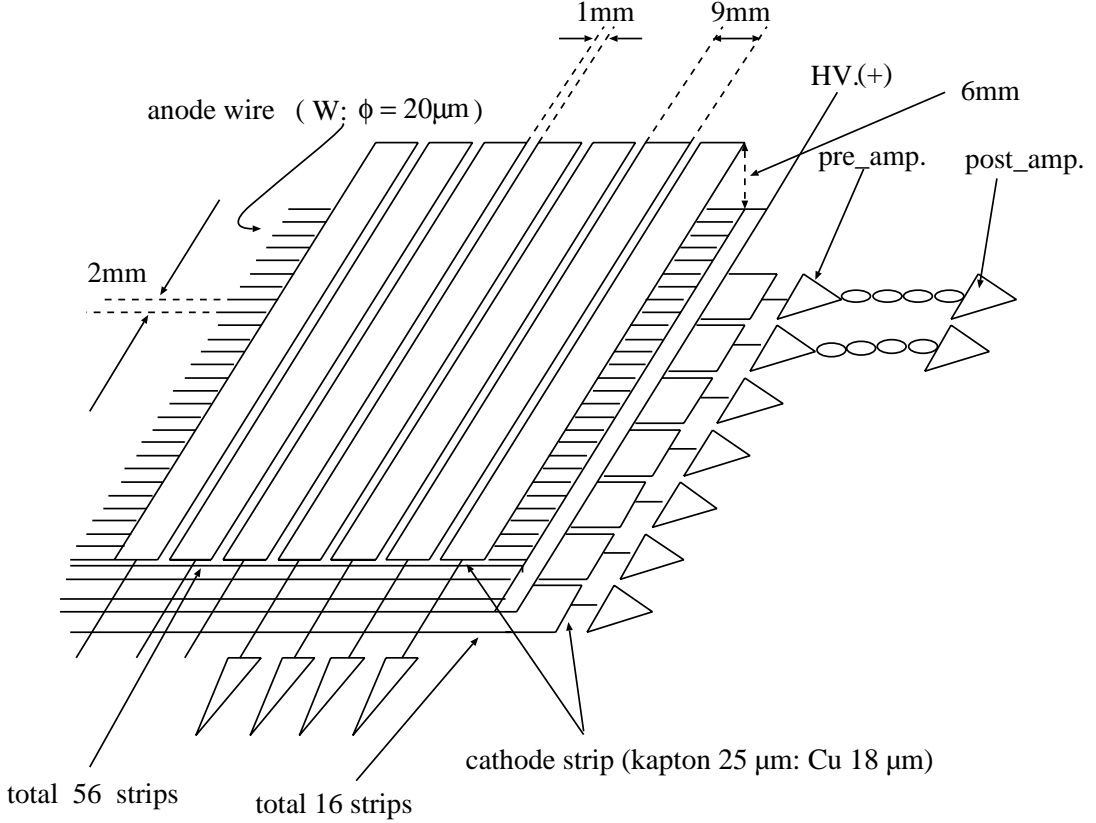


Figure 4.11. Schematic view of the MWPC construction showing the cathode strip orientation with respect to the anode wires.

on Kapton foil [97]. The half gap between the anode and cathode planes was 6 mm [97]. The chambers were operated in proportional mode with a 50:50 Argon (Ar):ethane gas mixture [97]. The three chambers in each gap were connected in series with a gas flow of $30 \text{ cm}^3 \text{ min}^{-1}$ from the gas circulating system [97]. A more complete set of chamber parameters can be found in table 4.5 below [97].

4.8 Lead-Glass Counters

Lead-glass modules used in the TOPAZ experiment at KEK TRISTAN were adopted as lead-glass counters (PGC) for use in the TREK/E36 experiment [21]. A single module has the following dimensions: mass of 26.7 kg, width of $135 \times 113 \text{ mm}^2$

Table 4.5

Parameters of planar C-tracking detectors

Parameters	
Anode wires	20 μm diameter Au coated W
Anode pitch	2 mm
Half gap	6 mm
Cathode strips	9 mm width with 1 mm spacing
Gas mixture	Ar : ethane 50 : 50
Readout	x, y cathode strips
Effective area	
C2	160 \times 560 mm 2
C3	200 \times 640 mm 2
C4	200 \times 720 mm 2

and length of 340 mm [21]. The properties of the lead-glass counter are summarized in table 4.6 below [21].

Table 4.6

Parameters of the lead-glass counters

Lead-glass counter properties	
Mass of module	26.7 kg
Material	SF6W
PMT	Hamamatsu R1652
Size	
Thickness	135 \times 113 mm 2
Length	340 mm

An assembly of 7 modules were stacked in radially behind the TOF2 counters, in each gap. The PGC surfaces were mirror-polished, and a PMT was attached to each module for the Čerenkov photon detection [21]. Čerenkov photons generated

by the e^+ s from K_{e2} decays were produced from multiple e^+e^- pair particles created by electromagnetic showers in the PGC; however the μ^+ s from $K_{\mu 2}$ decays do not generate any shower allowing for further PID discrimination [21]. The total Čerenkov photon yield from an e^+ was expected to be much larger than that from a μ^+ , which would make it possible to separate e^+ from μ^+ as a result of this difference in Čerenkov light yield [21].

CHAPTER 5

GEANT4 GEOMETRY

The TREK/E36 Monte Carlo (MC) simulation toolkit (e36g4MC), developed by the author, is based on ROOT, Geant4 and Python. Geant4 is a high energy physics simulation toolkit for geometry and tracking, and ROOT and Python contain a wealth of scientific data analysis tools. Due to the high precision nature of the TREK/E36 experiment in searching for beyond SM physics as well as rare kaon decay searches for light neutral bosons, it was imperative to thoroughly verify the validity of the e36g4MC toolkit. The work of verifying the e36g4MC, performed by the author and Dr. Tongtong Cao (then at Hampton University), was rather involved and entailed very detailed comparisons between the e36g4MC and the tracking package [104, 105]. The tracking packing was developed by Tongtong as was based on a Kalman Filter algorithm. In order to maintain the object oriented paradigm of C++ in the e36g4MC, the toolkit utilized the ROOT `TObject` class for writing information to the generated ROOT files. This method was used as in order to establish consistency between information storage in experimental and simulation data. Thereby making it possible to analyze experimental and simulation data by using the same analysis routines. This made it possible to perform cross-checks with relative ease as well as utilize the same classes when performing similar analyses in data and simulation. An example of such a ROOT file structure is shown the in figure 5.1 below. In this scheme, various detector classes and their associated class members are represented by the $K+$ `TTree` branches and leaves respectively.

As previously mentioned in section 4.1, the TREK/E36 experiment used a large acceptance spectrometer based on a superconducting toroidal magnet with iron cores, originally designed for hypernuclear spectroscopy and rare decay studies using stopped kaons [101]. The spectrometer geometry and its e36g4MC representation are pre-

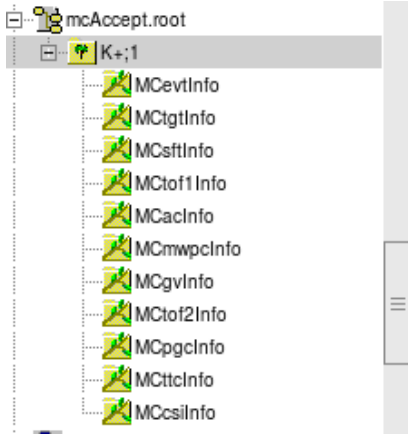


Figure 5.1. Data structure of the *e36g4MC* ROOT file. The leaves store the necessary information for each detector as needed by the user.

sented in figure 5.2. Since the real TREK/E36 geometry was rather complex for a number of detectors, it became necessary to generate these geometries using CAD (computer-aided design) software and the CAD files were subsequently imported into the *e36g4MC* package. Furthermore, correct material assignments were applied for each CAD geometry using the extensive Geant4 materials database. These CAD files were produced by L. Harris, an undergraduate student in the Hampton University Nuclear Physics group.

A custom standalone generator containing eighteen K^+ decay channels was developed by Tongtong [105,106] to assist in by-product searches of light neutral bosons A' . The generator has been fully included into the *e36g4MC* framework, by the author, and served the purpose of ascertaining the width of a given A' search window as a function of its mass $m_{A'}$. The framework of the generator has an important feature used in assigning weights to branching ratios of different channels, i.e.:

- *Real*: assigns the real branching ratios amongst the channels
- *Same*: assigns uniform branching ratios amongst the channels

As a means of further establishing consistency between data and simulation, the misalignment of the C2 detectors described in section B.1 has been fully incorporated

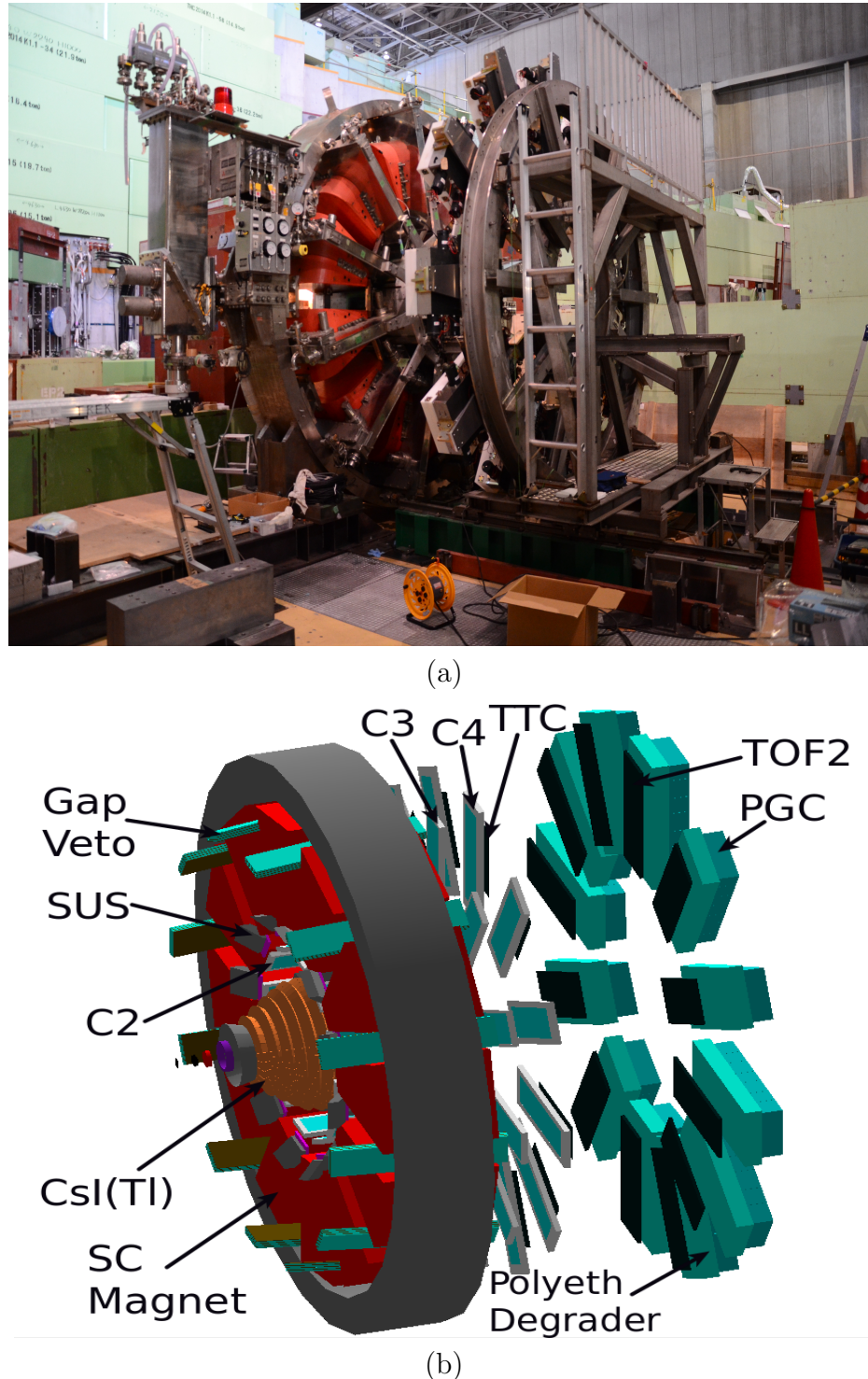


Figure 5.2. The TREK/E36 detector apparatus. The real TREK/E36 geometry (a) and the e36g4MC geometry using Geant4 (b).

into the e36g4MC. The misalignment of the TOF2 counters has also been taken into account in the e36g4MC in order to make it more realistic when compared with the experiment setup.

5.1 Central Detector System

The central detector (CD) system was comprised of the target, spiral fiber trackers (SFT), time of flight scintillators (TOF1), aerogel Čerenkov (AC) and the CsI barrel. The CsI barrel is highly segmented with 768 crystals covering a large solid angle, approximately 75% of 4π and surrounded the stopping target, and was optimized for photon energy in the range of 10 to 250 MeV/ c [97]. This high degree of segmentation allowed for good kinematic resolution for the π^0 's [97]. Figure 5.3 shows the CsI barrel as well as the other CD elements. The e36g4MC geometry of the CsI was developed by S. Strauch and has been thoroughly vetted, by the author, and played an important role in studying the effect of shower-leakage in the CsI detector.

5.1.1 Central Detector: Target

The active target which consisted of 256 fibers was constructed at the TRIUMF national laboratory in Vancouver, BC as mentioned earlier [107]. The high degree of segmentation was carried over into the e36g4MC geometric description of the target, seen in figure 5.4. The fibers were $3.053 \times 3.053 \text{ mm}^2$ and 200 mm in length [108]. The target provided the x and y coordinates of the stopped kaons, as well as the azimuthal angle ϕ of the out-going lepton [107, 108].

Another important geometric feature of the target fibers was the 1.3 mm deep groove into which 1.0 mm wavelength shifting (WLS) fibers were placed. This intricate shape was produced by making use the `G4SubtractionSolid` class from Geant4.

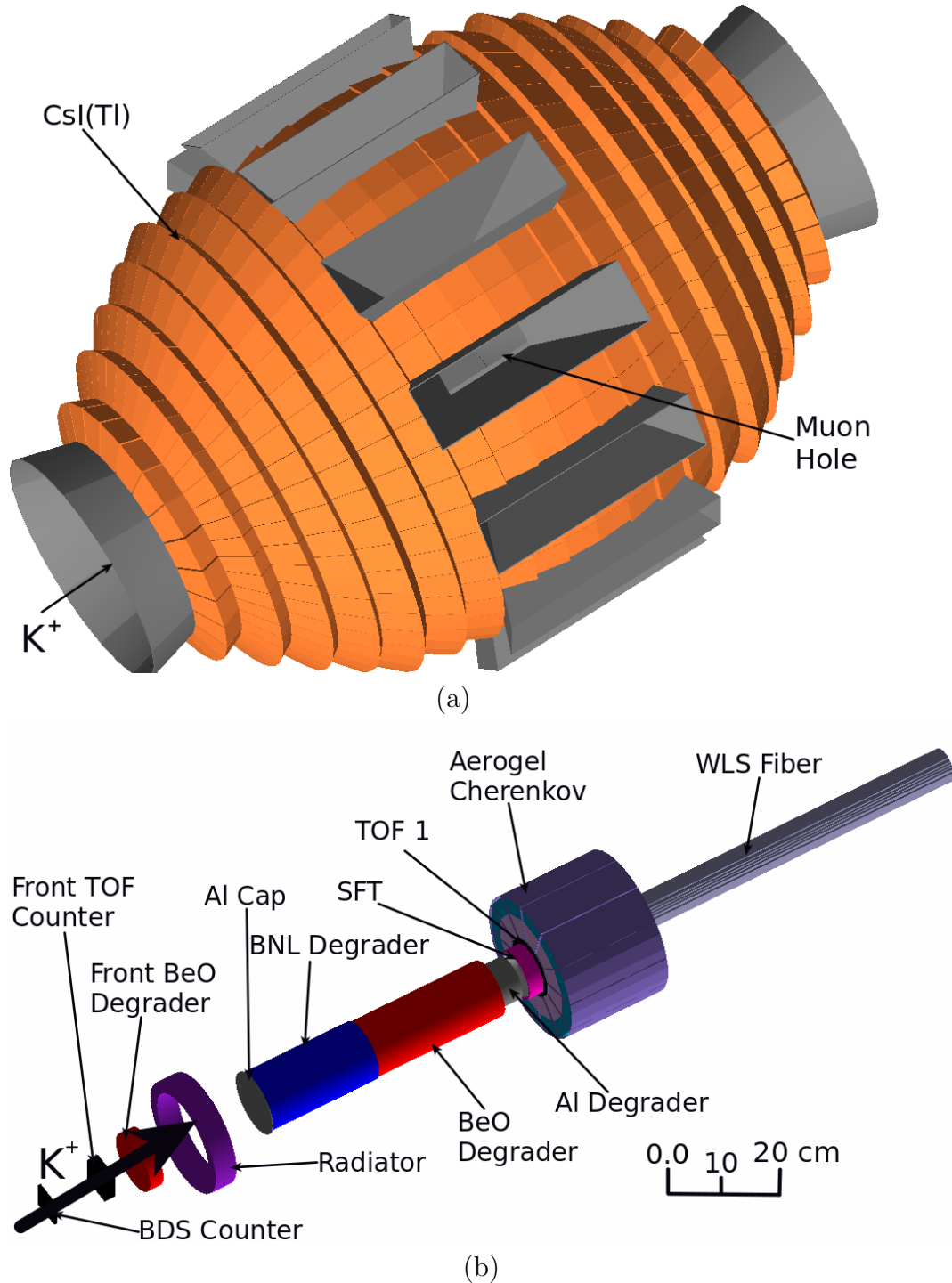


Figure 5.3. The central detector system produced using the e36g4MC. The CsI barrel with all 768 crystals (a) and the geometry that sits inside the calorimeter (b).

This class makes it possible for the *user* to “cut” away sections of a given geometric shape.

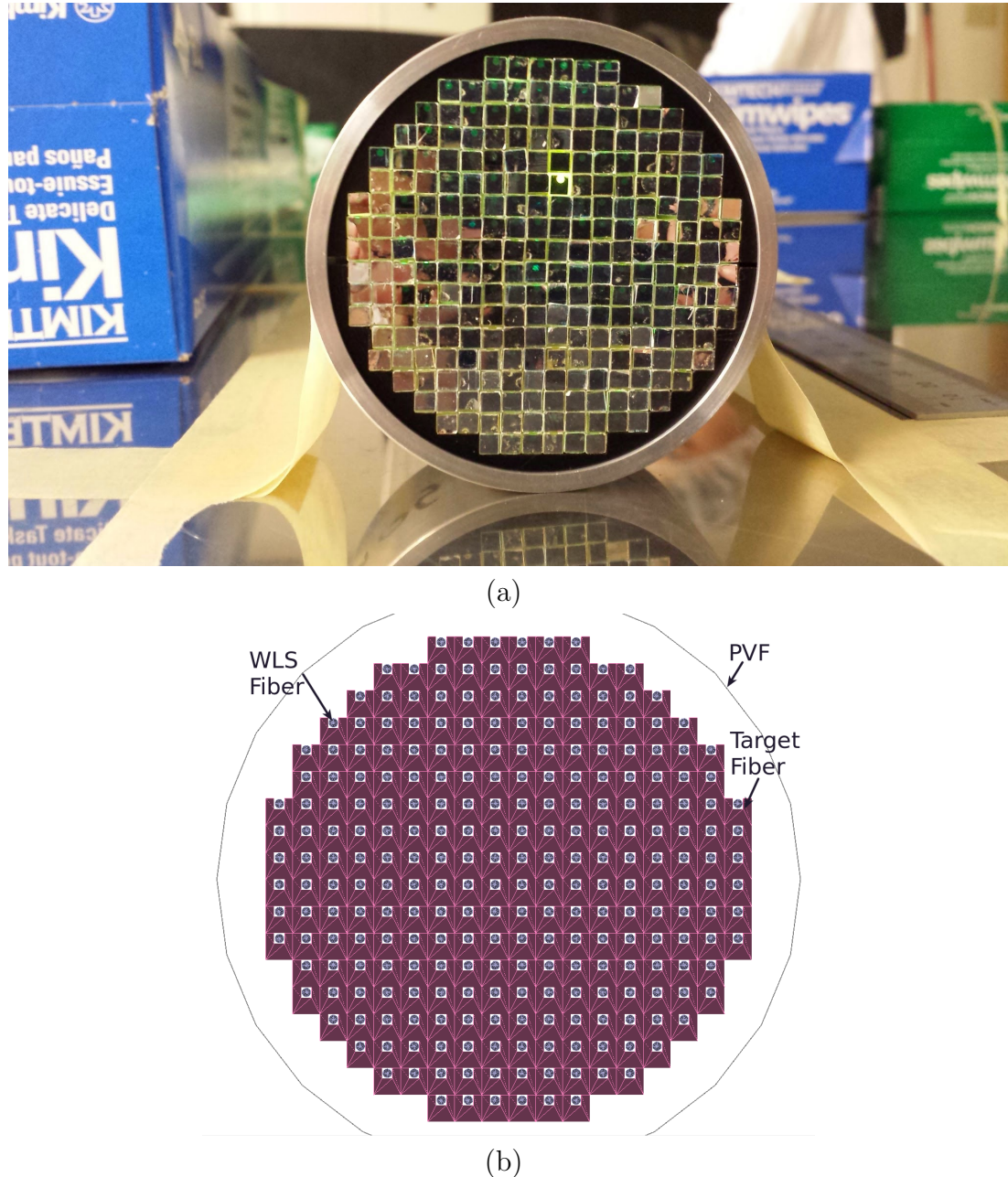


Figure 5.4. The highly segmented target fibers. The real geometry of the TREK/E36 target (a) and (b) shows the e36g4MC target geometry and embedded WLS fibers.

In addition to its already complex geometry, the CD system also consisted of non-trivial elements, namely the polyethylene wrapping around TOF1 for light leakage prevention. Indeed it became necessary to add additional materials to the various

e36g4MC detector descriptions in order to obtain an accurate accounting of the material budget as well as to improve the systematic effects of the CsI barrel. These materials included the target holder and photomultiplier tube (PMT) support geometry which was developed by Dr. Hiroshi Ito and added to the e36g4MC toolkit. The target holder was an Al tube into which the entire target was inserted. This structure is shown in figure 5.5 below.

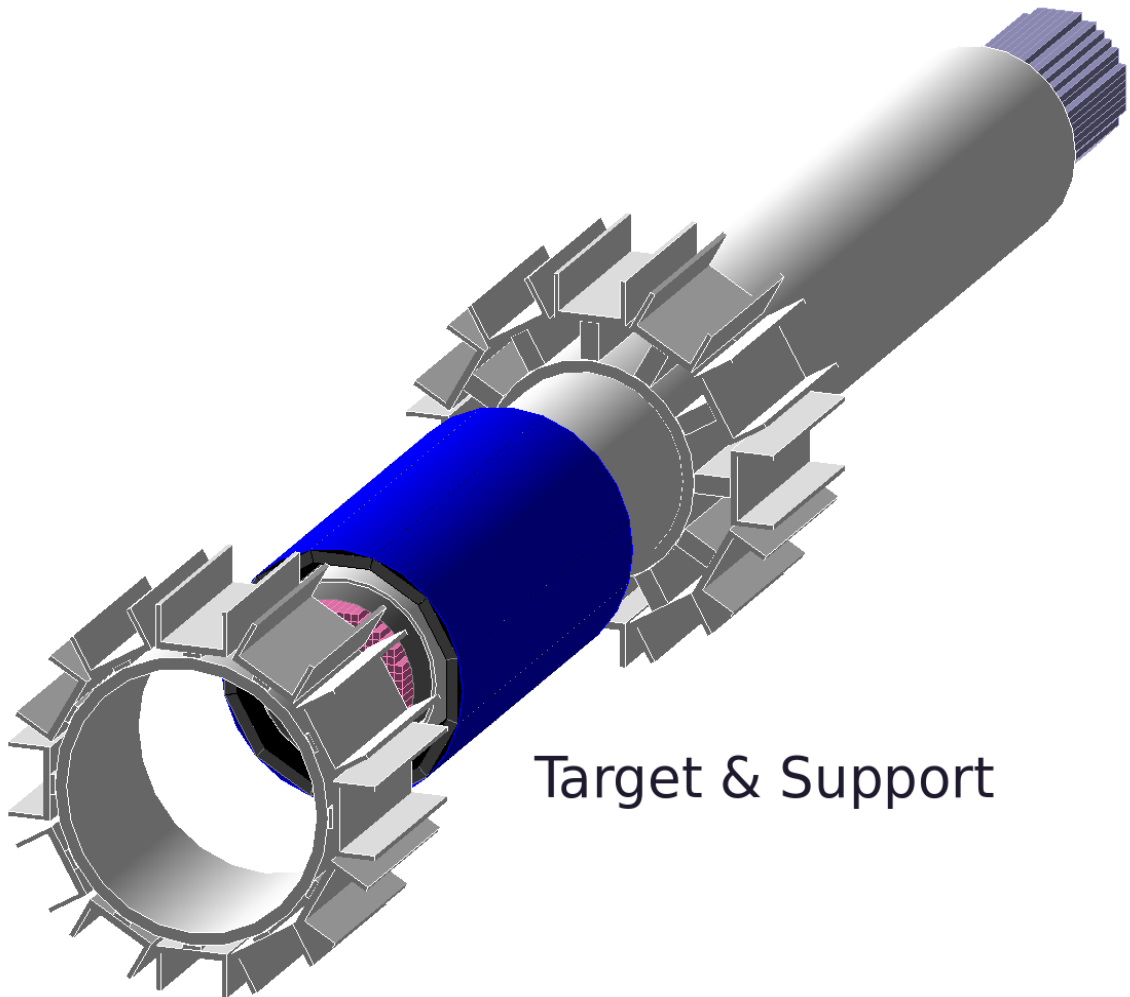


Figure 5.5. Target support. The target and Al target support tube as well as the TOF1 counter.

5.1.2 Central Detector: TOF1

TOF1 was located around the outer layer of the SFT and in conjunction with TOF2, which was located at the exit of the spectrometer after C4 and the thin trigger counter (TTC), provided additional discrimination between e^+ and μ^+ as per the earlier discussion. In order to reduce light leakage in the TOF1 counters, the counters were wrapped in additional polyethylene material. These additional materials were also included in the e36g4MC geometry, shown in figure 5.6 below.

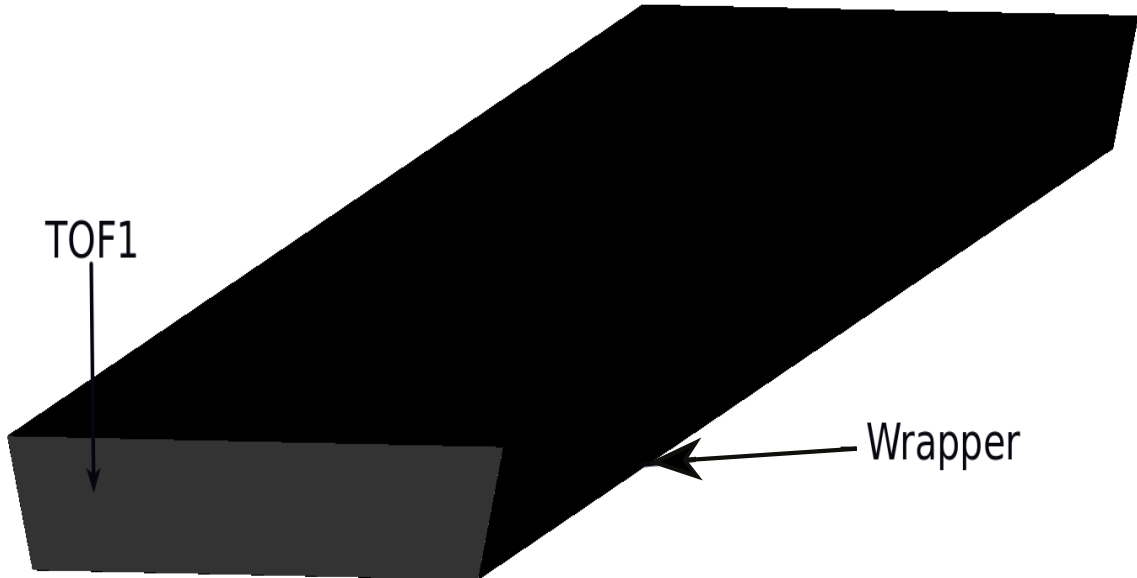


Figure 5.6. TOF1 and wrapping material. A TOF1 counter and the additional polyethylene material demonstrating the accounting of the material budget within the e36g4MC geometries.

5.1.3 Central Detector: AC and AC mirror

The AC detectors were manufactured at Chiba University, using silica aerogel, an amorphous and porous substance comprised of silica (SiO_2) particles and air-filled pores as mentioned above. Given the complicated geometry of the AC components, mirror and mirror support, as well as the AC housing, geometries for these components were produced by utilizing CAD drawing and were subsequently implemented into

the e36g4MC toolkit. Care was taken in order implement the optical properties of the aerogel material by making use of the G4OpticalPhoton class and setting $n = 1.08$. Information on the optical properties of the AC are described in [99]. Figure 5.7 shows the AC and the mirror raised above it (a) and the composite AC-mirror (b).

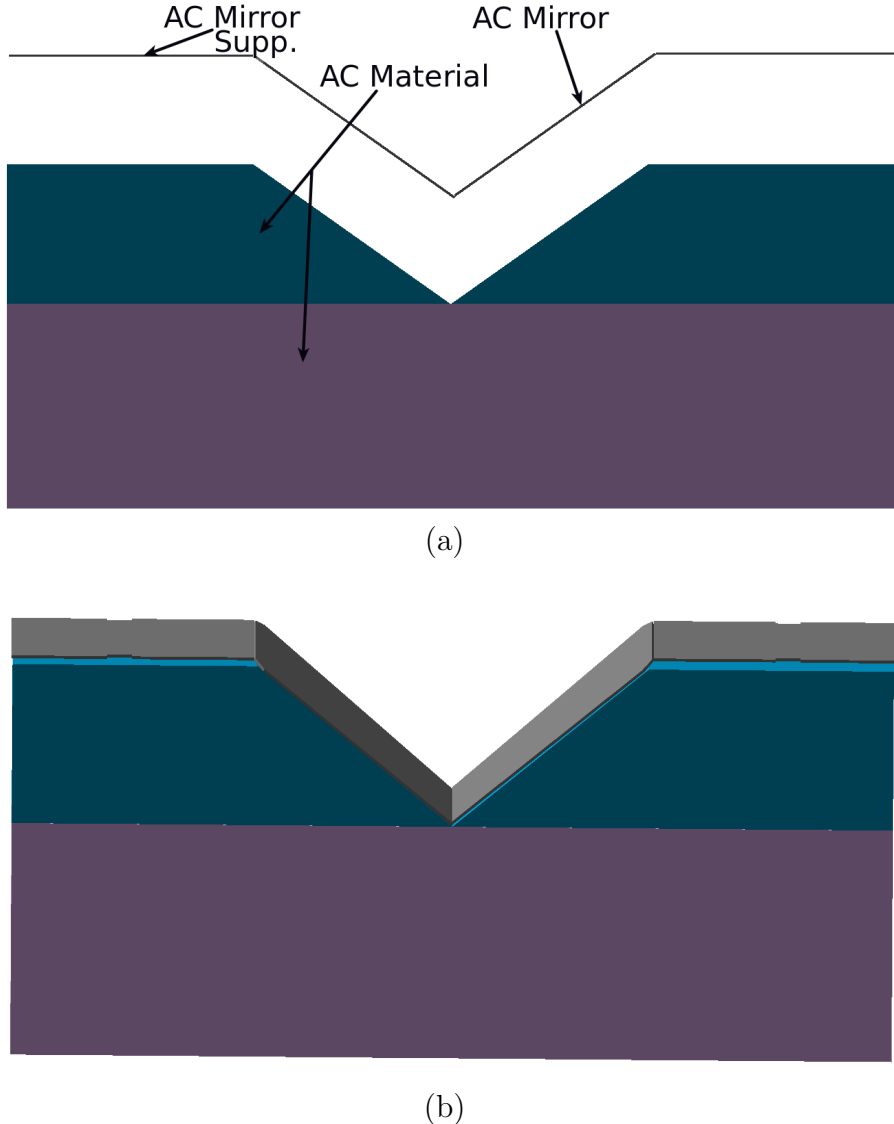


Figure 5.7. The aerogel Čerenkov detector and the mirror. Mirror raised above above the AC (a) and placed neatly on to the AC (b). Due to the complicated nature of the AC mirror, the mirror was produced using a CAD program and that CAD file was imported into e36g4MC.

Table 5.1 shows a summary of the dimensions for the various CD elements and their respective inputs into the e36g4MC and their corresponding real detector counterparts.

Table 5.1

Central detector dimensions

Target fiber dimensions	e36g4MC (mm⁽²⁾)	Real (mm⁽²⁾)
Clear fiber	3.053×3.053	3.053×3.053
Target groove	$200 \times 1.15 \times 1.3$	$200 \times 1.15 \times 1.3$
WLS fiber	1.0	1.0
SFT dimensions		
Fibers	3.7 (thickness) 240.0	3.7 (thickness) 240.0
TOF1 dimensions		
Scintillator	5.0 (thickness) $x_1 = 26.5, x_2 = 23.8$ 188 (length)	5.0 (thickness) $x_1 = 26.5, x_2 = 23.8$ 188 (length)
AC dimensions		
Radiator	40 (thickness) $x_1 = 47.5, x_2 = 6$ 188 (length)	40 (thickness) $x_1 = 47.5, x_2 = 26$ 188 (length)
TOF2 dimensions		
Scintillator	$x = 800, y = 150, z = 20$	$x = 800, y = 150, z = 20$
Gaps 5 & 7	$x = 680, y = 150, z = 20$	$x = 680, y = 150, z = 20$

5.2 Geant4 Verification

5.2.1 Propagation and Magnetic Field

The verification procedure of the e36g4MC was carried in a series of steps, by the author and Tongtong. The first of these steps included the vetting of propagation and implementation of the magnetic field map between the e36g4MC and tracking package. The TREK/36 tracking package is based on the Kalman filter algorithm

which uses an iterative (Runge-Kutta) process from an origin state vector behind the C4 detector to the target and then back to C4 again using a smoothing procedure in order to improve tracked results in the MWPCs [105].

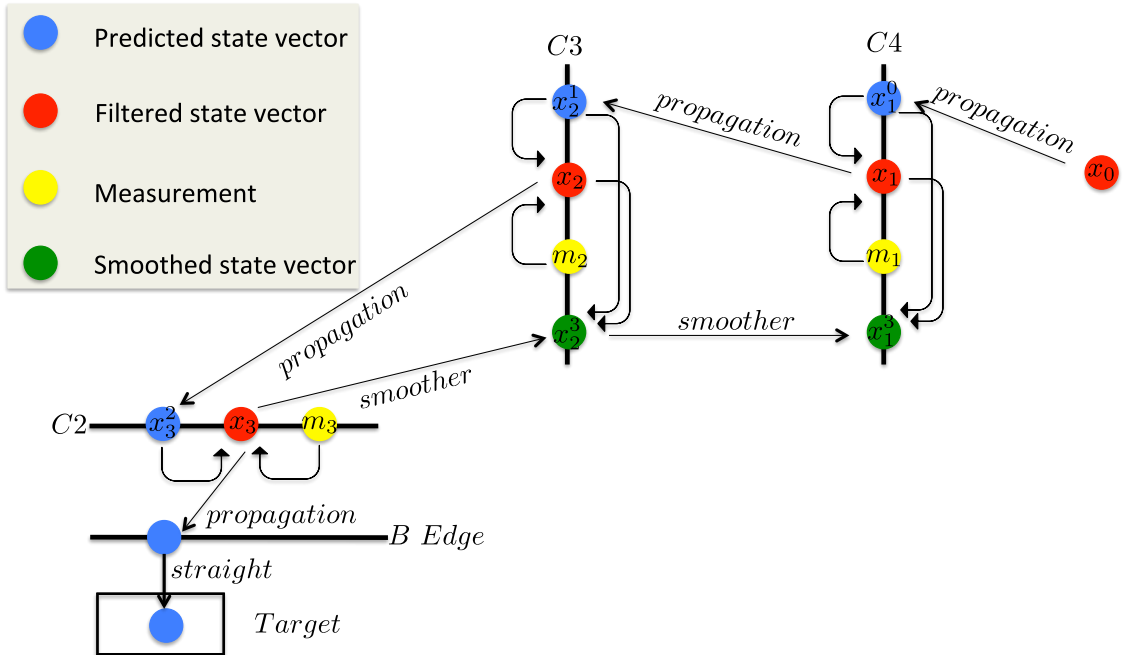


Figure 5.8. Kalman Filter algorithm [105, 106]. A schematic view of the Kalman filter algorithm implementation in the TREK/E36 experiment, which shows a starting state vector point x_0 and propagating to the target and then using a smoother to improve the state vector positions for the various C tracking elements.

In the Kalman filter process, the predicted state vector improves with every Runge-Kutta step and, by using a smoother, a back improvement between measured and calculated state vectors was achieved. For comparisons and verification between the tracking package and the e36g4MC a fictional particle, a *geantino*, which only feels the electromagnetic interaction was propagated in the e36g4MC and the state vector at the vertex as well the state vector at each of the tracking elements was recorded and later back-propagated in the tracking package as shown in figure 5.8 [105, 109]. Both the e36g4MC and tracking package made use of a TOSCA generated external magnetic field map, 3D plot of is shown in figure 5.9 below.

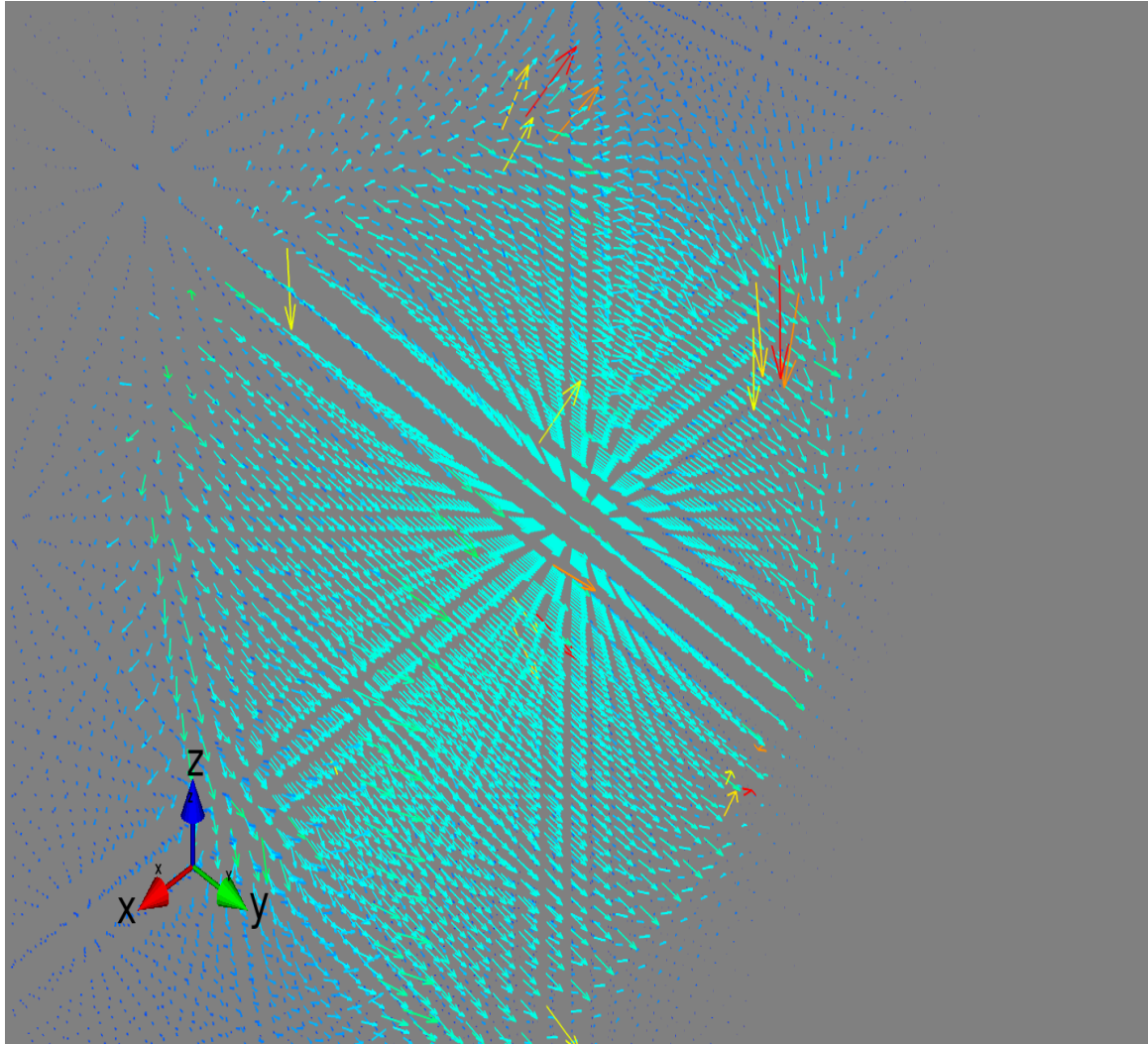


Figure 5.9. TOSCA generated field map. Three dimensional plot of the field map used in both e36g4MC and the tracking package.

The treatment of an external field map required special treatment in Geant4. Geant4 has the capability of describing a variety of fields and propagating the tracks according to user defined accuracy [110]. A Runge-Kutta method for the integration of ordinary differential equations are used in order to propagate a track inside a field. In Geant4, several Runge-Kutta methods are available, and tailored for different conditions. Once a method is chosen to calculate the track's propagation in a specified magnetic field, the curved path is broken up into linear chord segments. For example

if a field map is coarse, a G4RungeKutta3 class is the best option in order to get the correct cord length calculation. In the e36g4MC, the G4SimpleRunge was used because the TOSCA field map was calculated with 1 cm spacing for (x, y, z) . These chord segments are determined so that they approximate the curved path as closely as possible. Figure 5.10 shows a zoomed in version of the μ^+ tracks in the magnetic field.

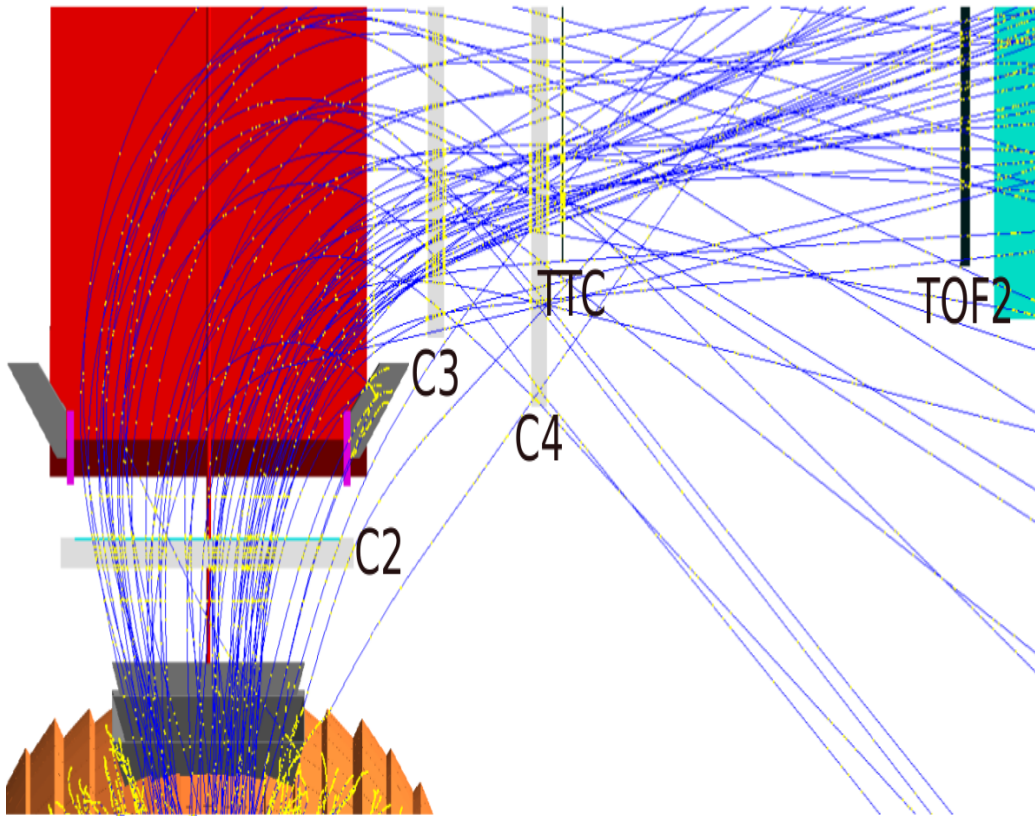


Figure 5.10. Implementation of TOSCA field. Successful implementation of a TOSCA generated toroidal field in the e36g4MC toolkit.

Given the special treatment of an external field map in Geant4, it was imperative to verify that the treatment of the magnetic field between the tracking package and the e36g4MC toolkit were consistent. This was performed by taking the state vector differences at C2, these are defined as differences in position coordinates (x, y, z) and direction cosines (nx, ny, nz) . Remember from figure 5.8 that the starting point

for tracking is just behind C4 and is propagated backwards through the region of magnetic field. For this reason the state vector comparison between the tracking package and the e36g4MC was carried out at C2 [105, 109].

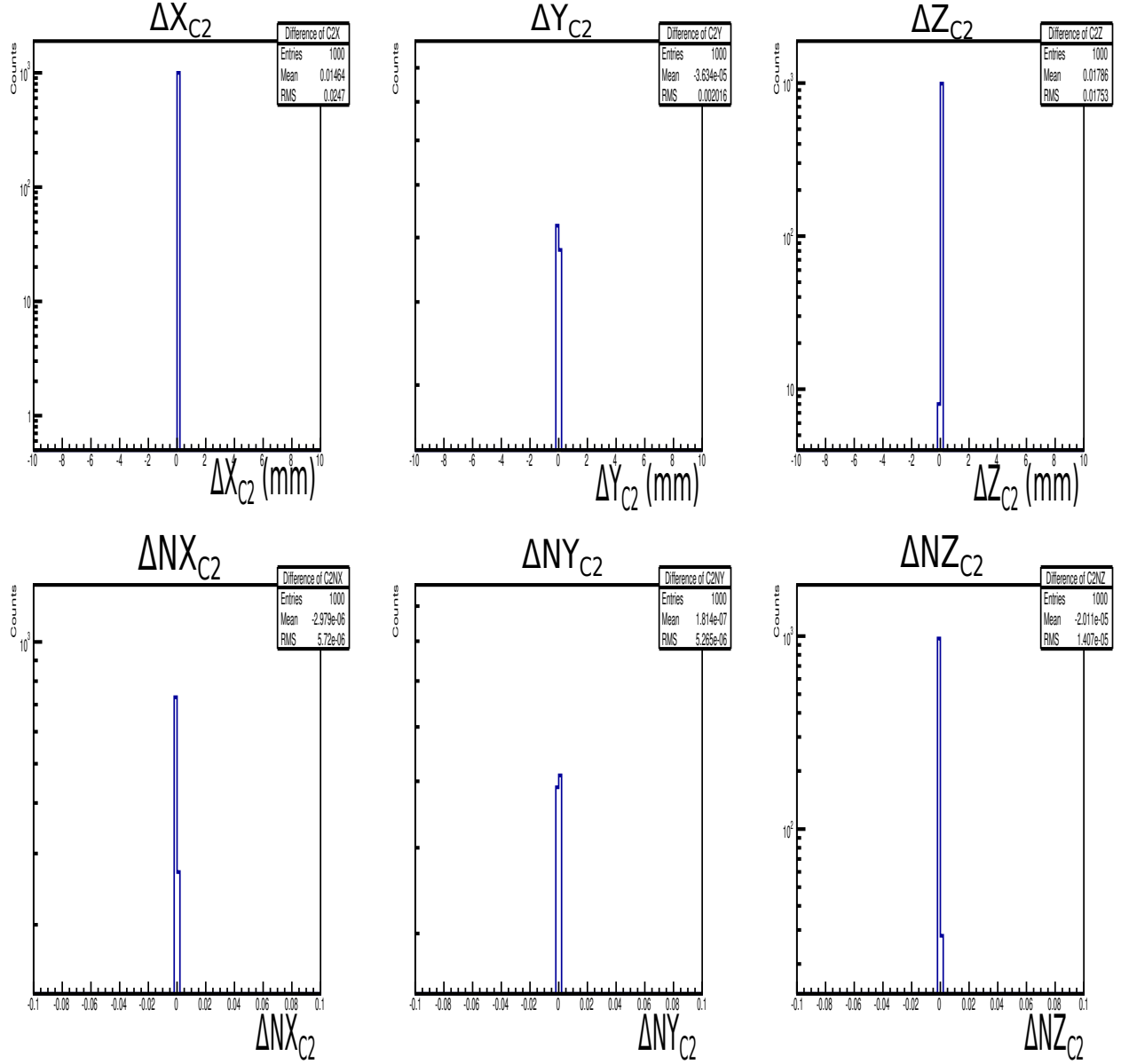


Figure 5.11. Geantino state vector evaluation. The differences in state vector at C2 between the tracking package and the e36g4MC toolkit, evaluated with geantino simulated data. The top panel shows the differences of C2 position coordinates (ΔX , ΔY , ΔZ), and the bottom plane shows the differences of direction cosines (ΔNX , ΔNY , ΔNZ). This result helped to establish that the propagation and treatment of the magnetic field in both packages are consistent.

The comparison process was as follows:

- Generated a simulation data sample and saved the information for the C tracking elements
- Used state vectors from simulation as the initial state vectors in the tracking package
- Back-propagated from just behind C4 to C2 using tracking package
- Compared results between simulation and those reconstructed by tracking
- A separate single event with all detailed information of all the Runge-Kutta steps was generated for more thorough comparison

The results in figure 5.11 show the difference between simulation and reconstructed *geantino* state vector evaluation at C2, which were found to be centered at zero for both the top and bottom panels. The top panel shows the differences of C2 position coordinates ($\Delta X, \Delta Y, \Delta Z$), and the bottom plane shows the differences of direction cosines ($\Delta NX, \Delta NY, \Delta NZ$). These results helped to verify that the treatment of the magnetic field as well as propagation in both the tracking and e36g4MC packages are consistent [106, 109]. further, these results demonstrated that the magnetic field map was the same in the tracking and e36g4MC packages. As mentioned, the *geantino* does not undergo physics processes of energy loss and multiple scattering, save for electromagnetism and it was therefore crucial in establishing the consistency of propagation and magnetic field implementation.

5.2.2 Multiple Scattering

Upon verifying the consistency of the magnetic field map used by both the tracking package and the e36g4MC packages, and further that the evaluation and propagation of particles in the magnetic field were also consistent, studies of multiple scattering and energy loss were carried out. The μ^+ was the charged particle used in this study because the $K_{\mu 2}$ decay is the predominant decay for the kaon. Elastic scattering of charged particles is an important feature of transport codes and Geant4 contains

several multiple scattering methods depending on situation at hand [110]. Most particle physics tracking and simulation codes use multiple scattering theories of Molière [111], and/or the Goudsmit and Saunderson [112]. The theory of Molière gives only an angular distribution after a given average path length which made it amenable for use in the tracking package accounting for additional noise during propagation. Geant4, on the other hand, uses mixed algorithms for calculating multiple scattering: Molière, Goudsmit-Saunderson, and Highland [113] theories are used when necessary as a correction to angular distributions and improved accuracy in high z-materials.

The treatment of multiple scattering between the tracking package and the e36g4MC are fundamentally different. In the tracking package, multiple scattering was based on the Molière theory, and was accounted for as additional noise, taken into account as small angular variations as calculated in equation 5.2.1

$$\theta_{ms} = \frac{13.6}{\beta p} z \sqrt{\frac{s}{X_0}} \left(1 + 0.038 \ln \left(\frac{s}{X_0} \right) \right) \quad (5.2.1)$$

where β , p , z are the velocity, momentum and charge of the incident particle, and s/X_0 is the true path length per radiation length [109]. This noise term, θ_{ms} , was then applied in the Kalman filter equations in order to improve the state vectors at given evaluation points (detectors). On the other hand, in the e36g4MC multiple scattering was accounted for stochastically along the particles' trajectory by computing the mean path length correction and the mean lateral displacement [114]. Figure 5.12 above shows a comparison between the tracking package, dotted curve, and the e36g4MC, solid curve. For the tracking package, the dotted curve was produced from C4 to C2, whereas for the e36g4MC, the solid curve was produced from the TTC to the target. The curves show good agreement, save for the region of magnetic field due to the differences in the treatment of multiple scattering between the two packages.

Further analysis of simulation and reconstructed state vector differences evaluated at C2 with $K_{\mu 2}$ muons, was carried out by studying the effects of turning various

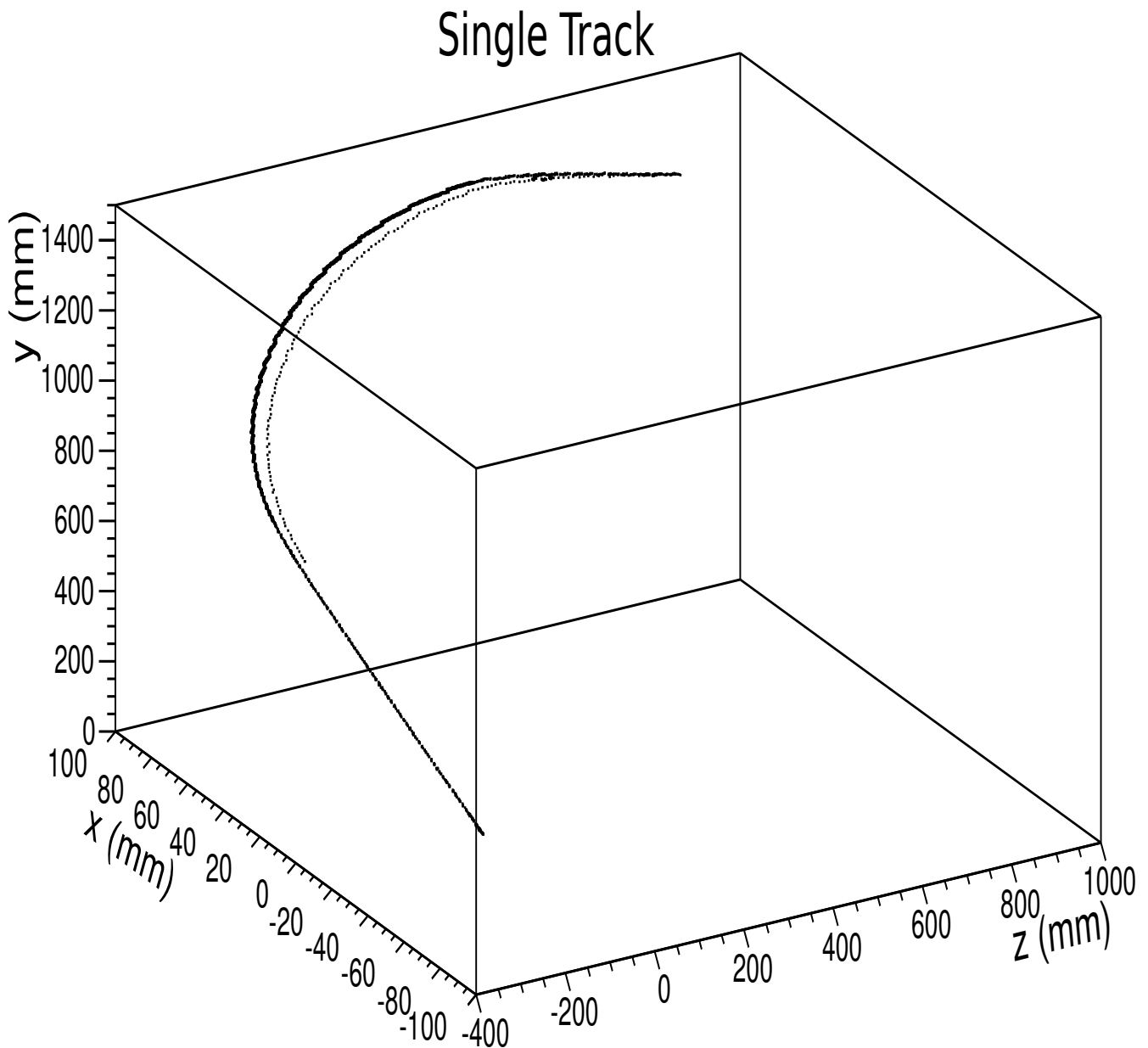


Figure 5.12. Single Track. Single track event trajectory for the tracking package, dotted line, and e36g4MC, solid line. Both tracks used simulation data and the dotted line was reconstructed using simulation data and plotted from C2 to C4 tracking elements [109].

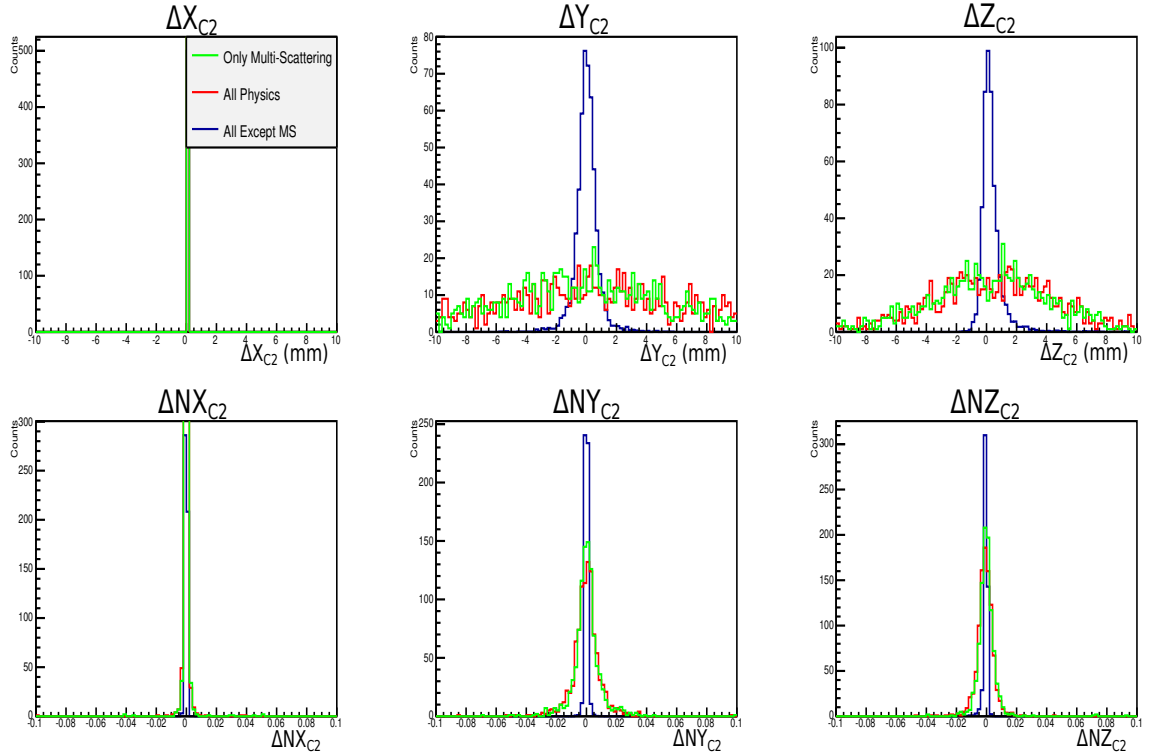


Figure 5.13. Physics comparison. State vector differences evaluated at C2 with $K_{\mu 2}$ muons, was carried out by studying the effects of turning various physics processes on and off: all physics turned on (red), multiple scattering turned off (blue) and only multiple scattering turned on (green), between the tracking package and the e36g4MC toolkit.

physics processes on and off: all physics turned on (red), multiple scattering turned off (blue) and only multiple scattering turned on (green), the results are shown in figure 5.13. The case for all physics represents the processes of ionization, multiple scattering, pair-production and bremsstrahlung. These results all show Gaussian distributions with mean values around zero, indicating that the physics treatment are consistent between the two packages. It can be concluded that multiple scattering was the main reason behind the differences in position and direction, up to a few centimeters. This meant further that multiple scattering could not be ignored in the tracking package, and figure 5.12 shows clearly the difference in path length due to multiple scattering, the solid line is a single event simulation from the e36g4MC and

dotted line is the reconstructed track. Notice that the curvature of the solid line is larger, possibly due the stochastic treatment of multiple scattering in Geant4, which can have noticeable deviations in energy loss evaluation between the two packages.

5.2.3 Energy Loss

The tracking package used effective material properties as a means of accounting for the material budget, whereas the e36g4MC aimed to account for the detailed materials as discussed before. This meant that in the tracking package, the effective material properties for the detectors were calculated based on mass-weights of particular layers which represented different materials through which a charged particle traversed. In the e36g4MC toolkit, however, the particles traveled through detectors layer by layer. Energy loss through material is calculated using the Bethe-Bloch formula [8]

$$-\frac{dE}{dx} = K z^2 \frac{Z}{A} \frac{1}{\beta^2} \left[\frac{1}{2} \ln \left(\frac{2m_e c^2 \beta^2 \gamma^2 T_{max}}{I^2} \right) - \beta^2 - \frac{\delta(\beta\gamma)}{2} \right] \quad (5.2.2)$$

Equation 5.2.2 was used to calculate the mean energy loss in the tracking package. In Geant4, the mean energy loss is also evaluated with Beth-Bloch formula while also making use of sophisticated algorithms to sample energy loss fluctuations as a particle travels through material [114–117]. Figure 5.14 shows the stopping power $-dE/dx$ of a μ^+ travelling in copper as at different momenta.

Positively charged muons in the TREK/E36 experiment, lies in the minimum ionizing region of the Bethe-Bloch method to account for energy loss. This effect was used to sanity check the e36g4MC package, by comparing the energy loss between C2 and C4 for the cases when:

1. Only ionization process is turned on in the simulation

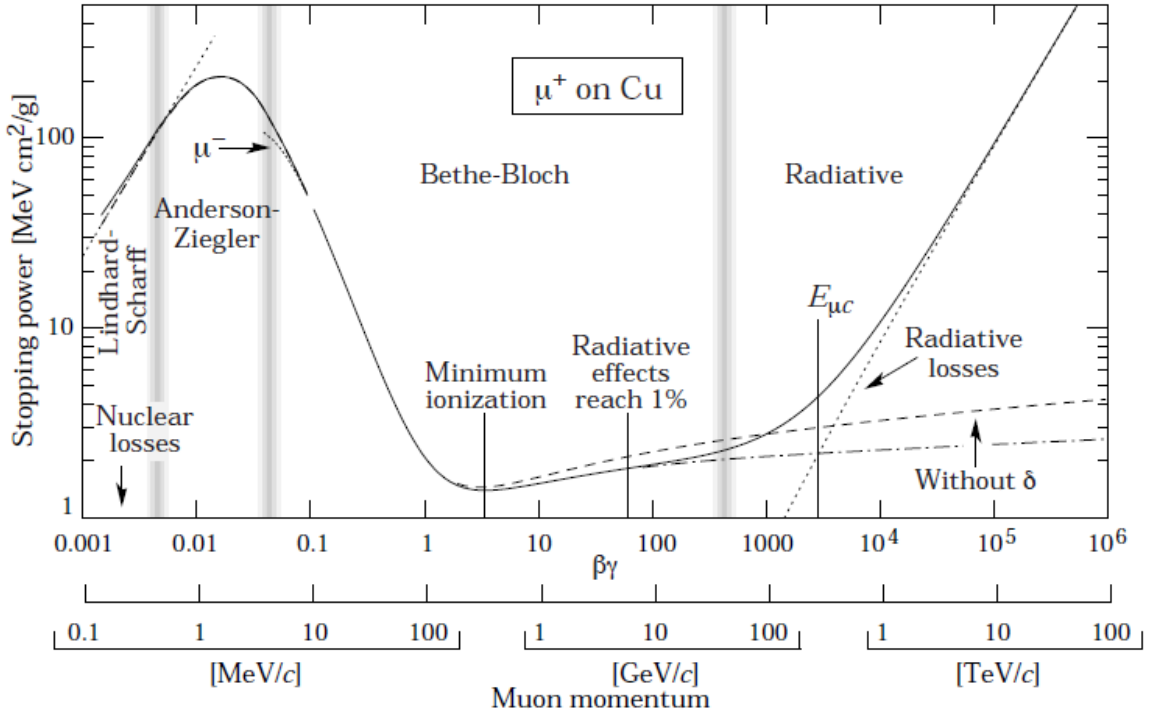


Figure 5.14. Geant4 energy loss. Stopping power ($-dE/dx$) for positive muons in copper as a function of $\beta\gamma = p/Mc$ over nine orders of magnitude. Solid curves indicate the total stopping power. Data below the break at $\beta\gamma \approx 0.1$ are taken from bands indicate boundaries between different approximations discussed in the text. The short dotted line labeled “ μ^- ” illustrate the “Barkas effect”, the dependence of stopping power on the projectile charge at very low energies [8].

2. Only ionization and bremsstrahlung process are turned on

Figure 5.15 shows that for μ^+ there is no observable difference between energy loss due to ionization and energy loss due to both ionization and bremsstrahlung, which is the expected result as this is the minimum ionizing region for muons.

In the e36g4MC the energy loss of muons is computed by the Geant4 class G4VMuEnergyLoss [117]. In Geant4, the energy loss for a charged particle is a stochastic quantity described in terms of a straggling function. The μ^+ mean energy loss during a step was computed as follows [110]

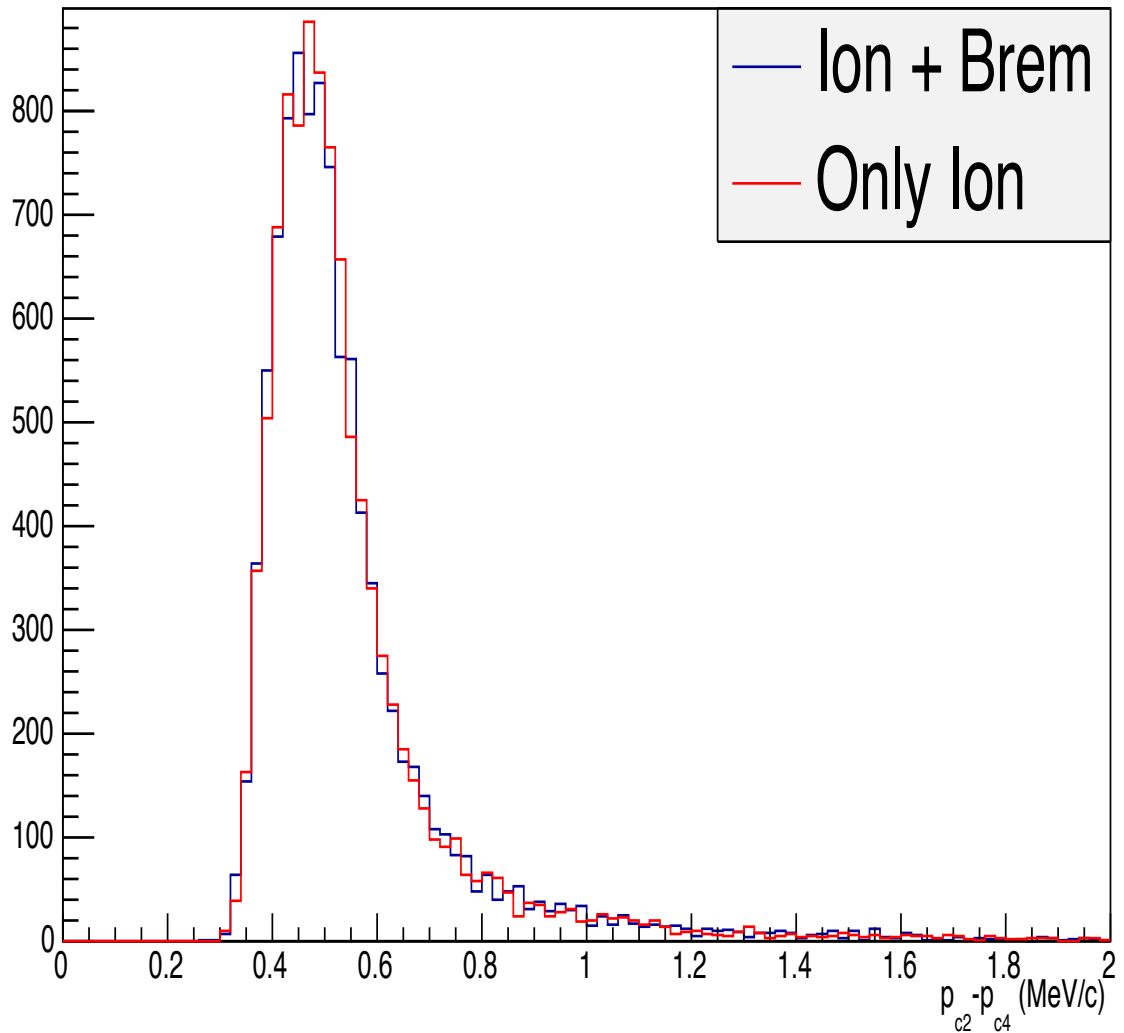


Figure 5.15. Energy loss in the e36g4MC. Comparison of energy loss due to only ionization (red) and energy loss due to both ionization and bremsstrahlung (blue). For heavy particles like μ^+ only energy due to ionization is considered thereby explaining the consistency between the red and blue histograms, because energy loss due to radiation is negligible.

$$\Delta T = T(r_0) - T(r_0 - s), \quad (5.2.3)$$

where T is the μ^+ kinetic energy, r_0 is the range at the beginning of the step of length s . In the case for which $s < \kappa r_0$, where κ is an arbitrary parameter (the *linear loss limit*), an approximation is used [110, 118]:

$$\Delta T \approx s \left| \frac{dE}{dx} \right|.$$

Since in the TREK/E36, the μ^+ energy loss lies in the minimum ionizing region, a sanity check was conducted by taking into account both ionization and radiation. In the tracking package, only ionization was considered. Figure 5.15 shows the negligible difference in energy loss for μ^+ between C2 and C4, when radiation energy loss was taken into account, resulting in a mere minute deviation.

The discussion from the previous paragraph entailed only comparison of energy loss due to radiation-ionization and that due to only ionization for μ^+ in the e36g4MC. A comparison and correction in momentum at C4 between the tracking package and the e36g4MC was also carried out. For the correction, an anode plane was replaced with anode wire in the e36g4MC. This picture is shown in figure 5.16

The density of the anode is very large, so even if it is thin, the resulting energy loss due to the anode is large, ≈ 0.1 MeV. For the MWPCs used in the TREK/E36 experiment, the anode plane was made up of individual anode wires and was therefore not a solid plane. In the tracking package, an effective density was used in lieu of the anode wires and was less than the real density of the actual anode wires. The effective density was calculated as

$$\delta_{eff} = \delta_{real} \cdot \frac{V_{anodeW}}{V_{plane}}, \quad (5.2.4)$$

where δ_{real} is the actual density of an anode wire, V_{anodeW} is the volume of an anode wire and V_{plane} is the volume of the anode plane. Figure 5.17 shows the improvement in energy loss once the anode planes were replaced with anode wires in

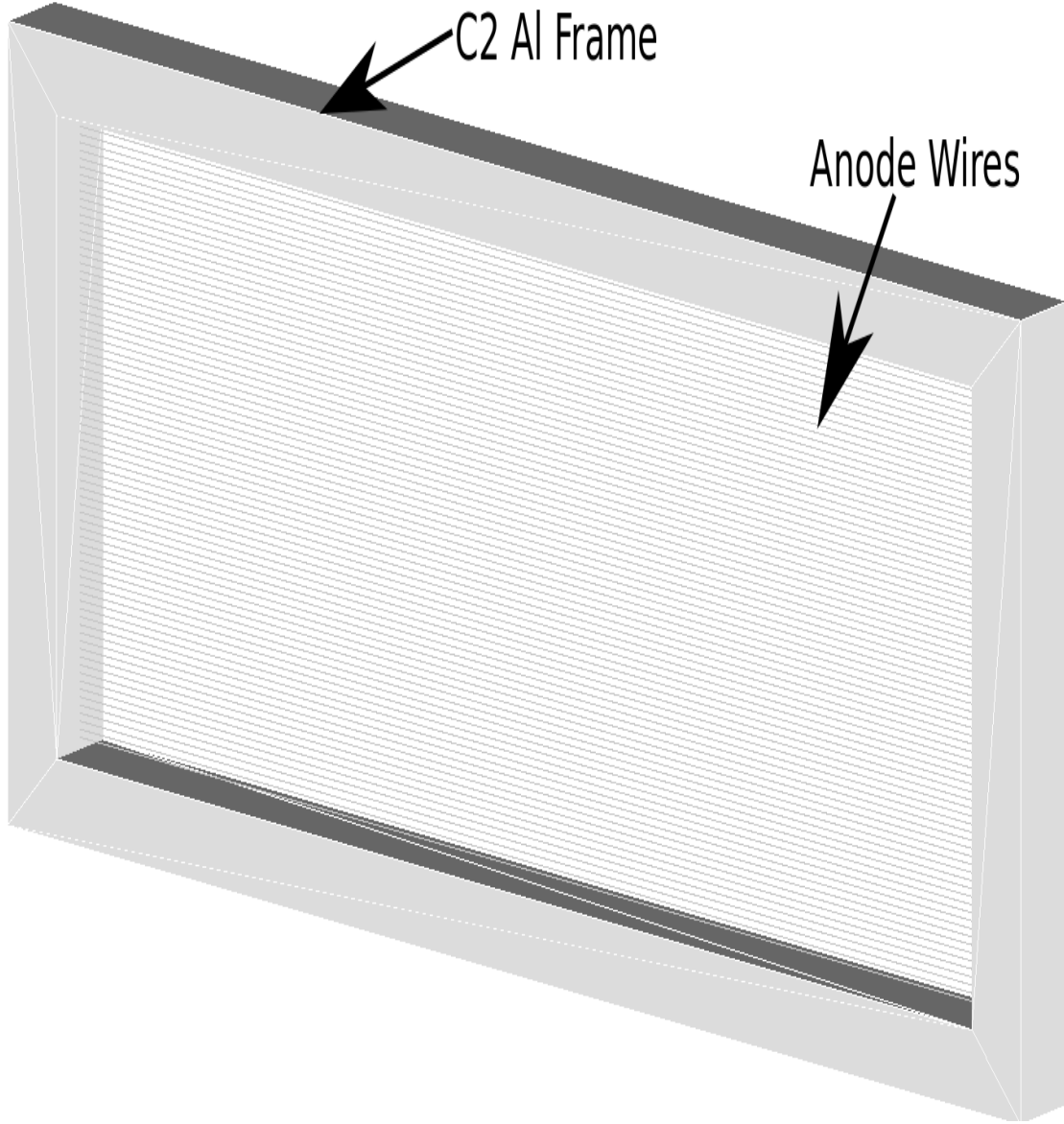


Figure 5.16. C2 anode wires. Anode planes were replaced with anode wires in all the C tracking elements in order to correct for the discrepancy in energy loss between the tracking the package and the e36g4MC.

the e36g4MC. To test the improvement of the anode wires, the momentum difference at C2 between the tracking the package and the e36g4MC. To reiterate, in the tracking package, propagation started just behind the C4 and ended at the target. Since there is only air, a magnetic field and C3, between C4 and C2, the energy loss at C2 became rather simple and the only deviation would be due to the anode planes. In

figure 5.17 it is clear that the energy loss due to the anode plane was non-negligible. The observed long tail at the low momentum end in both figure 5.17 (a) and (b) was due to the continuous stochastic energy loss in the e36g4MC as previously discussed. Due to the conversion of the anode plane into anode wires, the mean difference in momentum Δp at C2 between the tracking package and the e36g4MC is centered at zero. Again, this study used data from the simulation, which was then reconstructed through propagation in the tracking package, in order to ensure that comparison was fair and could be controlled.

Given this good agreement in energy loss between the tracking package and the e36g4MC, it was clear that for the central detector system the material budget was well accounted for in the e36g4MC. Furthermore, the consistency in propagation, magnetic field map and transport methods helped confirm the validity and efficacy of the e36g4MC.

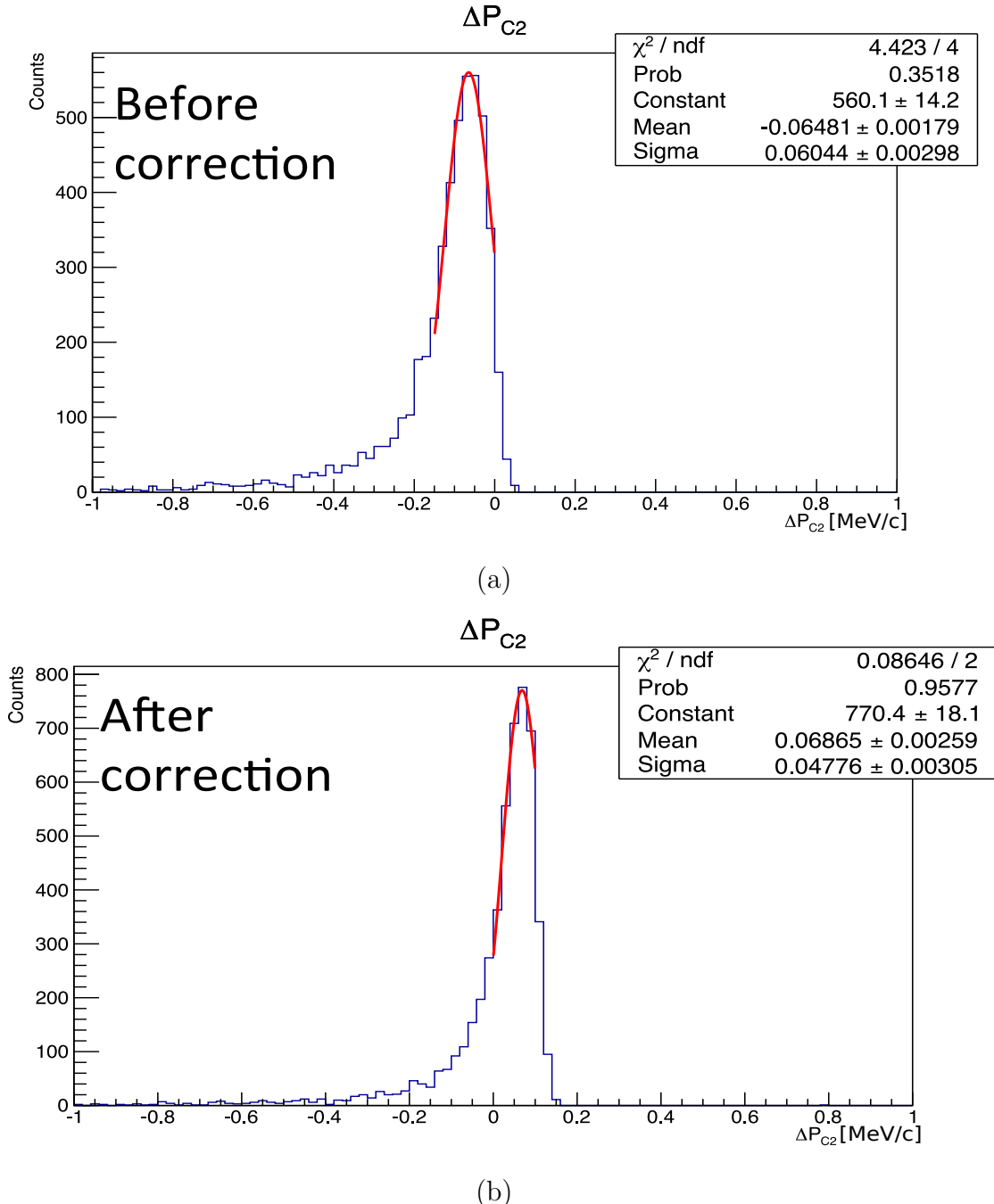


Figure 5.17. Energy loss correction. In (a) the energy loss discrepancy between the tracking package and the e36g4MC before the anode plane was replaced with anode wires in the e36g4MC. In (b) the energy loss correction after anode wires were used in the e36g4MC, and the energy loss has improved as a result.

CHAPTER 6

CALIBRATION AND DATA ANALYSIS

6.1 Overview

In this chapter the tools and techniques used for data analysis will be discussed. The analysis framework employed for the TREK/E36 (`Cooker`) is a C++ and ROOT toolkit that uses XML recipes to drive various analysis and calibration plugins. Originally developed for OLYMPUS, `Cooker` is currently being used to calibrate and analyze TREK/E36 data. Data from the CsI was stored as a waveform, and a mathematical function was deployed to fit these waveforms in order to extract the information necessary for calibration and data analysis. The CsI calibration used the $K_{\mu 2}$ channel because the energy of the muon is monochromatic and the muon deposits all its energy into the a given crystal without showering. A cross-check of the calibration was performed by studying pre-selected π^0 's from the known K_{pi2} momentum region.

The author performed the calibration and data analysis of the CsI(Tl) detector, as well as the *ab initio* development of all the source codes pursuant to completing those tasks.

6.2 Cooker Framework

`Cooker` was developed by Dr. Jan C. Bernauer for the OLYMPUS experiment [119] and has been used for analysis in the DarkLight experiment [120], and MUSE [121]. `Cooker` has an interface to ROOT libraries (histograms, ntuples, etc.) as well as to Boost libraries. Each detector element had an associated `class` for storing raw data; these independent `classes` were then merged into a `TTree` as `TBranch` objects, and the detector variables were stored as `TLeaf` objects (`ntuples`). Data processing

in `Cooker` was arranged according to a two tier system of analysis, low-level (detector calibration procedures) and higher-level (tracking, CsI cluster analysis, etc.) plugins. The `Cooker` framework made it easy to merge both low-level detector calibration plugin as well as high-level tracking plugin in order perform cluster analysis for the CsI.

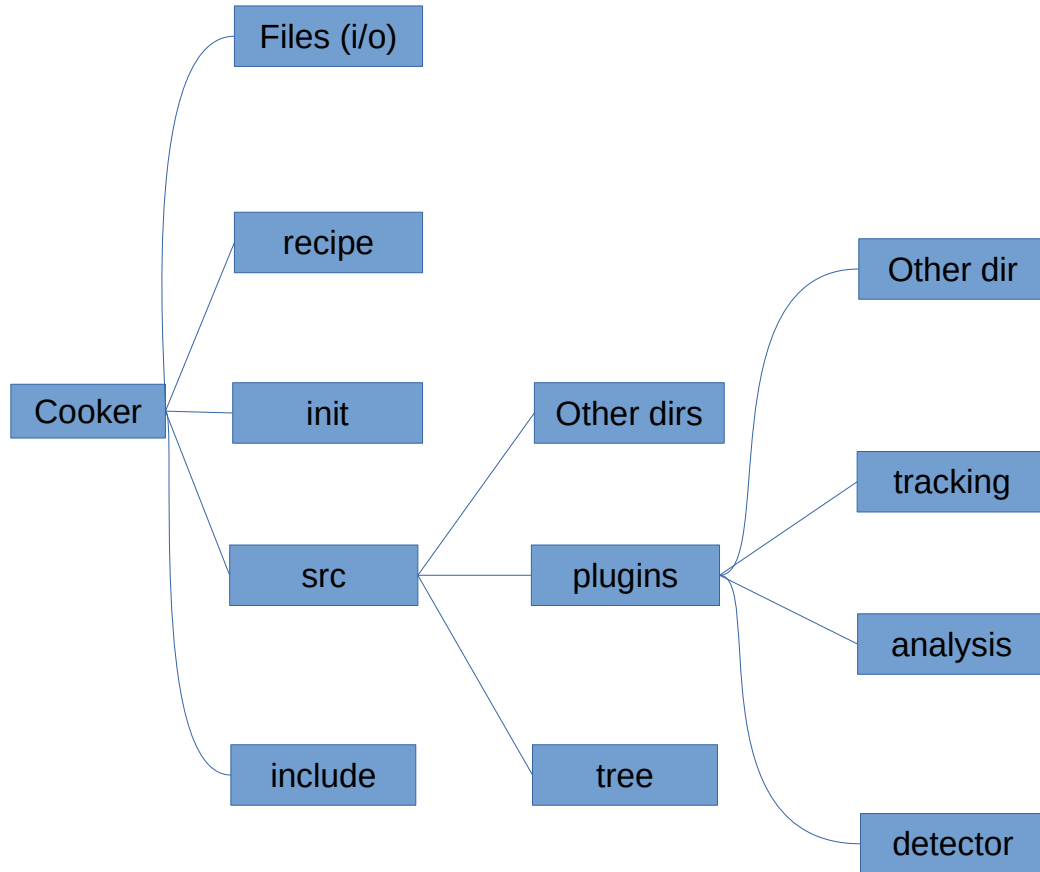


Figure 6.1. `Cooker` structure overview showing directory hierarchy. Top level .h files are located in the `include` directory and the corresponding .cpp are located in the `src` directory.

In figure 6.1 the `Cooker` directory hierarchy is shown. The `detector` directory was used to define low-level plugins for the various TREK/E36 detector elements. Whereas, the directories for `analysis`, `tracking`, etc., were used to define high-level plugins.

An example of a low-level plugin is the CsI calibration plugin that was used to cali-

brate the $K_{\mu 2}$ decay channel. Since the build environment for Cooker was generated by using `cmake`, this implied that all subsequent subdirectories needed `CMakeLists.txt` files. These `CMakeLists.txt` files were needed in order to create a localized build environment for either a given detector element or an analysis routine and thereby creating shared library objects.

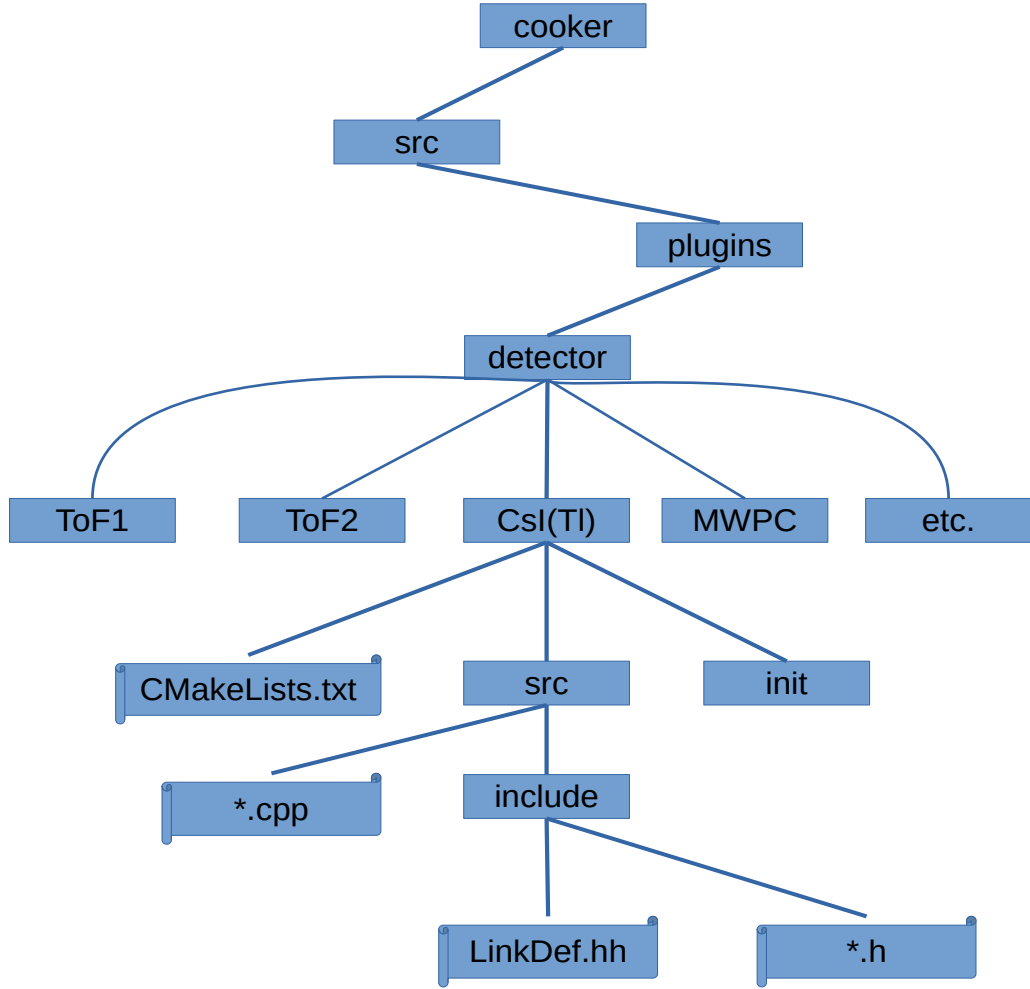


Figure 6.2. The low-level CsI(Tl) plugin hierarchical structure.

The `init` directory contained `.xml` and `.xsd` files which are written by the plugin developer and will be called at the beginning of a given plugin. This folder has the information that the developer would like to initialize. The `LinkDef.hh` file directs `rootcling` which classes should be added to the dictionary [122]. Inside the

the `LinkDef.hh`, the pragma statements were ordered by listing all specializations before any `classes` that needed them [122]. The `Det_CsI` was the main `class` for the CsI(Tl) plugin. Definitions of data members and functions used by the low-level calibration were defined in the `Det_CsI.h` file. The `Det_CsI.cpp` file included member functions for studying CsI timing and pulse height distribution. The pulse height distribution was used to calculate the gain factors for all the CsI(Tl) crystals. Routines for finding and identifying clusters were defined in the `findClusters` class. Gain factors from the calibration along with the `findClusters` functions were used in the `Cluster_CsI.cpp` functions, and cluster data variables were written to ROOT file for further analysis.

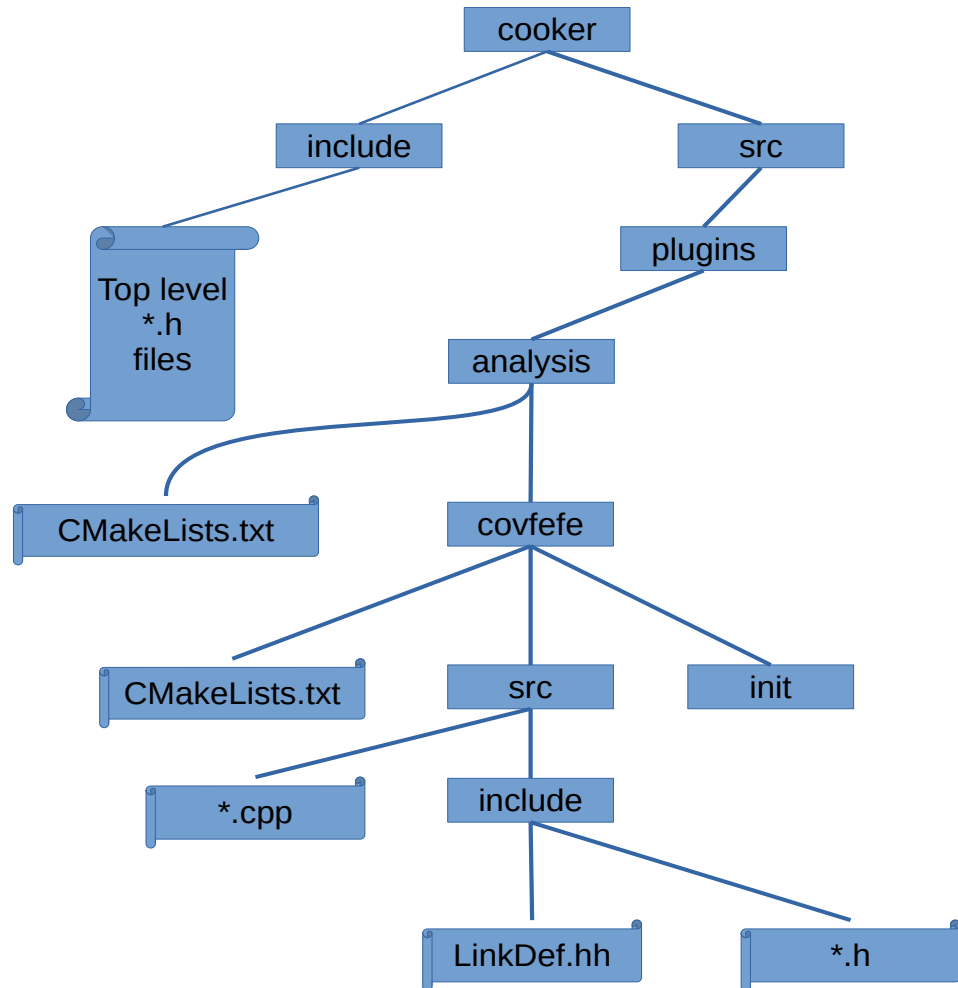


Figure 6.3. High-level analysis plugin for the CsI.

Evaluation of the clusters from the `Det_CsI` routines were analyzed by high-level analysis plugins. Figure 6.3 shows the directory structure of the CsI analysis plugin. Definitions of analysis data members and functions were defined in the `covfefe class`. The `evalClusters` was a utility method set-up for producing histograms and `TCanvas` under various analysis cuts defined in the `clusterAna.cpp` file. The cut conditions which will be discussed in more details later were broadly defined to fulfill the following conditions:

1. No cuts: All good gap events
2. $K_{\pi 2}$ momentum cut: $.190 \leq P_{K_{\pi 2}} \leq .215$ MeV
3. TOF1 multiplicity cut: required that least 3 TOF1 counters have fired

6.3 Calorimeter Calibration

PIN photodiodes (PIN diodes) were used to readout scintillation light from the CsI(Tl) crystals; because the strong toroidal fringing field under which the CsI barrel was operated rendered PMTs ineffective [97]. A detailed description of the CsI electronics can be found in Ref. [20].

Figure 6.4 shows system for each channel of the CsI detector. A low-noise preamplifier was mounted directly behind each crystal, the main amplifier with low-gain, high-gain and timing outputs, a constant-fraction discriminator(CFD), a common stop TDC (0.6 ns resolution), a time digitizer (TD) and a peak-sensitive ADC [20]. VF48 flash ADC (had a $10 \mu s$ time range) allowed waveform recording to be performed with 12-bit accuracy at a sampling rate of 25 MHz [19].

A special waveform fitting function was developed by Dr. Hiroshi Ito, in order to fit the output signals of the CsI(Tl) crystals in order to determine their respective energy and timing. Figure 6.5 (a) shows a typical CsI(Tl) waveform, plotted together

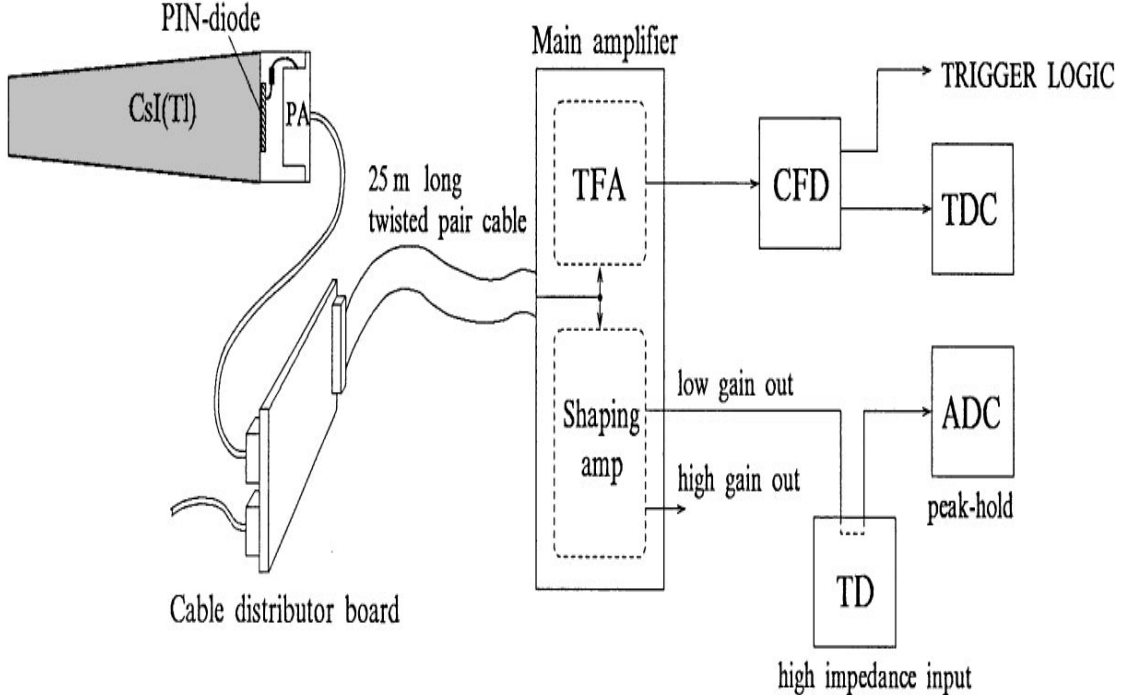


Figure 6.4. CsI detector electronics block diagram.

with the fit function, and (b) shows the the % residual. The following formula in equation 6.3.1 was employed for fitting [100],

$$f_1(t) = \frac{A}{1 - e^{-\frac{t-\tau_0}{\lambda}}} \cdot Freq\left(\frac{t - \tau_0 - d}{\mu}\right) \cdot \left[\frac{t - \tau_0}{\tau_1} e^{1 - \frac{t-\tau_0}{\tau_1}} + \epsilon \frac{t - \tau_0}{\tau_2} e^{1 - \frac{t-\tau_0}{\tau_2}} \right] + h_0, \quad (6.3.1)$$

where A is the amplitude of the waveform, λ, μ express the rising pulse, while the $\tau_{1,2}$ describe the decay region of the pulse and τ_0 describes the rise time. Detailed description of the fit function has been covered extensively in Ref. [100]. The frequency function, $Freq(x)$, from ROOT is defined as follows [122]

$$Freq(x) = \frac{1}{\sqrt{2}} \int_{\infty}^x e^{-t^2/2} dt. \quad (6.3.2)$$

Prominent K^+ decay modes are presented in table 6.1 below. The viability of being able to record two-body decays with the CsI detector enabled calibration with $K_{\mu 2}$ muons and a combined calibration procedure utilizing both tracking results and clusters in the CsI in order to perform calibration using $K_{\pi 2}$ pions. Calibration of the CsI crystals was performed by using dedicated $K_{\mu 2}$ calibration run data. Hit modules were identified as having good timing relative to the fiducial counter trigger timing. Since a given crystal has a length of 25 cm, the $K_{\mu 2}$ muon deposits all of its energy without creating a shower. For this reason, only single cluster events were evaluated for the calibration while noting that the initial kinetic energy of the $K_{\mu 2}$ muon is $T_\mu = 152.9 \text{ MeV}/c$ [8].

Table 6.1

Prominent K^+ decay modes

Decay	Branching ratio (%)	Energy of decay products (MeV)
$K^+ \rightarrow \mu^+ \nu_\mu (K_{\mu 2})$	0.635	$T_\mu = 152.4$
$K^+ \rightarrow \pi^+ \pi^0 \mu (K_{\pi 2})$	0.212	$T_{\pi^+} = 108.5$
$K^+ \rightarrow \pi^0 \mu^+ \nu_\mu (K_{\mu 3})$	0.0318	$T_{\pi^0} = 110.6$ $T_{\pi^0}^{max} = 118.9$

Pile-up events were observed in the form of a waveform having a double peak. Figure 6.6 shows a typical post-pile waveform. These pile-up events were important in classifying events as strictly $k_{\mu 2}$.

The fit function was used for the calibration of the CsI modules which utilized monoenergetic $K_{\mu 2}$ muons. The muons have an initial energy of $152.9 \text{ MeV}/c$, which they lose while traversing the CD system. The muons deposit all their energy into the crystals, creating a first pulse, a second pulse is produced as a delayed signal from the $\mu^+ \rightarrow e^+ \bar{\nu}_\mu \nu_e$ decay. As a consequence, a selection criterion needed to be established in order to properly select $K_{\mu 2}$ events. The criteria is as follows:

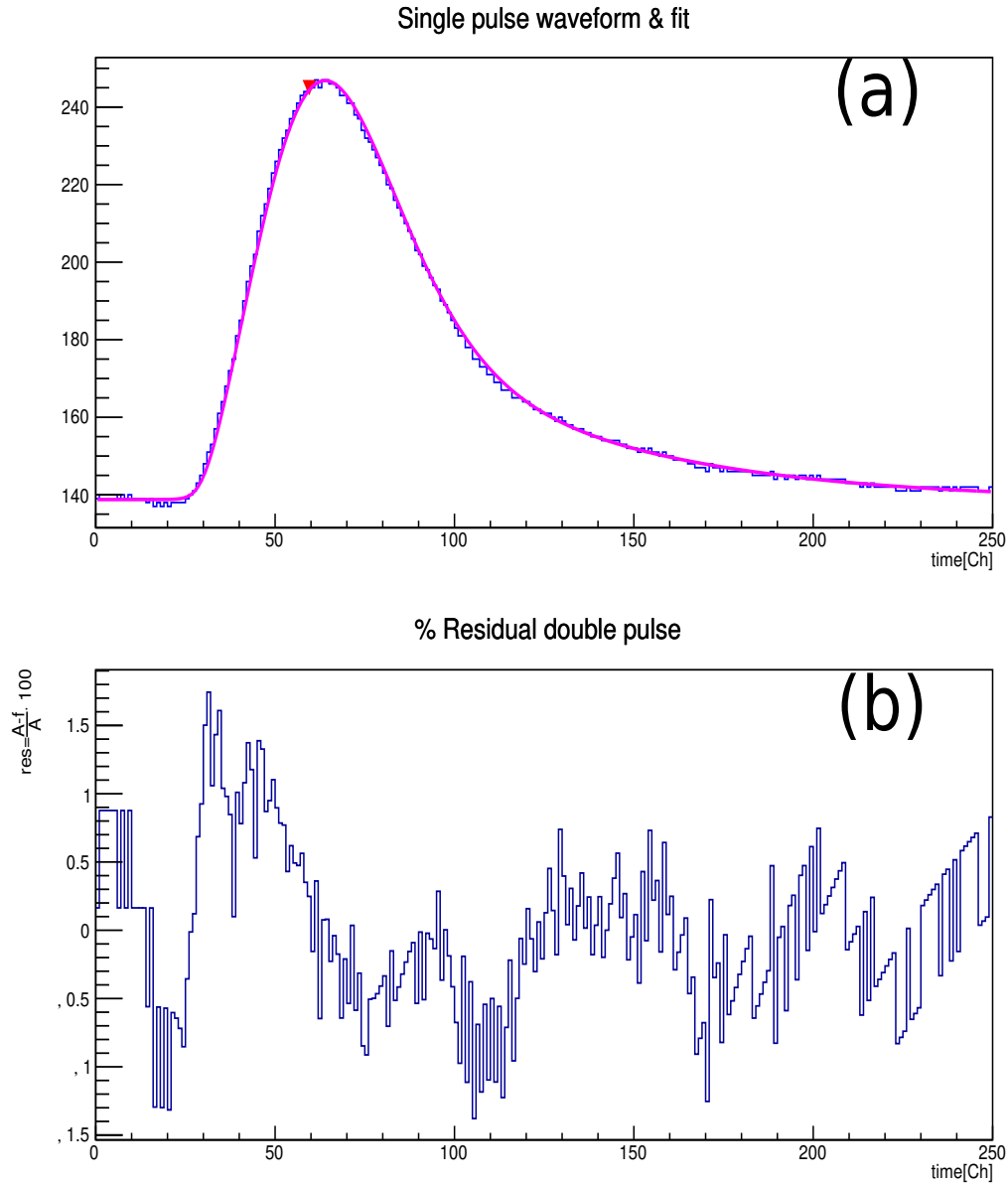


Figure 6.5. Typical VF48 single pulse waveform with fitting function. The figure at the bottom is the % residual.

1. only a single crystal registered a hit per event
2. peak time coincided with the K^+ decay time
3. waveform was analyzed using the double pulse fit function

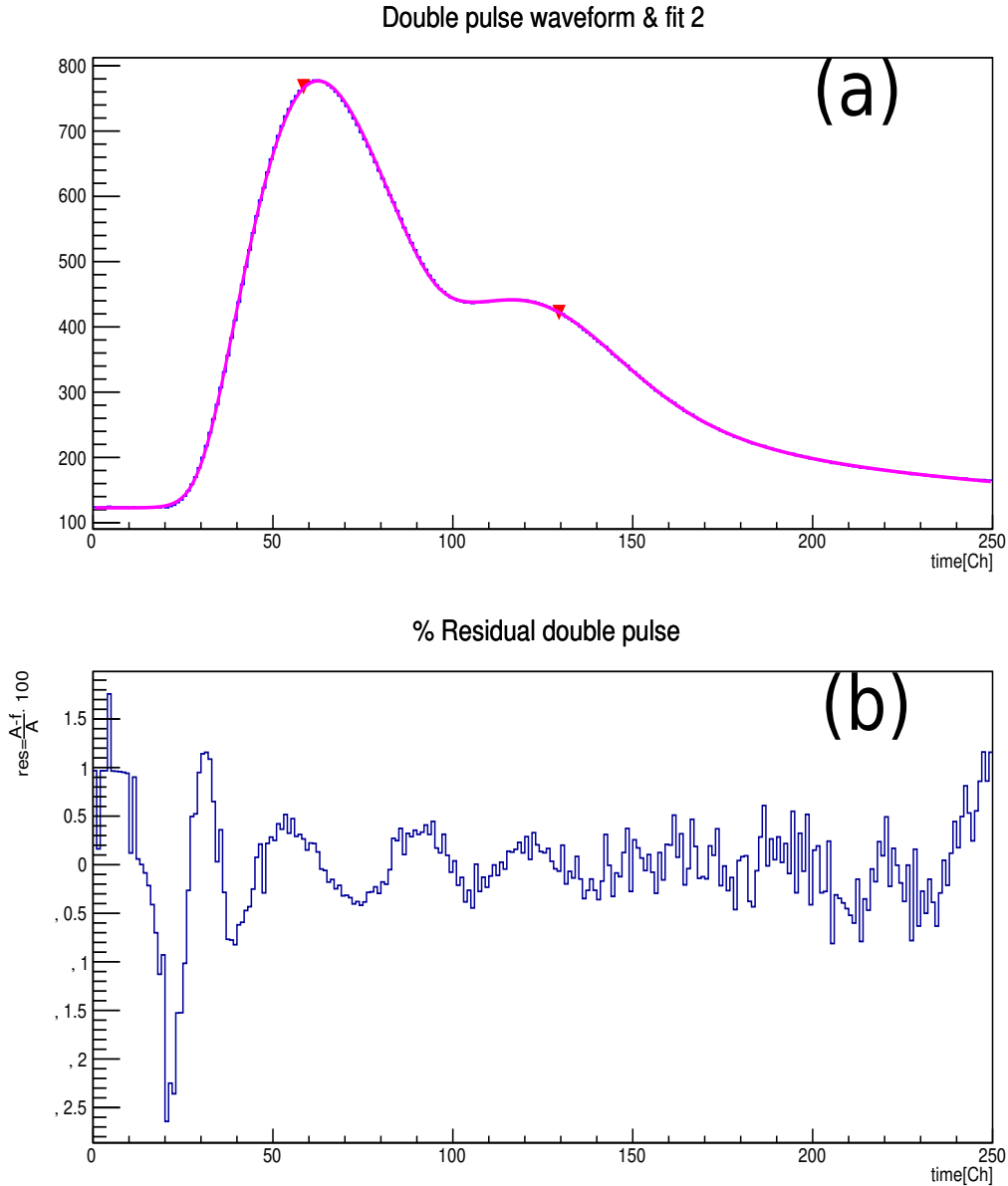


Figure 6.6. An example of a double pulse along with fitting function.

Below is a graph 6.7 showing the distribution of pulse heights. The blue histogram shows selection criteria 1 & 2, whereas the shaded histogram shows selection for all 3 criteria, which was used to calibrate the CsI crystals. The energy loss in the target system was calculated using the e36g4MC.

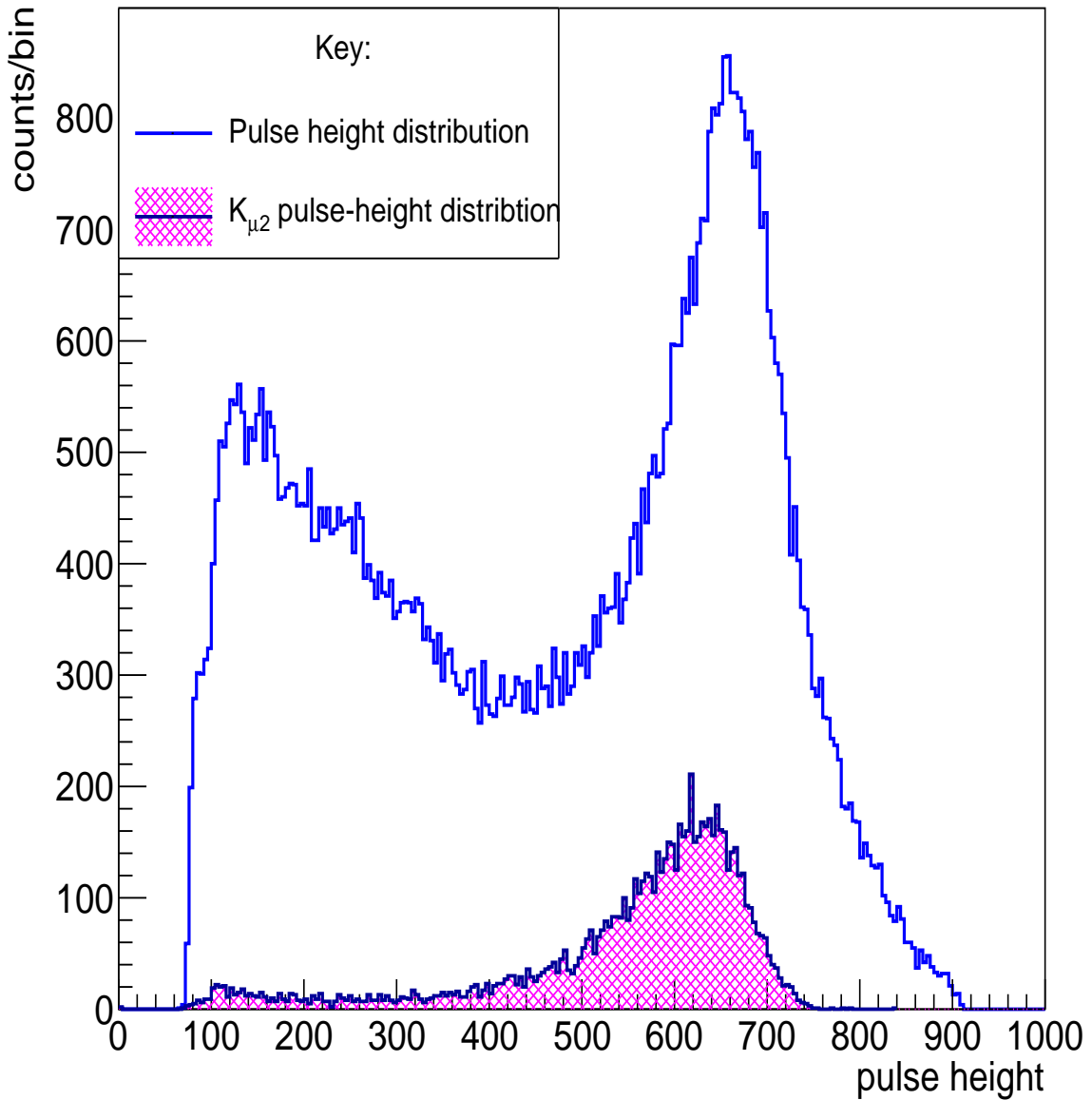


Figure 6.7. CsI(Tl) pulse height distribution

For this procedure the e36g4MC generator was used in the isotropic generation of the $K_{\mu 2}$ channel. The energy of the muons was recorded before entering the geometry of the CsI detector, and consequently the mean energy was established by taking the difference of the PDG value and the e36g4MC measurement. The e36g4MC measurement was used for all the CsI and crystals and the mean value was used to

calculate the incident muon energy in the CsI. Figure 6.8 shows the mean energy loss in the central detector (CD) system, with $\mu = 8.89$ MeV, and $\sigma = 2.97$ MeV.

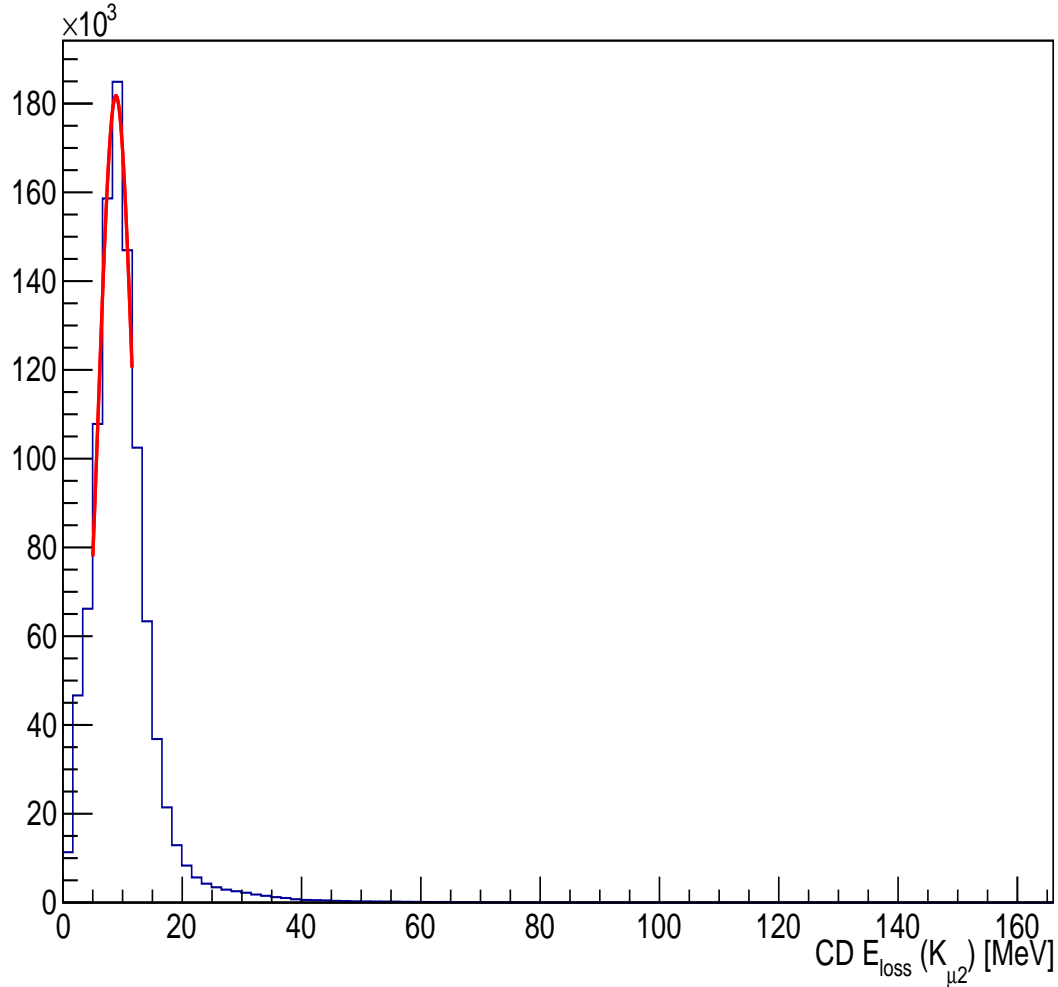


Figure 6.8. Energy loss in the central detector (CD) system as measured in the e36g4MC. The mean energy loss was calculated to be $\mu = 8.89$ MeV and $\sigma = 2.97$ MeV.

By using the measurement of the incident muon energy for all the CsI(Tl) crystals in the e36g4MC, calibration constants for all the CsI(Tl) crystal were obtained by making use of the following formula

$$C_i = \frac{dE_{CsI}}{(A - P)_i}, i = 1, \dots, 768. \quad (6.3.3)$$

Where A is the waveform amplitude and P is the baseline. In order for energy loss to applied, it was necessary to determine the energy loss due the muon traversing the CD system. Equation 6.3.4 below describes the CsI energy loss correction

$$T_\mu = dE_{CsI} + CDE_{loss}, \quad (6.3.4)$$

where T_μ is the muon monochromatic energy as described in table 6.1, dE_{CsI} is the incident energy of the muon for a give CsI(Tl) crystal, and CDE_{loss} is the energy loss due to a muon propagating through the CD system. The energy loss correction for all the CsI(Tl) was applied using the mean energy loss measured in figure 6.8 along with equation 6.3.4 above. The results for the $K_{\mu 2}$ energy loss are shown in figure 6.9 below, where the blue histogram shows the muon incident for the collective CsI(Tl) crystals and the cyan histogram shows the application fo the energy loss correction. There is good agreement between the T_μ value from table 6.1 and the mean value of the energy loss corrected $K_{\mu 2}$ muons in figure 6.9 below.

In addition to the $K_{\mu 2}$ decay channel, the $K_{\pi 2}$ decay was additionally used in the calibration of the CsI(Tl) by requiring a “*good gap event*”. A good gap event meant that the invariant mass of the π^0 was reconstructed in the CsI(Tl) barrel provided that a π^+ was detected using the MWPCs.

6.3.1 CsI Timing Study

A timing study of the CsI detector was performed in order to reduce the effects of accidental backgrounds. The trigger window for the VF48’s was between channels 60 – 65, and crystals with peak times that fell into this range formed candidate signals for waveform analysis. The peak time was defined as the time that coincided with the maximum amplitude of the waveform. Rudimentary analyses of peak times for given crystals were performed by recording the peak times of all crystals that had a

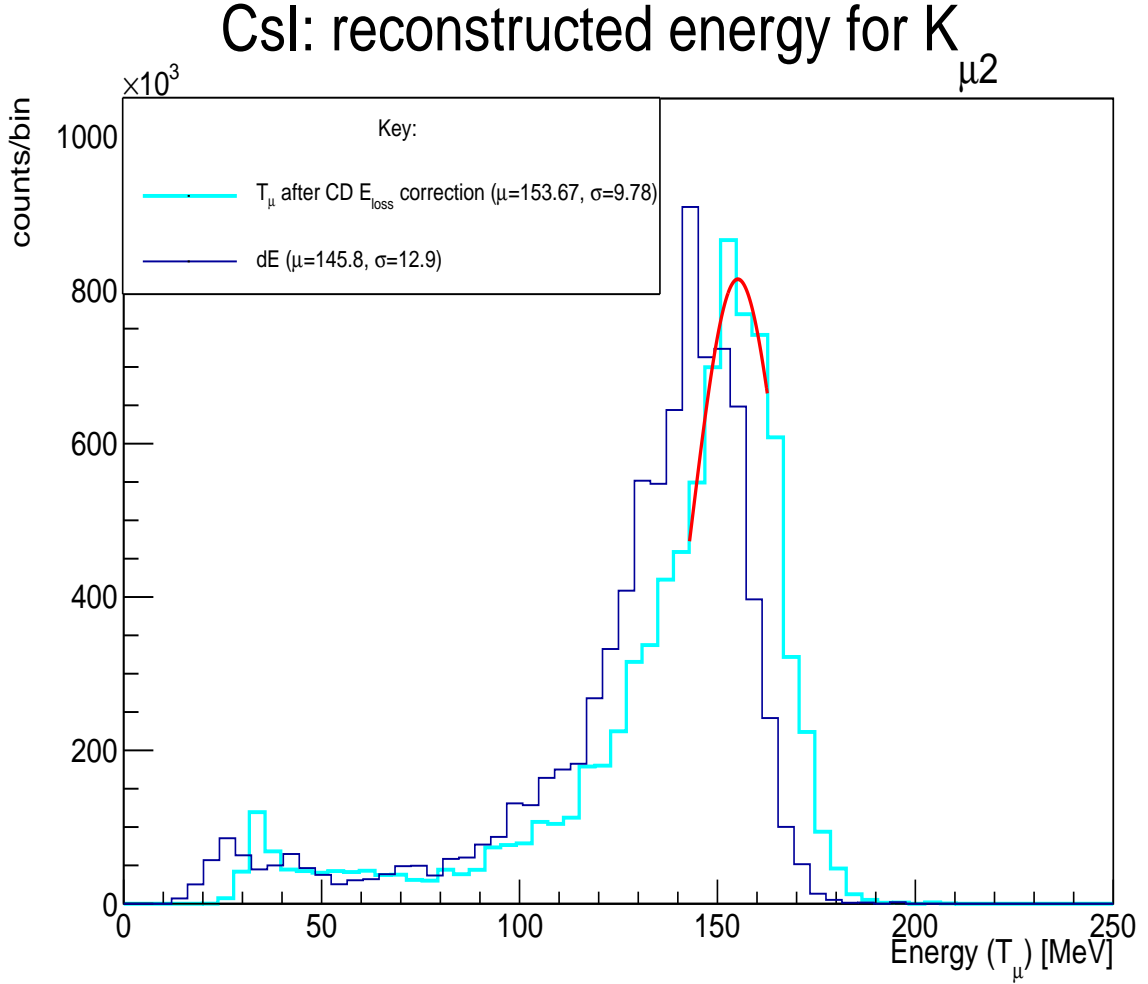


Figure 6.9. Incident energy dE of a $K_{\mu 2}$ muon (blue) upon striking a given CsI crystal. The cyan histogram T_μ is obtained after correcting for the energy lost by the muon as it traverses the central detector (CD) system.

signal above threshold in order to produce the histograms shown in figure 6.10. The need for the timing study is illustrated in figure 6.10 (b) below, where it is seen that accidental hits make it into the trigger window of channels 60 – 65 of production runs as opposed to calibration runs in figure 6.10 (a) where background hits were significantly suppressed. In figure 6.10 (a), the blue histogram is a CsI calibration run performed during the summer 2015 as part of the experimental engineering run and the red histogram is from the fall 2015 calibration run; figure 6.10 (b) are production runs from the fall of 2015.

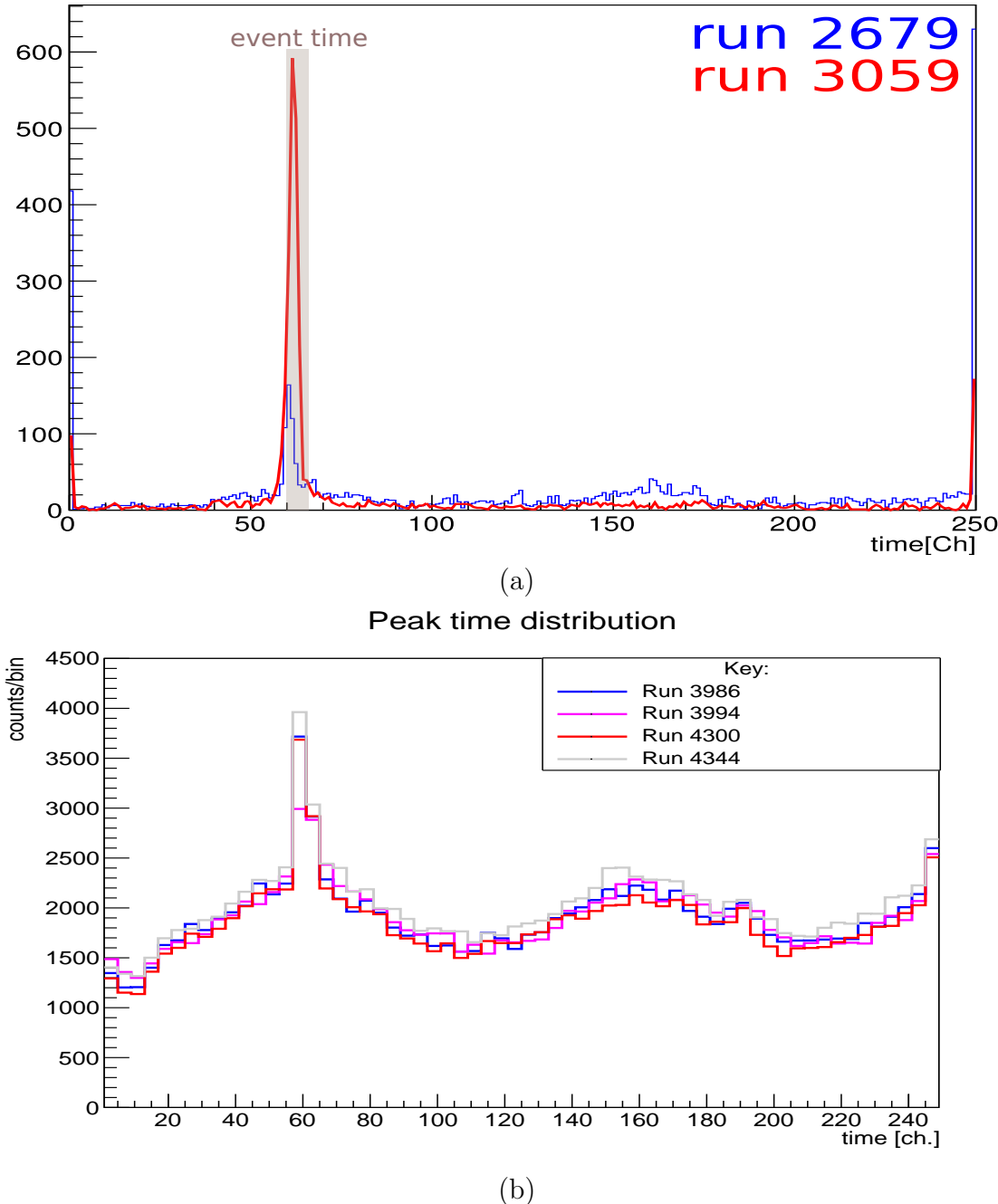


Figure 6.10. Peak time distribution for select calibration runs (a) and production runs (b).

The CsI electronics had three self-timed VF48 channels which served as the reference trigger time (T_{ref}) for candidate CsI signal events. CsI detector timing study

used information from the rise time τ_0 parameter of equation 6.3.1, peak time and constant fraction discriminator at half maximum (CFD50), in order to correct for the jitter and also to suppress accidentals. A schematic depicting the timing variables of interest is presented in figure 6.11 below.

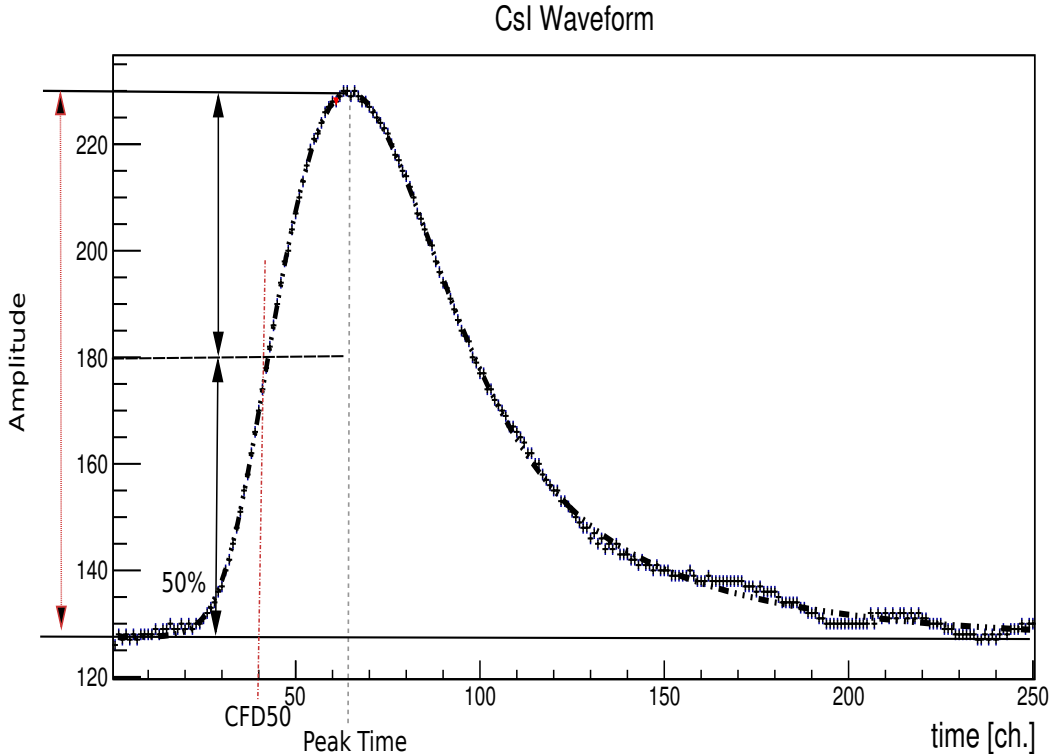


Figure 6.11. Typical VF48 waveform and fit. The figure has been annotated with the variables used to perform the timing study.

Evaluation of the CDF50 time involved taking a “constant fraction” of the pulse amplitude. This fraction was taken at 50% of the pulse amplitude and represents the inflection point. The CFD50 times for both signal and reference channels fluctuate around respective constant values, thereby providing the more stable timing study.

A study to observe the relationship between the energy, amplitude, and the CFD50 was performed by means of 2D histograms as shown in figure 6.13. Figure 6.13 (a) shows the 2D histogram of the CFD50 time for single crystal events plotted against the amplitude (energy). Amplitude walk is observed in this histogram. In figure 6.13

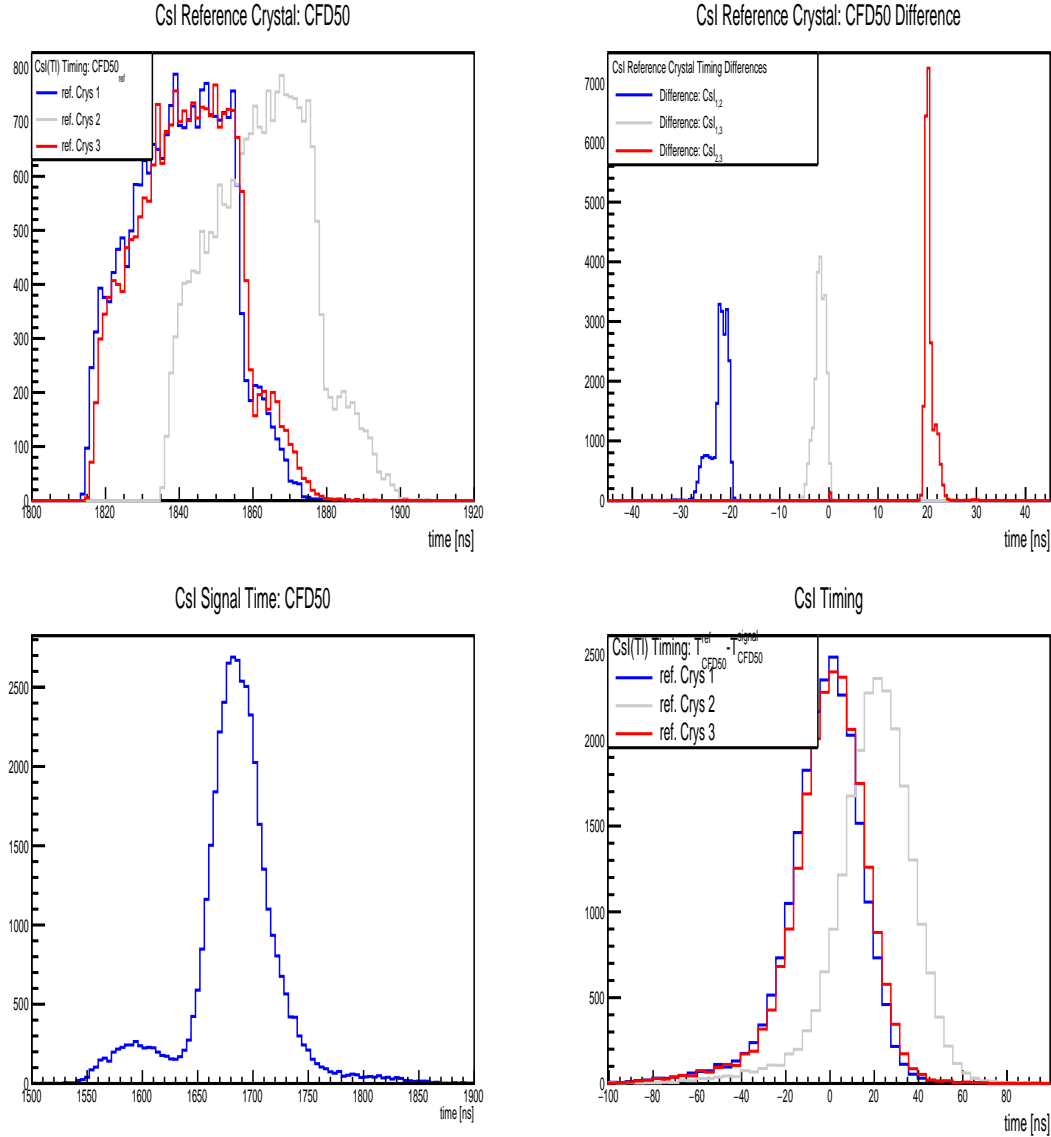


Figure 6.12. CsI timing study using the CFD50. The top row shows the CFD50 for the reference channels as well as the differences between them: $CsI_{ref1} - CsI_{ref2}$ (blue), $CsI_{ref1} - CsI_{ref3}$ (gray) and $CsI_{ref2} - CsI_{ref3}$ (red)). The bottom row shows the CFD50 times of the signal channels, as well as the determined CsI time, by taking the differences between the three reference channels and the signal channels.

(b) only candidate $K_{\mu 2}$ events were selected and the CsI time, which is the CFD50 time corrected by subtracting out the reference CFD50 time $T_{CFD50}^{ref} - T_{CFD50}^{sig}$, for these events was plotted again the energy. The CsI time together with the strict cut conditions used to select candidate $K_{\mu 2}$ events yield a clean sample with centralized

energy and time. From these results, it was concluded to use the corrected CFD50 time as the CsI timing information.

By using the blue histogram from the fourth set of histograms in figure 6.12 we were able to obtain the timing distribution by correcting for reference time T_{ref} . Figure 6.14 shows the μ^+ time distribution using the CFD50 method; and corrected for the reference time T_0 , $T_{CFD50}^{ref} - T_{CFD50}^{sig}$. The time resolution $\sigma = 14.1318$ ns, was obtained by fitting with a Gaussian.

6.3.2 Cluster Analysis: Overview

During the nascent developmental stages of the CsI cluster finding algorithm, a special **Cooker** graphical interface, **visco**, was used as common sense check for cluster finding performance. Cluster information, primarily the angles (θ and ϕ), number of clusters and energy, were printed to the screen. In conjunction with **visco**, an event viewer for the CsI detector was developed to visually assess the information printed to the screen by the cluster finder from one event to the next. By virtue of the information from the event viewer in figure 6.15 the goodness of the cluster finding algorithm was ascertained by the reconstruction of the π^0 invariant mass as well as the evaluation of the opening angle between the reconstructed π^0 and the tracked π^+ .

6.3.3 Cluster Analysis: $K_{\pi 2}$ Evaluation

Pulse height analysis was also performed for studying $K_{\pi 2}$ clusters in the CsI detector. Figure 6.16 shows the procedure for extracting cluster information from the Cooker plugin.

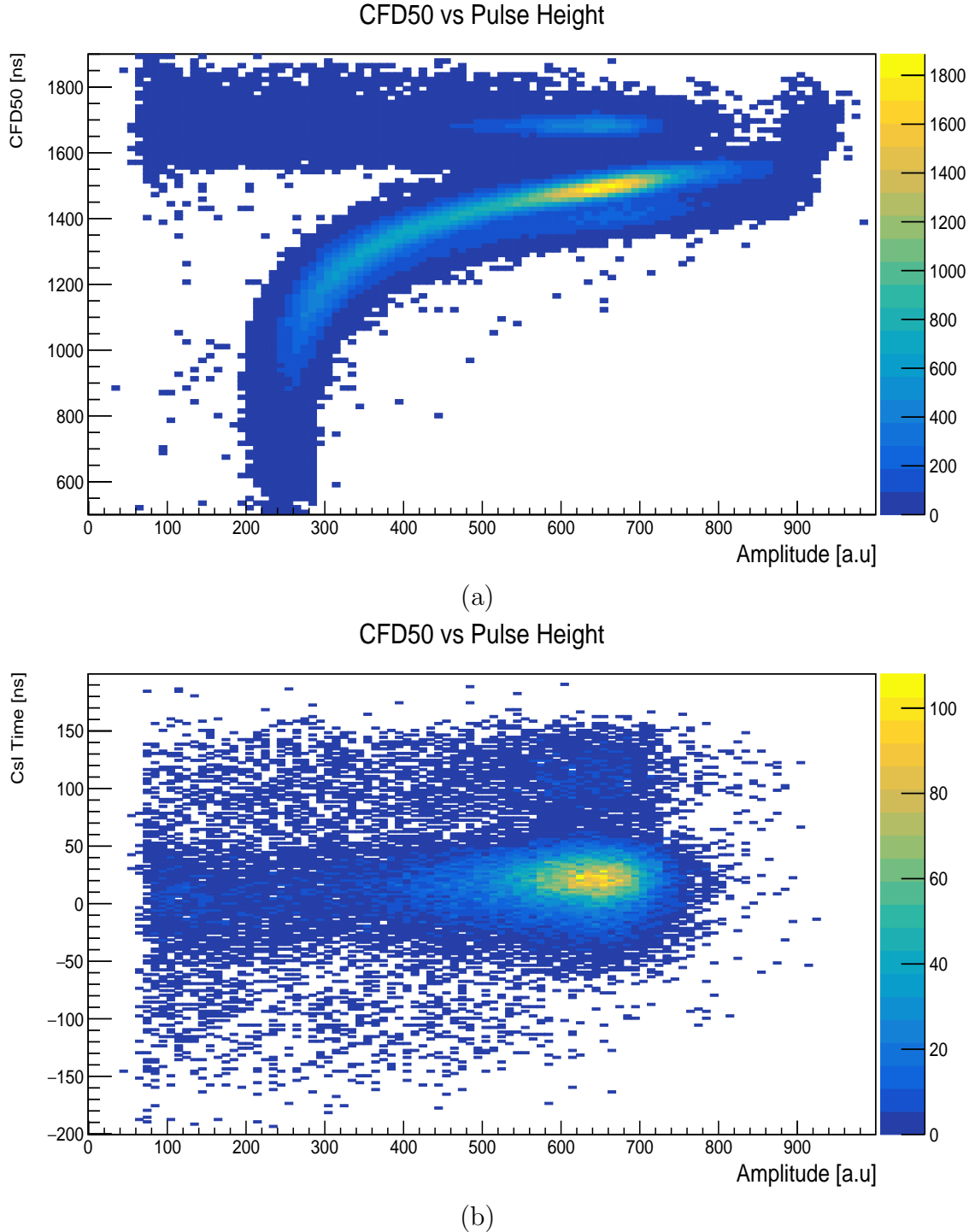


Figure 6.13. Two dimensional histograms depicting the relationship between the energy and the CFD50 time. In (a) we have single crystal events and a noticeable amplitude walk is observed, whilst in (b) we have select $K_{\mu 2}$ events and a more centralized amplitude is observed.

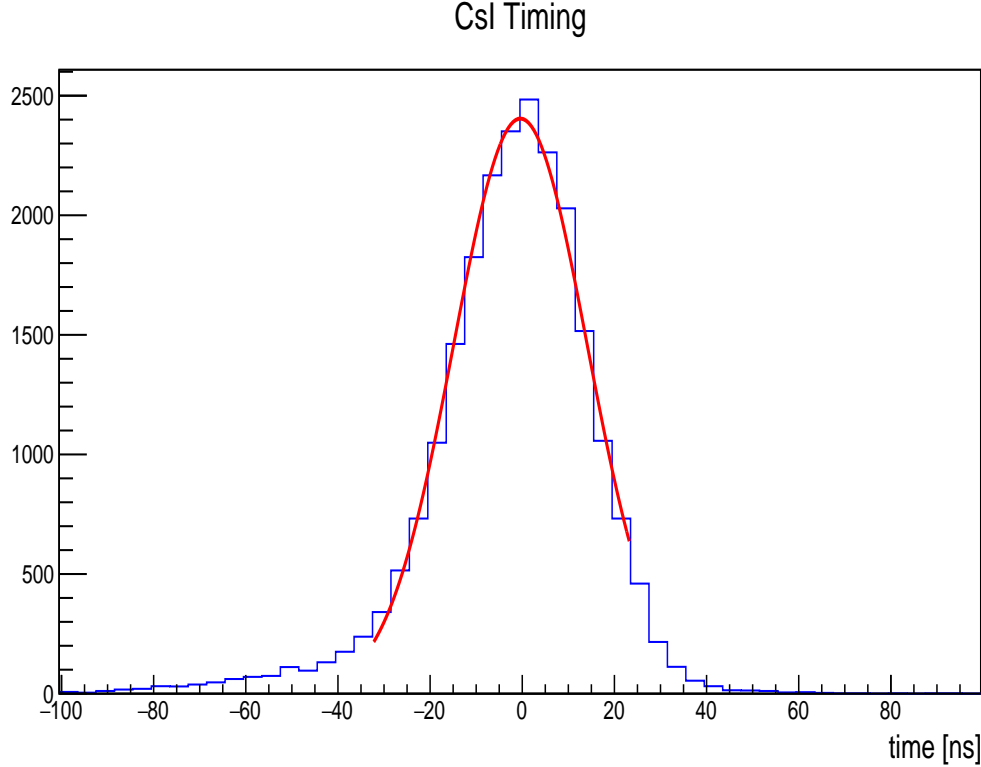


Figure 6.14. The μ^+ CFD50 time resolution corrected for the reference time T_0 . The time resolution was found to be $\sigma = 14.1318$ ns, by fitting a Gaussian.

Also shown in the figure 6.16, is that the same procedure was employed to study clusters in the e36g4MC, which was used to verify the MC simulation. The results from the $K_{\mu 2}$ calibration were applied to two cluster events in the CsI detector in order to reconstruct the invariant mass of the two clusters as well as their total energy. For a given cluster, the crystal with the highest energy was used as the central crystal and up to eight neighbouring crystals were considered to form a cluster. Since the CsI(Tl) was operated with high hardware threshold (≈ 20 MeV), only crystals with energies greater than 20 MeV participated for a given event. For this reason, single crystals were considered to be part of a cluster, namely a *single crystal cluster*. An energy-weighted centroid method was used to determine the location of a cluster, when clusters were formed from two or crystals $N_{crys} \geq 2$:

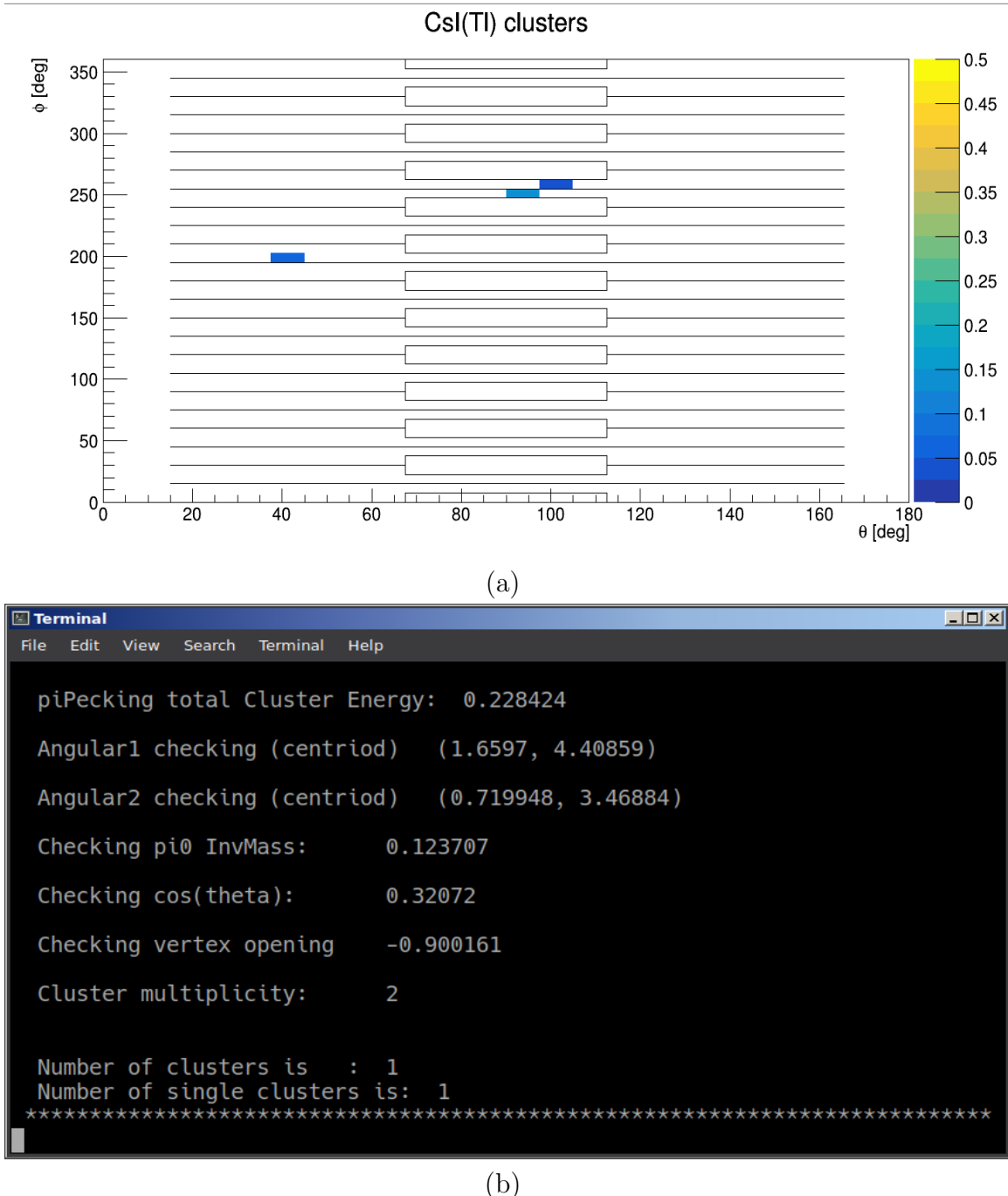


Figure 6.15. CsI event viewer (a) showing various cluster distributions displayed using visco and the screen print (b) with angles evaluated in radians.

$$\theta = \frac{\sum_i E_i \theta_i}{\sum_i E_i}$$

$$\phi = \frac{\sum_i E_i \phi_i}{\sum_i E_i},$$

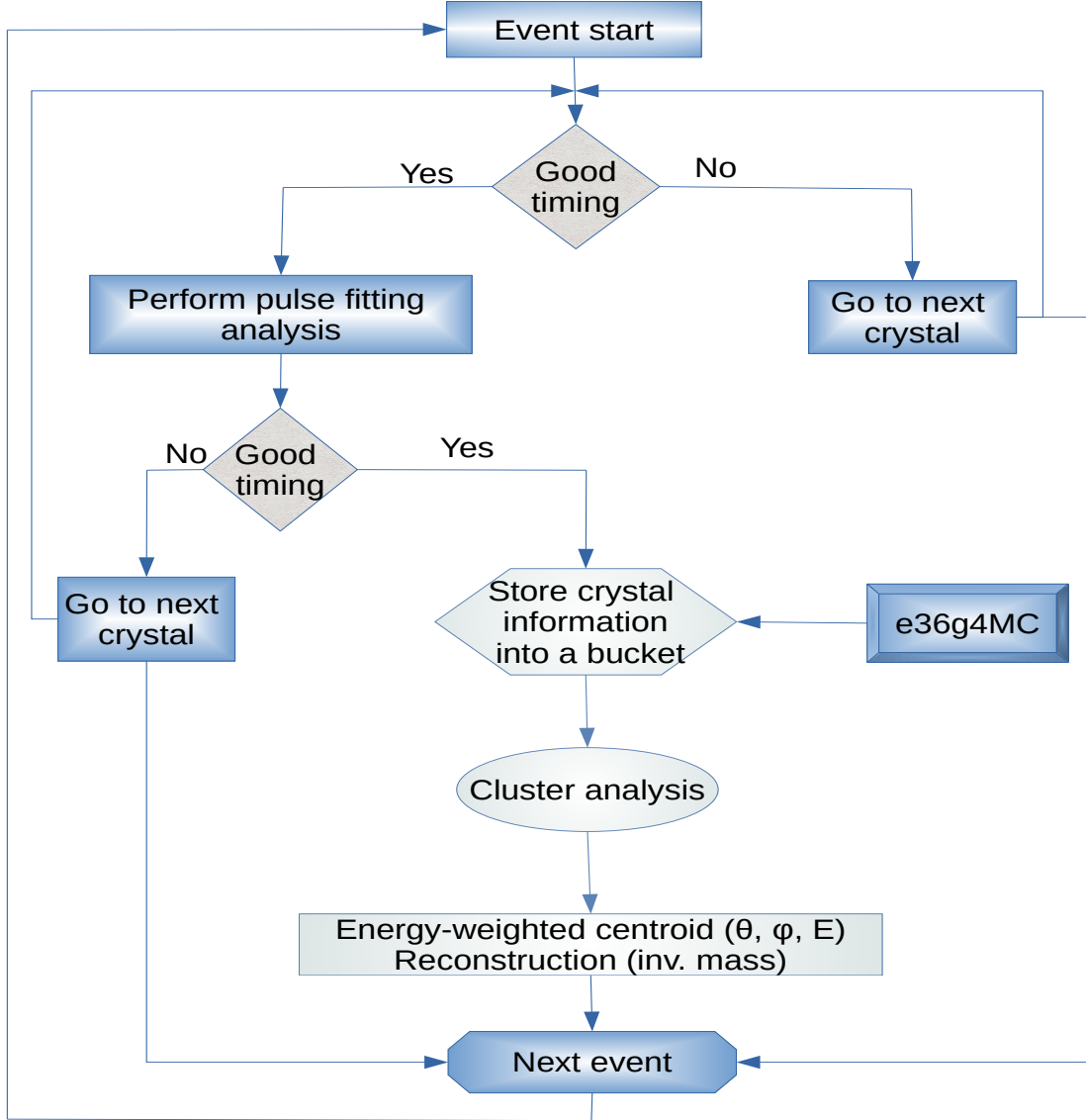


Figure 6.16. Flow charge showing the cluster algorithm for the CsI(Tl).

where E_i is the energy deposited in the i th crystal of the cluster and θ_i and ϕ_i are the polar and azimuthal angles of the i th crystal respectively. A K_{π^2} decay produces a neutral pion with a total energy $E_{\pi^0} = 245.6$ MeV and a positive pion with a momentum $p_{\pi^+} = 205$ MeV [8]. The π^+ formed a good gap event, and the neutral pion decayed into two photons $\pi^0 \rightarrow \gamma\gamma$ thereby forming two clusters in the CsI calorimeter. The criteria for pre-selecting π^0 from clusters in the calorimeter was as follows:

1. good gap event, i.e. a charged particle has a track that originated in the target and was tracked by the three MWPCs,
2. momentum cut centered around the $p(K_{\pi 2}) = 205$ MeV,
3. only two clusters were observed in the calorimeter.

A good gap required a charged particle to have a good track, meaning that a track has a vertex that originated in the target and was tracked by the three C-tracking elements. Upon momentum analyzing the tracks, a momentum cut was applied around the monochromatic momentum $p_{\pi^+} = 205$ MeV from the $K_{\pi 2}$ decay channel, shown in figure 6.17.

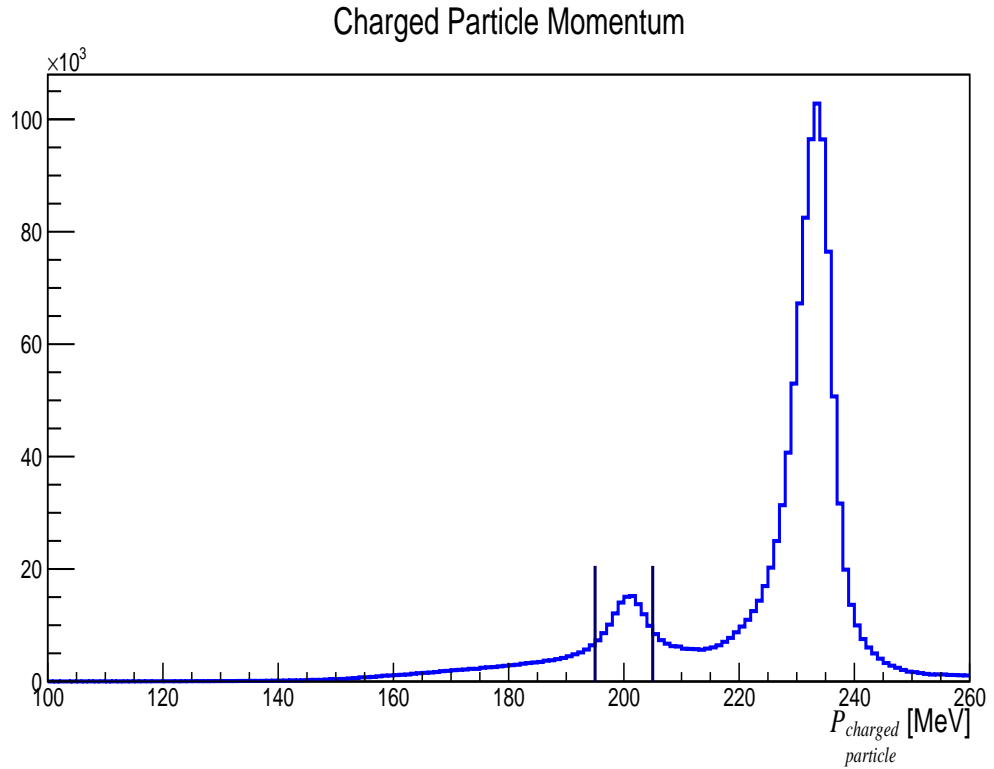


Figure 6.17. Momentum distribution for charged particle tracks, as analyzed by the toroidal spectrometer. The interval indicates a generous cut around the $K_{\pi 2}$ momentum.

Neutral pion events came from reconstructed two gamma clusters in the CsI detector. Since the kaon decayed at rest, this implies that the π^+ and π^0 are produced

back-to-back and therefore have an opening angle of $\theta_{\pi^+\pi^0} = 180^\circ$. Thus an additional cut was performed such that $\cos(\theta_{\pi^+\pi^0}) \leq -0.85$.

The e36g4MC the generator was used to run a solitary $K_{\pi 2}$ channel, which was much cleaner than the pre-selection of π^0 from the $K_{\pi 2}$ momentum in the data as shown in figure 6.18. The blue histograms are the data and the red histograms are from the e36g4MC simulation. The reconstructed π^0 invariant mass was observed to have a thinner peak compared to the data and a similar situation was also observed for the sum of the 2γ cluster energies. The angular agreement between data and e36g4MC is much better, although the e36g4MC does not fully reproduce the data. This disagreement could be due to beam profile characteristics contributing to accidental hits in the CsI, which the e36g4MC does not suffer from.

A strict cut requiring that on a single TOF1 counter registered a hit was further employed in order to reduce some of the accidental background. The low energy agreement between data and MC was much improved although there were still some lingering discrepancies at the high energy end as shown in figure 6.19. The observed disagreement at the high energy end could be due to several factors, such as accidental backgrounds from in-flight kaon decays and also from possible overestimation of the calibration coefficients. This overestimation might be due to the fact that muon only loses its energy by ionization, whereas the γ 's lose their energies by electromagnetic processes of bremsstrahlung, pair production and Compton scattering; implying that an additional gain factor < 1 might be needed to correct for this discrepancy. However, it is imperative to first suppress accidentals from in-flight kaon decays by imposing beam Čerenkov timing cuts in order to distinguish between prompt and stopped kaon decays.

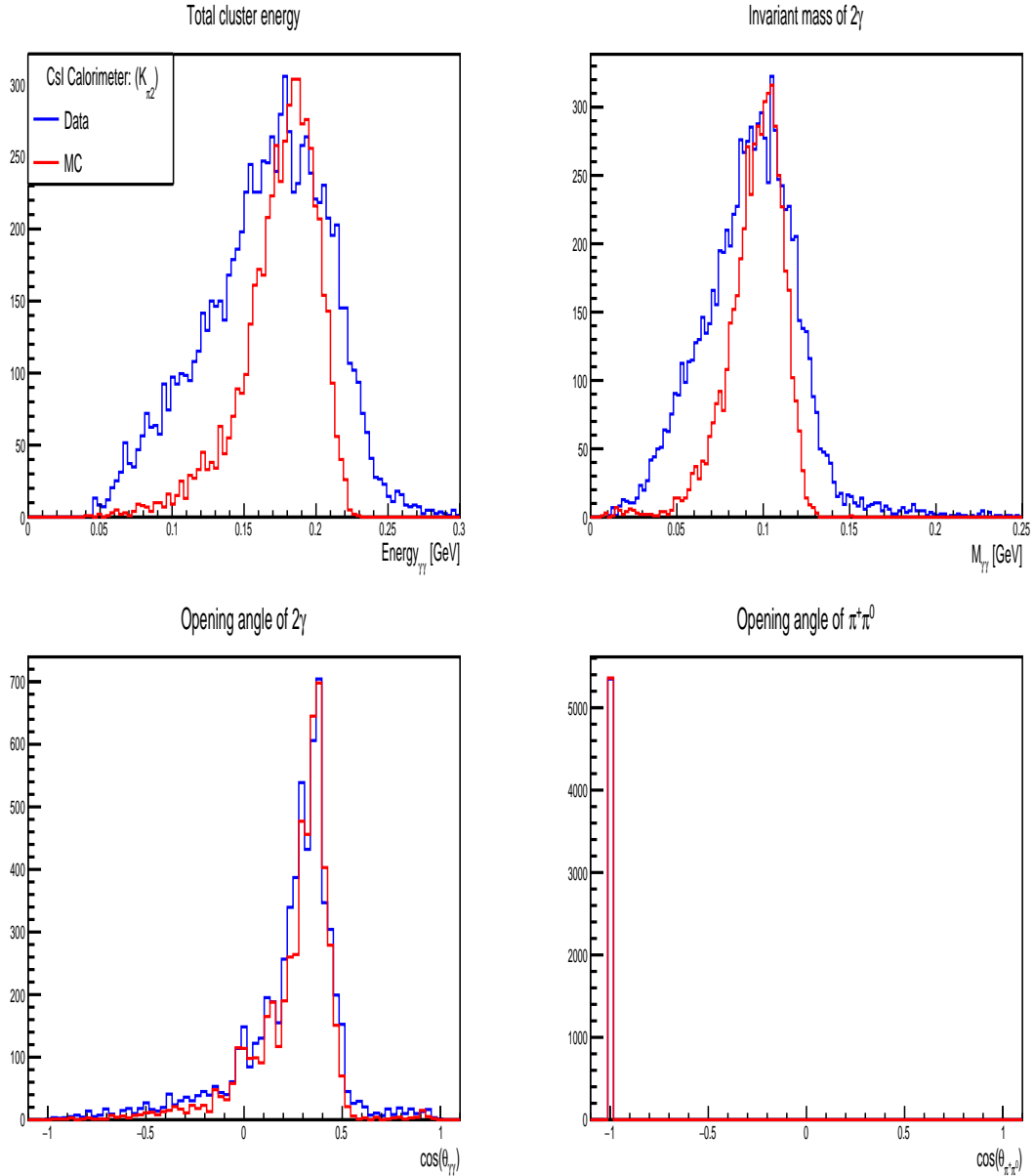


Figure 6.18. Plots of total energy, invariant mass of 2γ clusters, opening angle of 2γ 's, $\cos(\theta_{\gamma\gamma})$, and opening angle of $\pi^+\pi^0$ $\cos(\theta_{\pi^+\pi^0}) \leq -.99$; where the blue histograms are the data and the red histograms are from the e36g4MC.

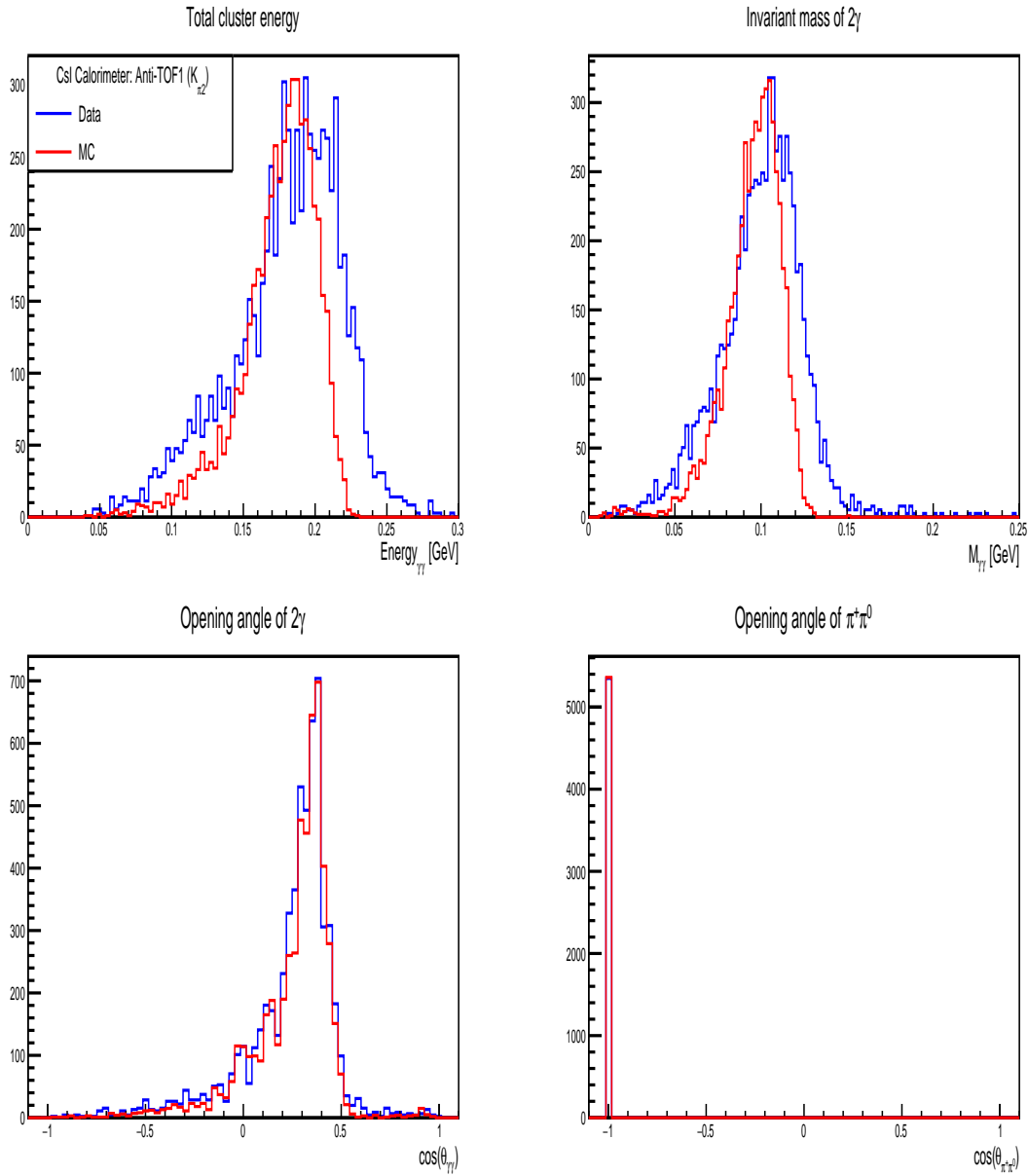


Figure 6.19. Plots of total energy, invariant mass of 2γ clusters, opening angle of 2γ 's, $\cos(\theta_{\gamma\gamma})$, and opening angle of $\pi^+\pi^0$ $\cos(\theta_{\pi^+\pi^0}) \leq -.99$. Better agreement between data and simulation was achieved by requiring that only a single TOF1 has registered a hit per event.

CHAPTER 7

RESULTS AND CONCLUSION

The TREK/E36 A' search was performed in the muonic kaon decay channel $K^+ \rightarrow \mu^+ \nu A'$, followed by the prompt $A' \rightarrow e^+ e^-$ decay. The trigger condition for the A' required a charged particle in the gap and 3 TOF1 counters that registered a hit. Ideally, one of the three TOF1 counters corresponds a tracked μ^+ while the other two register e^+ and e^- . The e^+e^- pair would then go on to form two clusters in CsI calorimeter, which can be used to produce an invariant mass spectrum M_{ee} . A peak search over a continuous background is needed to determine if an A' signal is present. PID systems are needed to suppress sources of reducible background, such as π^+ from $K_{\pi 2}$ decays and positrons, when these particle are detected in the gap. A dedicated generator was employed to determine the A' search window as a function of assumed masses $m_{A'}$. The generator was also used to calculate the number of stopped kaon N_K , a value that used in the extraction of the A' branching ratio $\mathcal{Br}(A')$ upper limit at 95% CL.

The author performed the calculations for the total number of stopped kaons N_K as well as acceptance fractions of $K_{\mu 2}$ muons and the A' masses $m_{A'}$ between 20-100 MeV. The e36g4MC toolkit was employed for calculating the acceptances and also for determining the width of the A' search window as a function of $m_{A'}$. Furthermore, the upper limit extraction of $\mathcal{Br}(A')$ were carried out by the author.

7.1 Acceptance and N_K Determination

The number of stopped K^+ in the fiducial region of the active target was computed as follows

$$\begin{aligned} N_K &= \frac{N_{\mu 2}}{\mathcal{B}r(\mu 2)PS_{\mu 2}A_{\mu 2}LT_{\mu 2}} \\ &= 2.81 \times 10^9 \end{aligned} \quad (7.1.1)$$

where $N_{\mu 2}$ is the number of tracked data candidates satisfying the $K_{\mu 2}$ decay momentum, $A_{\mu 2}$ is the acceptance of the $K_{\mu 2}$ muons evaluated with the MC simulations, $\mathcal{B}r(\mu 2)$ is the nominal branching ratio of the $K_{\mu 2}$ decay mode and $PS_{\mu 2} = 49$ and $LT_{\mu 2} = 1$ are the muon prescale factor and lifetime fraction respectively. Numerical values of the data candidates and simulation acceptance are summarized in table 7.1.

Table 7.1

Data candidates and acceptance

Data candidates	$N_{\mu 2} = 1.25 \cdot 10^9$
MC acceptance:	
$K_{\mu 2}$ decay	$A_{\mu 2} = 3.48012\%$

A custom K^+ decay generator, developed by Dr. Tongtong Cao as a standalone package, was employed to assist in studying the acceptances of the A' signal scan. The generator is instrumental because Geant4 does not contain kaon decay modes for the A' . This problem is solved by the generator which uses ROOT classes to calculate 18 kaon decay channels, including those with A' 's. The author modified the generator and adjoined it to the e36g4MC toolkit as library. The K^+ and π^0 decay modes are shown in tables 7.2 and 7.3, respectively.

Table 7.2

The K^+ decay channels and the corresponding branching ratios

Label	Branch	Ratio
0	$K^+ \rightarrow e^+ \nu$	1.582×10^{-5}
1	$K^+ \rightarrow \mu^+ \nu$	6.355×10^{-1}
2	$K^+ \rightarrow e^+ \pi^0 \nu$	5.07×10^{-2}
3	$K^+ \rightarrow \mu^+ \pi^0 \nu$	3.352×10^{-2}
4	$K^+ \rightarrow e^+ \pi^0 \pi^0 \nu$	2.55×10^{-5}
5	$K^+ \rightarrow \pi^+ \pi^- e^+ \nu$	4.247×10^{-5}
6	$K^+ \rightarrow \pi^+ \pi^- \mu^+ \nu$	1.4×10^{-5}
7	$K^+ \rightarrow \pi^+ \pi^0$	2.067×10^{-1}
8	$K^+ \rightarrow \pi^+ \pi^0 \pi^0$	1.760×10^{-2}
9	$K^+ \rightarrow \pi^+ \pi^+ \pi^-$	5.583×10^{-2}
10	$K^+ \rightarrow \mu^+ \nu \gamma$	6.2×10^{-3}
11	$K^+ \rightarrow e^+ \nu \gamma$	9.4×10^{-6}
12	$K^+ \rightarrow \mu^+ \pi^0 \nu \gamma$	1.25×10^{-5}
13	$K^+ \rightarrow \pi^+ \pi^+ \pi^- \gamma$	1.04×10^{-4}
14	$K^+ \rightarrow \mu^+ \nu A'$	$\epsilon^2 \times \text{ratio of channel 16}$
15	$K^+ \rightarrow \pi^+ A'$	$\epsilon^2 \times \text{ratio of channel 17}$
16	$K^+ \rightarrow \mu^+ e^+ e^- \nu$	2.5×10^{-5}
17	$K^+ \rightarrow \pi^+ e^+ e^-$	3×10^{-7}

Table 7.3

The π^0 decay channels and corresponding branching ratios

Label	Branch	Ratio
0	$\pi^0 \rightarrow \gamma \gamma$	9.8823×10^{-1}
1	$\pi^0 \rightarrow e^+ e^- \gamma$	1.174×10^{-2}
2	$\pi^0 \rightarrow \gamma A'$	$\epsilon^2 \times \text{ratio of channel 2}$

Using the generator, a scan for the A' signal was performed in the mass range of $20 \text{ MeV}/c^2 \leq m_{A'} \leq 110 \text{ MeV}/c^2$. Lower A' masses were disfavored because the CsI calorimeter was operated under high hardware threshold settings during the data-taking. Equally, higher A' masses are kinematically suppressed in $K^+ \rightarrow \mu^+ \nu A'$ decay, and the yields of muons tracked by the C2, C3 and C4 detectors in the e36g4MC were further suppressed by the spectrometer acceptance. This phenomena can be observed from the e36g4MC acceptance distribution as a function of assumed $m_{A'}$.

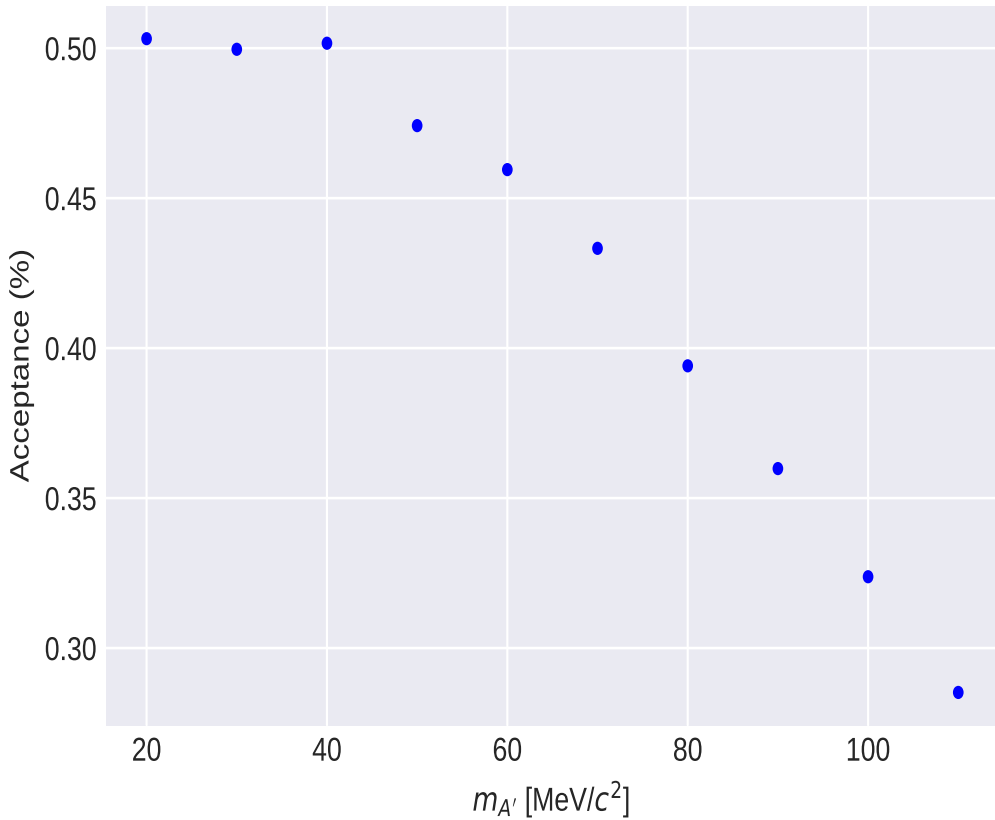


Figure 7.1. The acceptance (%) for assumed A' masses, demonstrating the low and high $m_{A'}$ yield suppression.

The search window of the A' as a function of $m_{A'}$ was determined by fitting a Gaussian around the mean values of MC reconstructed masses. The mass step of the scan was defined by a $1.0\sigma_m(m_{A'})$ cut around the reconstructed $m_{A'}$ value, which

increased with increasing assumed $m_{A'}$ as seen figure 7.2. The A' search window increased linearly with increasing mass.

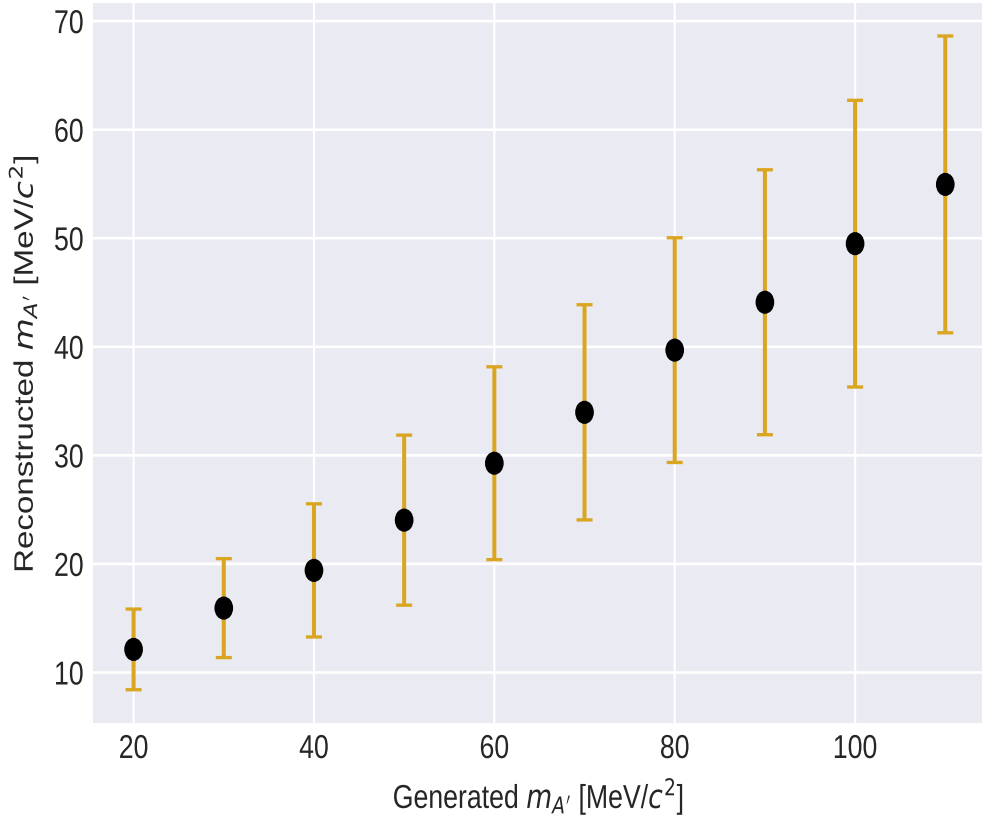


Figure 7.2. Mean values of e36g4MC reconstructed $m_{A'}$ as a function of assumed A' masses. The golden bands represent a $1\sigma_m(m_{A'})$ cut around the mean $m_{A'}$ values.

7.2 Light Neutral Boson A' Signal Search

The A' signal search required a TOF1 multiplicity of 3 or greater, implying that three charged particles passed through the TOF1 counters. An additional “*good gap*” condition was levied on one of the three charged particles that traversed through the TOF1 counters. A good gap event is defined as a charged particle that registered hits in the tracking detectors C2, C3 and C4, and has an extended vertex from tracking

that lies within the fiducial volume of the target. Figure 7.3 (a) shows the TOF1 multiplicity distribution under the following conditions: good gap, K_{π_2} momentum cut and $\text{TOF1 multiplicity} \geq 2$ cut. The corresponding momentum distributions are shown in figure 7.3 (b).

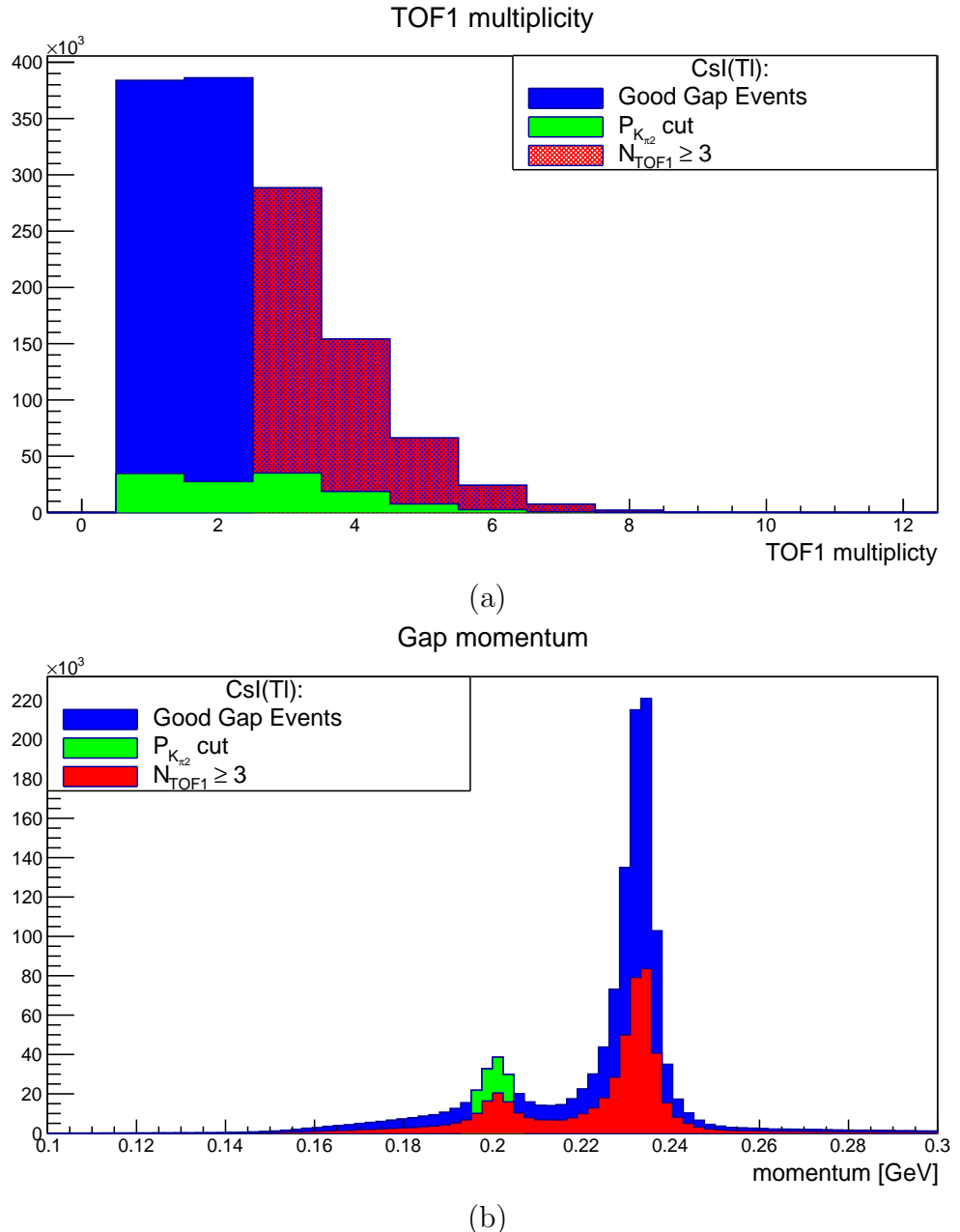


Figure 7.3. TOF1 multiplicity (a) indicating the number of counters that registered a hit per event. Charged particle momentum distribution (b) under three cut conditions: good gap (blue); K_{π_2} momentum region (green) and TOF1 multiplicity (red).

The yields of reconstructed invariant mass spectra from two cluster events in the CsI were conducted under the following cut conditions,

1. good gap events (blue)
2. $K_{\pi 2}$ momentum cut (green)
3. TOF1 multiplicity cut of ≥ 3 (red)

and are shown in figure 7.4. The blue histogram corresponds to all the events that have two clusters in the CsI and a charged particle in the gap. In the $K_{\pi 2}$ momentum cut the π^0 invariant mass was reconstructed from 2γ clusters and a m_{π^0} peak was observed. Candidate events for the A' search, satisfying the 3 TOF1 multiplicity condition, in the reconstructed invariant mass spectra M_{ee} are shown in the red histogram in figure 7.4.

Since a good gap event was required for the A' analysis, the red histogram of figure 7.3 (b) provides a scope into the momentum dependent background contributions of charged particles detected in the gap. Notice that even under a three TOF1 multiplicity cut, $K_{\mu 2}$ muons still formed the dominant background component. It can therefore be concluded that CsI clusters corresponding to charged particle tracks satisfying the $K_{\mu 2}$ momentum were a result of accidental hits in the calorimeter and thereby contributed to a reducible background in the invariant M_{ee} mass spectrum. In order to reduce background contributions from $K_{\mu 2}$ muons, the e36g4MC was used to study the endpoint momenta of various assumed A' masses and recording the muon momentum at the C4 detector.

A mean energy loss correction was applied to the charged particle momentum evaluated at C4. Figure 7.5 shows the energy corrected muon momenta under assumed

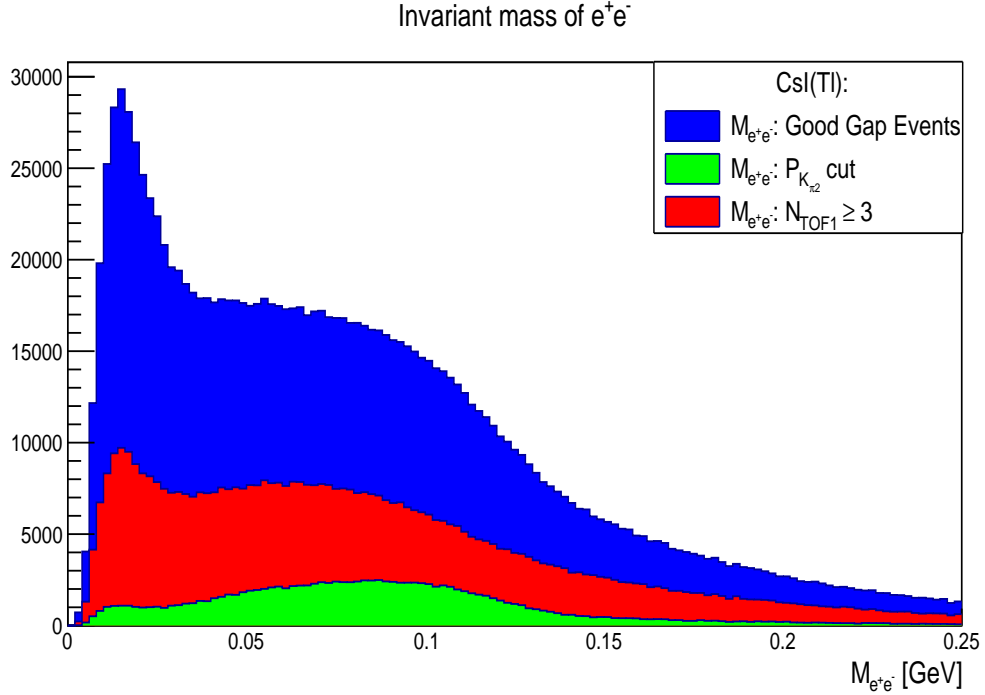


Figure 7.4. Invariant mass m_{ee} distributions under three cut conditions: good gap (blue); $K_{\pi 2}$ momentum region (green) and extra TOF1 (red).

A' masses, overlaid with an energy corrected momentum plot from $K_{\mu 2}$ and $K_{\pi 2}$ decays. The momenta were scaled to the $K_{\mu 2}$ yields for a better comparison of the overlap from $K_{\mu 2}$, as well as establishing a reasonable cut condition.

A momentum cut at 230 MeV was applied to the tracked particle in order to reduce some of the background, which can be seen as a solid light red line in figure 7.5. Since there is significant overlap between the $K_{\pi 2}$ pion and the muon from the scanned A' masses, there are no momentum cuts that can reduce the $K_{\pi 2}$ contribution and for this analysis, the $K_{\pi 2}$'s formed an irreducible background component to the A' search. A thorough PID analysis can get rid of the $K_{\pi 2}$ background and in turn increase the sensitivity of our probe. All numerical quantities are summarized in table 7.4.

Charged Particle Momentum

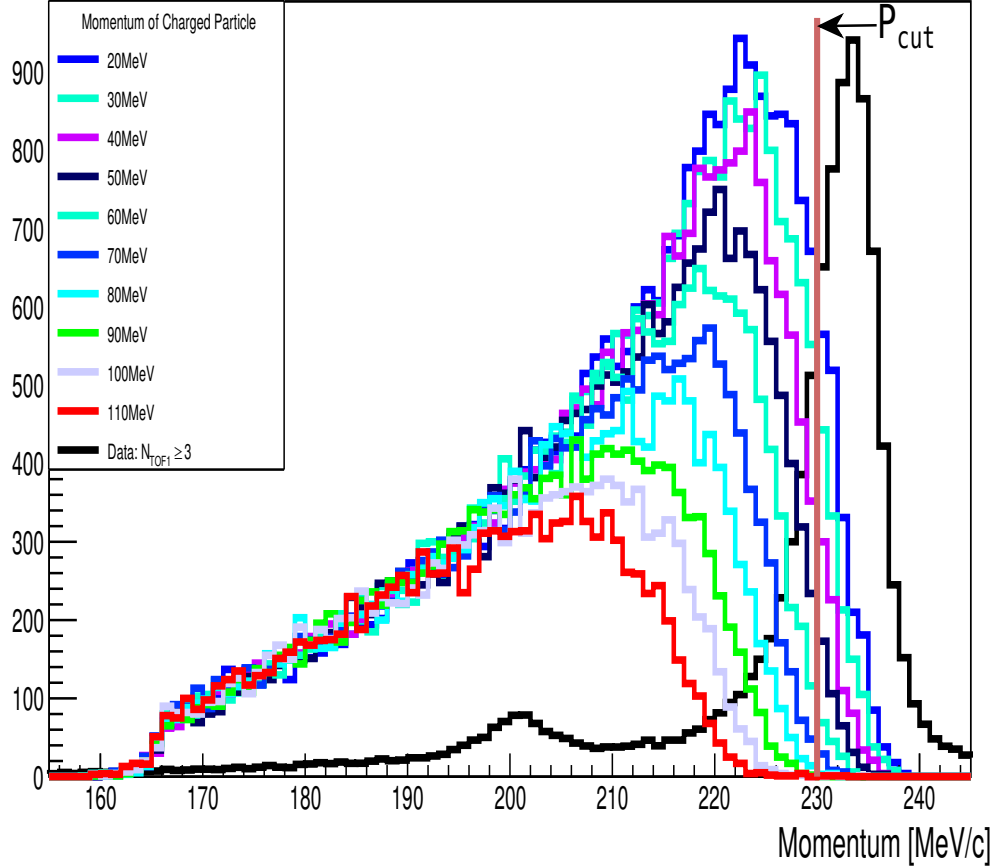


Figure 7.5. The e36g4MC endpoint momentum distributions for assumed A' masses and the two prominent K^+ decays. The momentum spectrum of the data was used for the condition that at least 3 TOF1 counters had fired.

Upper limits at 95% CL on the branching ratio of $B(K^+ \rightarrow \mu\nu A')$ for each A' mass value, corresponding to a 2σ limit of not observing the A' , under the assumption that $Br(A' \rightarrow e^+e^-) = 1$ were computed using the relation

$$Br(K^+ \rightarrow \mu\nu A') < \frac{2\sqrt{N_{\mu\nu ee}}}{N_K A_{A'} \cdot LT} \quad (7.2.1)$$

where $N_{\mu\nu ee}$ is the integrated number of events in a given A' search window, $A_{A'}$ is acceptance ratio of the A' with a given mass, determined from the e36g4MC. Figure 7.6 shows the upper limit under the 3 TOF1 counter multiplicity. They are

Table 7.4

Acceptances and number of data events

Events with 3 charged particles					
Generated $m_{A'}$	Reconstructed $m_{A'}$	Cut Window $\delta_{A'}$	Acceptance A'	Number of Background	Upper Limit
20	13.4519	3.87869	0.0037473	3.20×10^4	3.16×10^{-5}
30	16.2201	5.23556	0.00424818	4.21×10^4	3.65×10^{-5}
40	20.0441	5.64782	0.00462635	5.40×10^4	4.12×10^{-5}
50	24.8995	6.59778	0.00443463	6.32×10^4	4.72×10^{-5}
60	29.4384	8.24074	0.00438983	6.68×10^4	5.00×10^{-5}
70	34.3622	9.47883	0.0040863	7.28×10^4	5.54×10^{-5}
80	39.8596	10.1687	0.00378748	7.59×10^4	6.22×10^{-5}
90	44.2728	11.5294	0.00344984	9.09×10^4	7.45×10^{-5}
100	50.0189	12.6876	0.00311341	1.00×10^5	8.68×10^{-5}
110	55.3015	13.2774	0.00274744	1.05×10^5	1.01×10^{-4}

$\mathcal{O}(10^{-5})$ and show strong dependence on the assumed A' mass primarily because the acceptance of A' decreases with increasing $m_{A'}$.

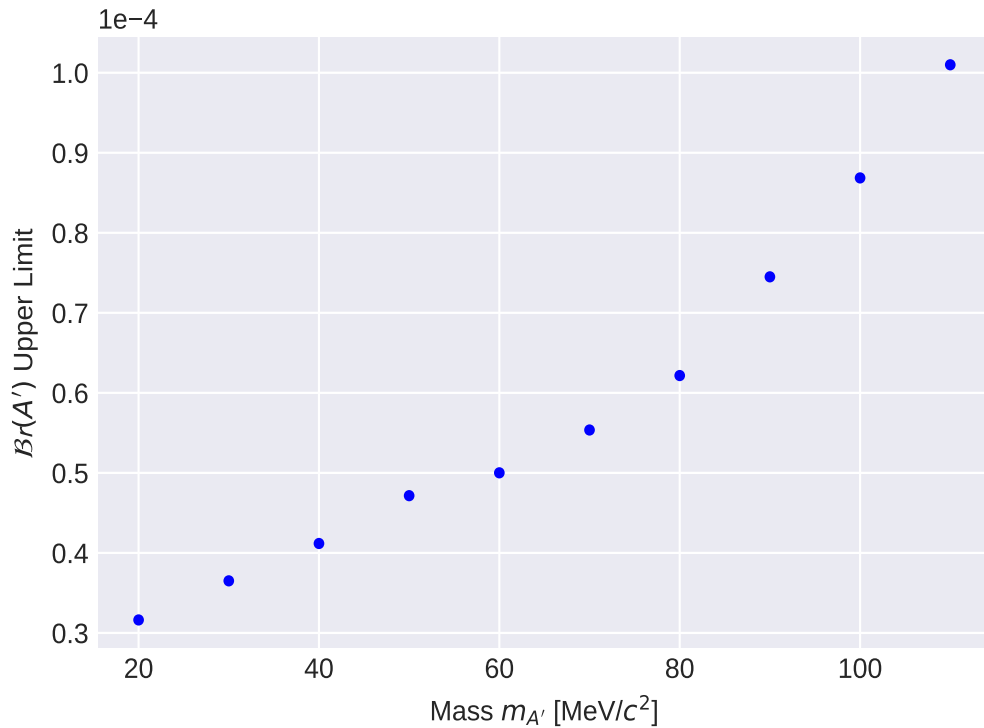


Figure 7.6. Upper limit of $Br(K^+ \rightarrow \mu^+ \nu A')$ under the condition that three TOF1 counters have fired.

Due to the aforementioned background from the dominant $K_{\mu 2}$ component, a momentum cut at 230 MeV/c was applied. The e36g4MC was used to estimate the signal loss percentage as result of the momentum cut. The signal loss exhibits strong dependence on the $m_{A'}$ and drops to zero at high A' masses. This is due to kinematic suppression of high $m_{A'}$ in the parameter space of $K^+ \rightarrow \mu^+ \nu A'$ decay, as well the spectrometer acceptance.

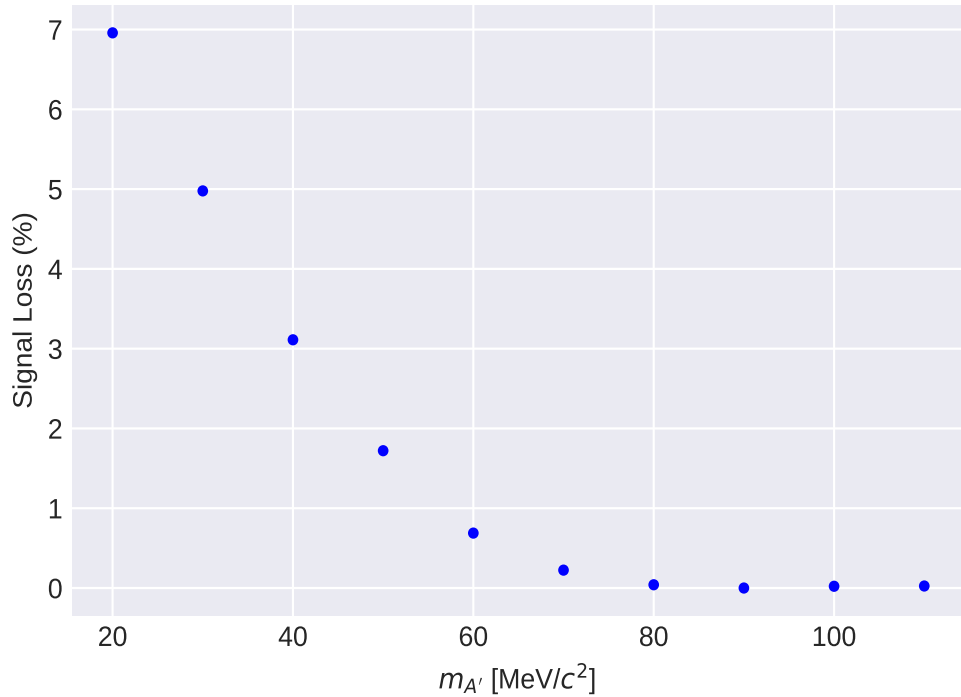


Figure 7.7. Signal loss percentage as a function of assumed $m_{A'}$. The signal loss drops to zero at high A' masses as a result of kinematic suppression in the $K^+ \rightarrow \mu^+ \nu A'$ decay.

The invariant mass M_{ee} spectrum reflecting the background reduction as result of the endpoint momentum cut is shown in figure 7.8. The red histogram represents events satisfying the A' trigger condition and the yellow histogram is for M_{ee} under the application of endpoint momentum cut.

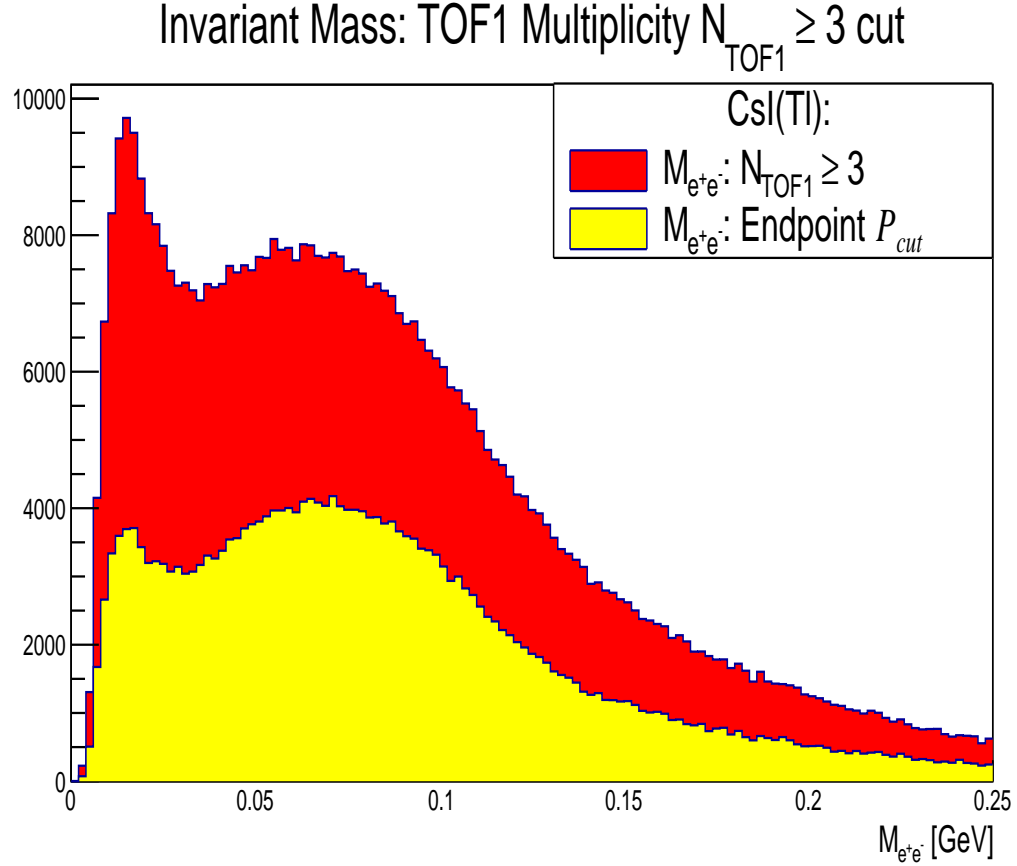


Figure 7.8. The invariant mass M_{ee} under the condition that at three TOF1 counters have registered a hit (red). The yellow histogram shows the M_{ee} once the endpoint momentum cut was applied, as a means of reducing the $K_{\mu 2}$ contamination.

The resulting upper limits on $\mathcal{Br}(A')$ under the momentum cut at 230 MeV/ c are presented in figure 7.9. They are $\mathcal{O}(10^{-5})$ with only about 5% of the data analyzed. They demonstrate a strong dependence on the A' mass, as the kinematic suppression at high $m_{A'}$ and low signal acceptance at higher masses drive up $\mathcal{Br}(A')$ thereby reducing the sensitivity.

7.3 Conclusion and Outlook

The TREK/E36 experiment has completed its data-taking and has been decommissioned as of March 2016. A Geant4 and ROOT based MC, e36g4MC, was developed

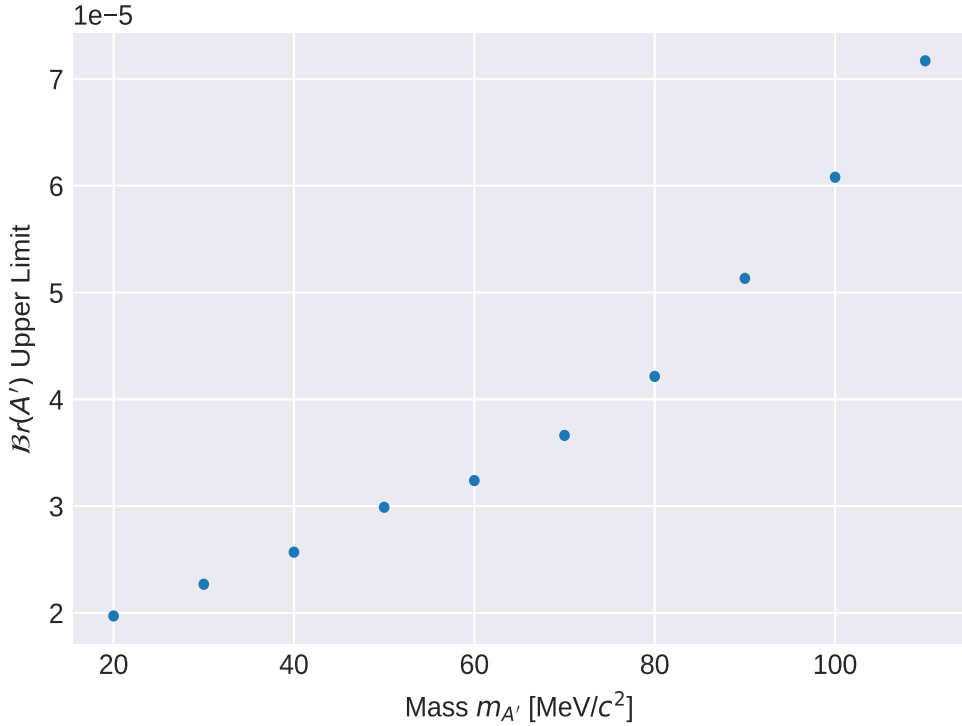


Figure 7.9. Upper limit of $\mathcal{B}r(A')$ under the condition that three TOF1 counters have fired and a 230 MeV/ c was applied.

to assist with rare kaon decay searches for light neutral bosons. The e36g4MC was vetted and found to be in agreement the tracking package. Furthermore the material budget between the e36g4MC and the tracking package were found to be in agreement. A search for the A' production in the $K^+ \rightarrow \mu^+ \nu A'$, followed by the prompt decay of $A' \rightarrow e^+ e^-$ along with a charged particle that was detected and tracked in the spectrometer gap, was performed using data from the TREK/E36 experiment. The sensitivity of TREK/E36 to A' production was evaluated via upper limits of the branching ratios $\mathcal{B}r(A')$ as a function of $m_{A'}$ and found were to be $\mathcal{O}(10^{-5})$, with about 8% of the data analyzed. The experimental limit from the Carlson model for a new light neutral with polar (scalar) and axial vector (pseudoscalar) couplings are $\mathcal{O}(-6)$, see figure 3.13. The e36g4MC toolkit was used in calculation of A' acceptances

as well for background suppression of $K_{\mu 2}$ muons. The π^+ from $K_{\pi 2}$ decays as well as e^+ from $K_{e 3}$ contributed to the irreducible background in the charged particle momentum spectrum, and thereby reduced the sensitivity of our probe. A thorough PID analysis, which is currently underway, will serve to reduce the background, thereby increasing the sensitivity of TREK/E36. The π^+ contribution can be removed by mass squared cut and e^+ 's can be removed by a full PID analysis utilizing the AC, PGC and TOF counters, as highly energetic muons can produce delta electrons in the AC counters.

Finally, a fully digitized and realistic e36g4MC would be instrumental in further studies of light neutral bosons. A fully digitized e36g4MC would be essential in providing a realistic description of detector responses as well as a full reproduction of known SM backgrounds. As a result the e36g4MC would play a pivotal role in reducing the SM backgrounds and increase our sensitivity to A' production.

REFERENCES

- [1] C. Rangacharyulu, et al. J-PARC Experimental Proposal Measurement of $\Gamma(K^+ \rightarrow e^+)/\Gamma(K^+ \rightarrow \mu^+\nu)$ and Search for heavy sterile neutrinos using the TREK detector system.
- [2] Douglas A. Bryman. $\pi \rightarrow e$ neutrino decay: Window on the generation puzzle. *Comments Nucl. Part. Phys.*, 21(2):101–121, 1993.
- [3] Vincenzo Cirigliano and Ignasi Rosell. Two-loop effective theory analysis of $\pi(K) \rightarrow e \text{ anti-nu}/e [\gamma]$ branching ratios. *Phys. Rev. Lett.*, 99:231801, 2007.
- [4] Vincenzo Cirigliano and Ignasi Rosell. $\pi/K \rightarrow e\bar{\nu}_e$ branching ratios to $\mathcal{O}(e^2 p^4)$ in Chiral Perturbation Theory. *JHEP*, 10:005, 2007.
- [5] F. Ambrosino et al. Precise measurement of $\Gamma(K \rightarrow e\nu(\gamma))/\Gamma(K \rightarrow \mu\nu(\gamma))$ and study of $K \rightarrow e\nu\gamma$. *Eur. Phys. J. C*, 64:627–636, 2009. [Erratum: Eur.Phys.J. 65, 703 (2010)].
- [6] C. Lazzeroni et al. Precision Measurement of the Ratio of the Charged Kaon Leptonic Decay Rates. *Phys. Lett. B*, 719:326–336, 2013.
- [7] Patrizia Cenci. Rare Kaon Decays with NA48/2 and NA62 at CERN. *Int. J. Mod. Phys. Conf. Ser.*, 31:1460308, 2014.
- [8] M. Tanabashi et al. Review of Particle Physics. *Phys. Rev.*, D98(3):030001, 2018.
- [9] James D. Bjorken, Rouven Essig, Philip Schuster, and Natalia Toro. New Fixed-Target Experiments to Search for Dark Gauge Forces. *Phys. Rev.*, D80:075018, 2009.

- [10] David Tucker-Smith and Itay Yavin. Muonic hydrogen and MeV forces. *Phys. Rev. D*, 83:101702, 2011.
- [11] Brian Batell, David McKeen, and Maxim Pospelov. New Parity-Violating Muonic Forces and the Proton Charge Radius. *Phys. Rev. Lett.*, 107:011803, 2011.
- [12] Carl E. Carlson and Benjamin C. Rislow. New Physics and the Proton Radius Problem. *Phys. Rev.*, D86:035013, 2012.
- [13] Carl E. Carlson and Benjamin C. Rislow. Constraints to new physics models for the proton charge radius puzzle from the decay $K^+ \rightarrow \mu^+ + \nu + e^- + e^+$. *Phys. Rev. D*, 89(3):035003, 2014.
- [14] Tommi Alanne, Giorgio Arcadi, Florian Goertz, Valentin Tenorth, and Stefan Vogl. Model-independent constraints with extended dark matter EFT. 6 2020.
- [15] Marco Fabbrichesi, Emidio Gabrielli, and Gaia Lanfranchi. The Dark Photon. 5 2020.
- [16] Carl E. Carlson and Michael Freid. Extending theories on muon-specific interactions. *Phys. Rev. D*, 92(9):095024, 2015.
- [17] K. Paton, et al. Measurement of T-violation Transverse Muon Polarization in $K^+ \rightarrow \pi^0 \mu^+ \nu$ Decays.
- [18] O. Mineev et al. The design and basic performance of a Spiral Fiber Tracker for the J-PARC E36 experiment. *Nucl. Instrum. Meth.*, A847:136–141, 2017.
- [19] Youichi Igarashi and Masatoshi Saito. Waveform sampler module for j-parc trek experiment. In *Waveform sampler module for J-PARC TREK experiment*, pages 1376–1379, 2012.

- [20] D. V. Dementev et al. CsI(Tl) photon detector with PIN photodiode readout for a $K_{\mu 3}$ T-violation experiment. *Nucl. Instrum. Meth.*, A440:151–171, 2000.
- [21] Y. Miyazaki et al. Performance test of a lead-glass counter for the J-PARC E36 experiment. *Nucl. Instrum. Meth.*, A779:13–17, 2015.
- [22] Katherine Freese. Status of Dark Matter in the Universe. *Int. J. Mod. Phys.*, 1(06):325–355, 2017.
- [23] Gianfranco Bertone and M.P. Tait, Tim. A new era in the search for dark matter. *Nature*, 562(7725):51–56, 2018.
- [24] R. Bernabei et al. The DAMA/LIBRA apparatus. *Nucl. Instrum. Meth. A*, 592:297–315, 2008.
- [25] Oscar Adriani et al. An anomalous positron abundance in cosmic rays with energies 1.5–100 GeV. *Nature*, 458:607–609, 2009.
- [26] J.E. Gunn, B.W. Lee, I. Lerche, D.N. Schramm, and G. Steigman. Some Astrophysical Consequences of the Existence of a Heavy Stable Neutral Lepton. *Astrophys. J.*, 223:1015–1031, 1978.
- [27] P.J.E. Peebles. Large scale background temperature and mass fluctuations due to scale invariant primeval perturbations. *Astrophys. J. Lett.*, 263:L1–L5, 1982.
- [28] Vanda Silveira and A. Zee. Scalar Phantoms. *Phys. Lett. B*, 161:136–140, 1985.
- [29] John McDonald. Gauge singlet scalars as cold dark matter. *Phys. Rev. D*, 50:3637–3649, 1994.
- [30] C. Boehm and Pierre Fayet. Scalar dark matter candidates. *Nucl. Phys. B*, 683:219–263, 2004.

- [31] Pierre Fayet. Light spin 1/2 or spin 0 dark matter particles. *Phys. Rev. D*, 70:023514, 2004.
- [32] Maxim Pospelov, Adam Ritz, and Mikhail B. Voloshin. Secluded WIMP Dark Matter. *Phys. Lett. B*, 662:53–61, 2008.
- [33] J. Knodelseder et al. The All-sky distribution of 511 keV electron-positron annihilation emission. *Astron. Astrophys.*, 441:513–532, 2005.
- [34] Celine Boehm, Dan Hooper, Joseph Silk, Michel Casse, and Jacques Paul. MeV dark matter: Has it been detected? *Phys. Rev. Lett.*, 92:101301, 2004.
- [35] Rouven Essig, Philip Schuster, and Natalia Toro. Probing Dark Forces and Light Hidden Sectors at Low-Energy e+e- Colliders. *Phys. Rev. D*, 80:015003, 2009.
- [36] Bob Holdom. Two U(1)'s and Epsilon Charge Shifts. *Phys. Lett. B*, 166:196–198, 1986.
- [37] Jim Alexander et al. Dark Sectors 2016 Workshop: Community Report. 2016.
- [38] Brian Batell, Maxim Pospelov, and Adam Ritz. Exploring Portals to a Hidden Sector Through Fixed Targets. *Phys. Rev.*, D80:095024, 2009.
- [39] F. Zwicky. On the Masses of Nebulae and of Clusters of Nebulae. *Astrophys. J.*, 86:217–246, 1937.
- [40] V. C. Rubin, N. Thonnard, and W. K. Ford, Jr. Rotational properties of 21 SC galaxies with a large range of luminosities and radii, from NGC 4605 /R = 4kpc/ to UGC 2885 /R = 122 kpc/. *Astrophys. J.*, 238:471, 1980.
- [41] E. Komatsu et al. Five-Year Wilkinson Microwave Anisotropy Probe (WMAP) Observations: Cosmological Interpretation. *Astrophys. J. Suppl.*, 180:330–376, 2009.

- [42] P.A.R. Ade et al. Planck 2015 results. XIII. Cosmological parameters. *Astron. Astrophys.*, 594:A13, 2016.
- [43] Jennifer K. Adelman-McCarthy et al. The Fourth Data Release of the Sloan Digital Sky Survey. *Astrophys. J. Suppl.*, 162:38–48, 2006.
- [44] J.Anthony Tyson, Greg P. Kochanski, and Ian P. Dell’Antonio. Detailed mass map of CL0024+1654 from strong lensing. *Astrophys. J. Lett.*, 498:L107, 1998.
- [45] A. Del Popolo. Nonbaryonic Dark Matter in Cosmology. *Int. J. Mod. Phys. D*, 23:1430005, 2014.
- [46] Y. Akrami et al. Planck 2018 results. I. Overview and the cosmological legacy of Planck. 7 2018.
- [47] M. Aguilar et al. Electron and Positron Fluxes in Primary Cosmic Rays Measured with the Alpha Magnetic Spectrometer on the International Space Station. *Phys. Rev. Lett.*, 113:121102, 2014.
- [48] T. Beranek and M. Vanderhaeghen. Constraints on the Dark Photon Parameter Space from Leptonic Rare Kaon Decays. *Phys. Rev.*, D87(1):015024, 2013.
- [49] T. Aoyama et al. The anomalous magnetic moment of the muon in the Standard Model. 6 2020.
- [50] Michel Davier, Andreas Hoecker, Bogdan Malaescu, and Zhiqing Zhang. Reevaluation of the hadronic vacuum polarisation contributions to the Standard Model predictions of the muon $g - 2$ and $\alpha(m_Z^2)$ using newest hadronic cross-section data. *Eur. Phys. J. C*, 77(12):827, 2017.
- [51] Alexander Keshavarzi, Daisuke Nomura, and Thomas Teubner. Muon $g - 2$ and $\alpha(M_Z^2)$: a new data-based analysis. *Phys. Rev. D*, 97(11):114025, 2018.

- [52] Gilberto Colangelo, Martin Hoferichter, and Peter Stoffer. Two-pion contribution to hadronic vacuum polarization. *JHEP*, 02:006, 2019.
- [53] Martin Hoferichter, Bai-Long Hoid, and Bastian Kubis. Three-pion contribution to hadronic vacuum polarization. *JHEP*, 08:137, 2019.
- [54] M. Davier, A. Hoecker, B. Malaescu, and Z. Zhang. A new evaluation of the hadronic vacuum polarisation contributions to the muon anomalous magnetic moment and to $\alpha(m_Z^2)$. *Eur. Phys. J. C*, 80(3):241, 2020. [Erratum: Eur.Phys.J.C 80, 410 (2020)].
- [55] Alexander Keshavarzi, Daisuke Nomura, and Thomas Teubner. $g - 2$ of charged leptons, $\alpha(M_Z^2)$, and the hyperfine splitting of muonium. *Phys. Rev. D*, 101(1):014029, 2020.
- [56] Alexander Kurz, Tao Liu, Peter Marquard, and Matthias Steinhauser. Hadronic contribution to the muon anomalous magnetic moment to next-to-next-to-leading order. *Phys. Lett. B*, 734:144–147, 2014.
- [57] Kirill Melnikov and Arkady Vainshtein. Hadronic light-by-light scattering contribution to the muon anomalous magnetic moment revisited. *Phys. Rev. D*, 70:113006, 2004.
- [58] Pere Masjuan and Pablo Sanchez-Puertas. Pseudoscalar-pole contribution to the $(g_\mu - 2)$: a rational approach. *Phys. Rev. D*, 95(5):054026, 2017.
- [59] Gilberto Colangelo, Martin Hoferichter, Massimiliano Procura, and Peter Stoffer. Dispersion relation for hadronic light-by-light scattering: two-pion contributions. *JHEP*, 04:161, 2017.

- [60] Martin Hoferichter, Bai-Long Hoid, Bastian Kubis, Stefan Leupold, and Sebastian P. Schneider. Dispersion relation for hadronic light-by-light scattering: pion pole. *JHEP*, 10:141, 2018.
- [61] Antoine Gérardin, Harvey B. Meyer, and Andreas Nyffeler. Lattice calculation of the pion transition form factor with $N_f = 2 + 1$ Wilson quarks. *Phys. Rev. D*, 100(3):034520, 2019.
- [62] Johan Bijnens, Nils Hermansson-Truedsson, and Antonio Rodríguez-Sánchez. Short-distance constraints for the HLbL contribution to the muon anomalous magnetic moment. *Phys. Lett. B*, 798:134994, 2019.
- [63] Gilberto Colangelo, Franziska Hagelstein, Martin Hoferichter, Laetitia Laub, and Peter Stoffer. Longitudinal short-distance constraints for the hadronic light-by-light contribution to $(g - 2)_\mu$ with large- N_c Regge models. *JHEP*, 03:101, 2020.
- [64] Gilberto Colangelo, Martin Hoferichter, Andreas Nyffeler, Massimo Passera, and Peter Stoffer. Remarks on higher-order hadronic corrections to the muon g-2. *Phys. Lett. B*, 735:90–91, 2014.
- [65] Thomas Blum, Norman Christ, Masashi Hayakawa, Taku Izubuchi, Luchang Jin, Chulwoo Jung, and Christoph Lehner. Hadronic Light-by-Light Scattering Contribution to the Muon Anomalous Magnetic Moment from Lattice QCD. *Phys. Rev. Lett.*, 124(13):132002, 2020.
- [66] Tatsumi Aoyama, Masashi Hayakawa, Toichiro Kinoshita, and Makiko Nio. Complete Tenth-Order QED Contribution to the Muon g-2. *Phys. Rev. Lett.*, 109:111808, 2012.
- [67] Tatsumi Aoyama, M. Hayakawa, Toichiro Kinoshita, and Makiko Nio. Tenth-Order Electron Anomalous Magnetic Moment — Contribution of Diagrams

- without Closed Lepton Loops. *Phys. Rev. D*, 91(3):033006, 2015. [Erratum: Phys. Rev. D 96, 019901 (2017)].
- [68] Andrzej Czarnecki, William J. Marciano, and Arkady Vainshtein. Refinements in electroweak contributions to the muon anomalous magnetic moment. *Phys. Rev. D*, 67:073006, 2003. [Erratum: Phys. Rev. D 73, 119901 (2006)].
- [69] C. Gnendiger, D. Stöckinger, and H. Stöckinger-Kim. The electroweak contributions to $(g - 2)_\mu$ after the Higgs boson mass measurement. *Phys. Rev. D*, 88:053005, 2013.
- [70] G.W. Bennett et al. Final Report of the Muon E821 Anomalous Magnetic Moment Measurement at BNL. *Phys. Rev. D*, 73:072003, 2006.
- [71] Chen-Ning Yang and Robert L. Mills. Conservation of Isotopic Spin and Isotopic Gauge Invariance. *Phys. Rev.*, 96:191–195, 1954.
- [72] A. J. Krasznahorkay et al. New results on the ${}^8\text{Be}$ anomaly. *J. Phys. Conf. Ser.*, 1056(1):012028, 2018.
- [73] Jonathan L. Feng, Bartosz Fornal, Iftah Galon, Susan Gardner, Jordan Smolinsky, Tim M. P. Tait, and Philip Tanedo. Protophobic Fifth-Force Interpretation of the Observed Anomaly in ${}^8\text{Be}$ Nuclear Transitions. *Phys. Rev. Lett.*, 117(7):071803, 2016.
- [74] A.J. Krasznahorkay et al. New evidence supporting the existence of the hypothetical X17 particle. 10 2019.
- [75] Jonathan L. Feng, Tim M.P. Tait, and Christopher B. Verhaaren. Dynamical Evidence For a Fifth Force Explanation of the ATOMKI Nuclear Anomalies. 6 2020.
- [76] Randolph Pohl et al. The size of the proton. *Nature*, 466:213–216, 2010.

- [77] W. Xiong et al. A small proton charge radius from an electron–proton scattering experiment. *Nature*, 575(7781):147–150, 2019.
- [78] Peter J. Mohr, David B. Newell, and Barry N. Taylor. CODATA Recommended Values of the Fundamental Physical Constants: 2014. *Rev. Mod. Phys.*, 88(3):035009, 2016.
- [79] Aldo Antognini et al. Proton Structure from the Measurement of $2S - 2P$ Transition Frequencies of Muonic Hydrogen. *Science*, 339:417–420, 2013.
- [80] Axel Beyer et al. The Rydberg constant and proton size from atomic hydrogen. *Science*, 358(6359):79–85, 2017.
- [81] Hélène Fleurbaey, Sandrine Galtier, Simon Thomas, Marie Bonnaud, Lucile Julien, François Biraben, François Nez, Michel Abgrall, and Jocelyne Guéna. New Measurement of the $1S - 3S$ Transition Frequency of Hydrogen: Contribution to the Proton Charge Radius Puzzle. *Phys. Rev. Lett.*, 120(18):183001, 2018.
- [82] J.C. Bernauer et al. High-precision determination of the electric and magnetic form factors of the proton. *Phys. Rev. Lett.*, 105:242001, 2010.
- [83] J. Arrington, W. Melnitchouk, and J.A. Tjon. Global analysis of proton elastic form factor data with two-photon exchange corrections. *Phys. Rev. C*, 76:035205, 2007.
- [84] L. Schlessinger and C. Schwartz. Analyticity as a Useful Computation Tool. *Phys. Rev. Lett.*, 16:1173–1174, 1966.
- [85] L. Schlessinger. Calculation of Some Three-Body Scattering Amplitudes. *Phys. Rev.*, 171:1523–1527, 1968.

- [86] Ralf-Arno Tripolt, Idan Haritan, Jochen Wambach, and Nimrod Moiseyev. Threshold energies and poles for hadron physical problems by a model-independent universal algorithm. *Phys. Lett. B*, 774:411–416, 2017.
- [87] S. Abrahamyan et al. Search for a New Gauge Boson in Electron-Nucleus Fixed-Target Scattering by the APEX Experiment. *Phys. Rev. Lett.*, 107:191804, 2011.
- [88] James R. Boyce. An overview of dark matter experiments at Jefferson Lab. *J. Phys. Conf. Ser.*, 384:012008, 2012.
- [89] Simona Giovannella et al. U boson searches at KLOE. *J. Phys. Conf. Ser.*, 335:012067, 2011.
- [90] Bernard Aubert et al. Search for Dimuon Decays of a Light Scalar in Radiative Transitions $\tau(3S) \rightarrow \gamma A_0$. In *2009 Aspen Winter Conference on Astronomy: THIRTY YEARS OF MAGNETARS: NEW FRONTIERS*, 2 2009.
- [91] Martin Bauer, Patrick Foldenauer, Peter Reimitz, and Tilman Plehn. Light Dark Matter Annihilation and Scattering in LHC Detectors. 5 2020.
- [92] Jonathan L. Feng, Bartosz Fornal, Iftah Galon, Susan Gardner, Jordan Smolinsky, Tim M. P. Tait, and Philip Tanedo. Particle physics models for the 17 MeV anomaly in beryllium nuclear decays. *Phys. Rev. D*, 95(3):035017, 2017.
- [93] Joerg Jaeckel and Sabyasachi Roy. Spectroscopy as a test of Coulomb’s law: A Probe of the hidden sector. *Phys. Rev. D*, 82:125020, 2010.

- [94] Savy G. Karshenboim, David McKeen, and Maxim Pospelov. Constraints on muon-specific dark forces. *Phys. Rev.*, D90(7):073004, 2014. [Addendum: Phys. Rev.D90,no.7,079905(2014)].
- [95] Vernon Barger, Cheng-Wei Chiang, Wai-Yee Keung, and Danny Marfatia. Constraint on parity-violating muonic forces. *Phys. Rev. Lett.*, 108:081802, 2012.
- [96] M. Abe et al. Search for T-violating transverse muon polarization in the $K^+ \rightarrow \pi^0 \mu^+ \nu$ decay. *Phys. Rev.*, D73:072005, 2006.
- [97] M. Abe et al. Apparatus for a search for T violating muon polarization in stopped kaon decays. *Nucl. Instrum. Meth.*, A506:60–91, 2003.
- [98] Makoto Tabata et al. Assembly and bench testing of a spiral fiber tracker for the J-PARC TREK/E36 experiment. *JPS Conf. Proc.*, 8:024001, 2015.
- [99] Makoto Tabata, Akihisa Toyoda, Hideyuki Kawai, Youichi Igarashi, Jun Imazato, Suguru Shimizu, and Hirohito Yamazaki. Fabrication of silica aerogel with $n = 1.08$ for e^+/μ^+ separation in a threshold Cherenkov counter of the J-PARC TREK/E36 experiment. *Nucl. Instrum. Meth.*, A795:206–212, 2015.
- [100] H. Ito et al. Performance check of the CsI(Tl) calorimeter for the J-PARC E36 experiment by observing e^+ from muon decay. *Nucl. Instrum. Meth.*, A901:1–5, 2018.
- [101] J. Imazato, H. Tamura, T. Ishikawa, R. S. Hayano, T. Yamazaki, A. Yamamoto, and T. Kawaguchi. A Superconducting Toroidal Magnet for Charged Particle Spectroscopy. In *Proceedings, 11th International Conference on Magnet Technology (MT-11): Tsukuba, Japan, August 28-September 1, 1989*, pages 0366–371, 1989.

- [102] A. Kawachi et al. The superconducting toroidal spectrometer for hypernuclear studies at KEK PS. *Nucl. Instrum. Meth.*, A416:253–262, 1998.
- [103] P. Monaghan. Preliminary Update on TOSCA Simulations for E36. *TREK/E36 magnetic field technical note*, 2014.
- [104] R. E. Kalman. A New Approach to Linear Filtering and Prediction Problems. *Journal of Basic Engineering*, 82(1):35–45, 03 1960.
- [105] T. Cao, D. H. Dongwi, M. Kohl. Precise Measurement of $K_{e2}/K_{\mu 2}$ Branching Ratio and New Physics Search with a Stopped K^+ Beam Experiment. Gordon Research Conference, August 2018.
- [106] T. Cao. Precise Measurement of $K_{e2}/K_{\mu 2}$ Branching Ratio and New Physics Search with a Stopped K^+ Beam Experiment. Fifth Joint APS/DNP and JPS, October 2018.
- [107] Sébastien Bianchin. Precise measurement of the $K_{e2}/K_{\mu 2}$ branching ratio and search for new physics beyond the Standard Model. *J. Phys. Conf. Ser.*, 800(1):012017, 2017.
- [108] S. Bianchin. Search for non-standard model physics using the transverse muon polarization in stopped K^+ decay. *AIP Conf. Proc.*, 1441(1):567–569, 2012.
- [109] T. Cao. Precise Measurement of $R_K = \Gamma(K^+ \rightarrow e^+\nu)/\Gamma(K^+ \rightarrow \mu^+\nu)$ and Search for New Physics by the TREK-E-36 Experiment. Division of Nuclear Physics (APS/DNP), October 2017.
- [110] Physics reference manual, available online from: <http://www.geant4.org>.
- [111] Gert Moliere. Theory of Scattering of Fast Charged Particles: Part II. Plural and Multiple Scattering. 1947.

- [112] S. Goudsmit and J. L. Saunderson. Multiple Scattering of Electrons. *Phys. Rev.*, 57:24–29, 1940.
- [113] Virgil L. Highland. Some Practical Remarks on Multiple Scattering. *Nucl. Instrum. Meth.*, 129:497, 1975.
- [114] S. Agostinelli et al. GEANT4: A Simulation toolkit. *Nucl. Instrum. Meth.*, A506:250–303, 2003.
- [115] Vladimir Ivanchenko et al. Recent improvements in geant4 electromagnetic physics models and interfaces. *Progress in NUCLEAR SCIENCE and TECHNOLOGY*, 2:898–903, 10 2011.
- [116] J. Apostolakis et al. Geometry and physics of the Geant4 toolkit for high and medium energy applications. *Radiat. Phys. Chem.*, 78(10):859–873, 2009.
- [117] J. Allison et al. Recent developments in Geant4. *Nucl. Instrum. Meth.*, A835:186–225, 2016.
- [118] G. A. P. Cirrone, G. Cuttone, F. Di Rosa, L. Pandola, F. Romano, and Q. Zhang. Validation of the Geant4 electromagnetic photon cross-sections for elements and compounds. *Nucl. Instrum. Meth.*, A618:315–322, 2010.
- [119] Douglas Hasell and Uwe Schneekloth. The OLYMPUS Experiment at DESY. *Nucl. Phys. News*, 28(1):20–24, 2018.
- [120] R. Corliss. Searching for a dark photon with DarkLight. *Nucl. Instrum. Meth. A*, 865:125–127, 2017.
- [121] R. Gilman et al. Technical Design Report for the Paul Scherrer Institute Experiment R-12-01.1: Studying the Proton "Radius" Puzzle with μp Elastic Scattering. 9 2017.

- [122] Root data analysis framework, user's guide, available online from: <https://root.cern.ch/root/html/doc/guides/users-guide/ROOTUsersGuide.html>.
- [123] D. H. Dongwi. Notes On E36 Detector Installation Process. *TREK/E36 installation technical note*, 2014.

APPENDICES

APPENDIX A

AUTHOR'S CONTRIBUTIONS TO TREK/E36

The list below highlights the authors' contributions to the TREK/E36 experiment in the phases of detector installation, maintenance and repair, slow control software set-up, MC simulation development, decommissioning and data analysis. Unless otherwise stated the tasks described below were performed solely by the author. The tasks are as follows:

- Development of the TREK/E36 simulation code (e36g4MC), starting with only target and CsI codes written by Dr. Steffen Strauch (U. South Carolina)
- Incorporation of the a standalone generator (written by Dr. Tongtong Cao, U. New Hampshire) in the e36g4MC
- Together with Tongtong, worked to make sure the e36g4MC and the tracking package were consistent
- Studied different current values using the TOSCA generated magnetic field maps in order to determine the optimal current at which to run the toroidal spectrometer
- Tested ~ 200 MWPC post amplifiers to determine which ones were viable for use in the experiment
- Installation of the tracking detector elements (C2, C3 and C4), with Jun and Sebastien
- Together with Dr. Sebastien Bianchin (U. British Columbia), repaired puncture C2 cathode window with kapton tape
- Repaired broken C3 anode wire (needed to be re-strung)
- Performed misalignment measurements of the C2 detectors and TOF2 counters with Jun and Satoshi
- Together with Dr. Jun Imazato (KEK), installed TTC counters and performed light leakage tests
- Together with Sebastien, assembled TOF2 and gap veto counter frames
- Together with Sebastien, installed TOF2 and gap veto counters

- Together with Jun, Sebastien and Satoshi, laid the CsI, MWPC, TOF, PGC, Target, SFT, TTC, AC and delay cables
- Together with Jun, fixed light leakage of TOF2 counters
- Performed pedestal study of TOF1, AC and TOF2, with Jun and Mr. Satoshi Kodama (Chiba U.)
- Provided tech support for DAQ system when it would crash and failed to restart, often running a backup DAQ software was needed
- Set up high voltage slow control software for LeCroy1458 power supply
- Conducted a rudimentary study of the AC pedestal and discovered that it was random from run-to-run as well gap-to-gap
- Performed a rudimentary study of acceptance ratio for different current value of the toroidal spectrometer
- Participated heavily in the decommissioning of the TREK/E36 apparatus
- Developed of CsI calibration routine for all 768 crystals
- Developed converter software, that takes target ROOT files as inputs and converts them into **Cooker** friendly format
- Developed of CsI cluster algorithm to study two-cluster events
- Extracted the $\mathcal{Br}(A')$ upper limits
- Developed CsI and TOF (M^2) analysis routines for the e36g4MC

APPENDIX B

DETECTOR INSTALLATION AND COMMISSIONING

The installation and commissioning of the TREK/E36 detectors was conducted between Fall of 2014 (September/October) and the Summer of 2015 (May/June). The Physics run and data taking was performed in the Fall of 2015, and the decommissioning took place during the early spring of 2016. A simple timeline outlining the installation, commissioning and data taking of the TREK/E36 experiment is shown in figure B.1 below and further details follow soon after.

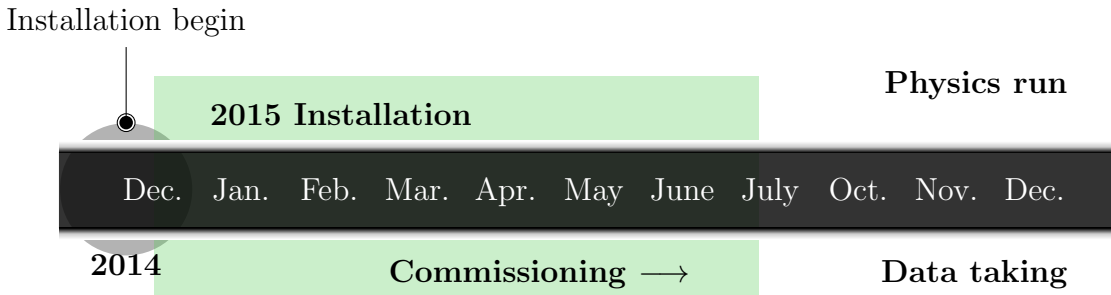


Figure B.1. Timeline.

The first 12 days of installation laid the foundation, know-how and protocol for installing various detectors which resulted in significant progress. This is why first 12 days of installation are covered in detail below. These notes were taken from the author's daily electronic journal [123], which serves as a first hand account of the days' activities, and highlights the authors' contributions during the detector installation phase of the TREK/E36 experiment.

B.1 Installation Day 1

Detector installation for the TREK/E36 experiment began on December 09, 2014. During the first day of detector installation, gap veto (GV) counters were installed in gaps 5, 6 and 7; additionally three C2 chambers were installed at the entrance of gaps 5, 6 and 7. In order for the installation of the GV counters to take place the following tasks needed to be completed [123]:

- Frames to hold GV counters were assembled
- The assembled GV counter frames were installed into the aforementioned magnet gaps
- Fastened the GV counter frames onto the iron frame of the toroidal magnet using a spacer to tilt the GV frames at an angle of 15°

A finished GV frame is shown in figure B.2, alongside a picture showing the insertion of the frame into a given magnet gap. The GV counters were subsequently installed into their respective gaps.

Three C2 chambers were installed at the entrances of gaps 5, 6 and 7. Each gap entrance had a rail support onto which the C2s were mounted. In some cases after initial attempts to install the C2 chambers failed, the support rails were adjusted in order to properly and fully install the chambers [123]. The displacement of the C2 chambers as a result of this adjustment was an important source of systematic effects for the experiment and was accounted for and documented [123].

B.2 Installation Day 2

On the second day of installation, the target was removed from the SFT-TOF1-AC system. Upon removal it became clear that the SciFiber target had been pushed too far into the degrader snout. This caused the teflon wrapping around the target to form wrinkles. The target fibers were also found to have been rotated by about 15°,

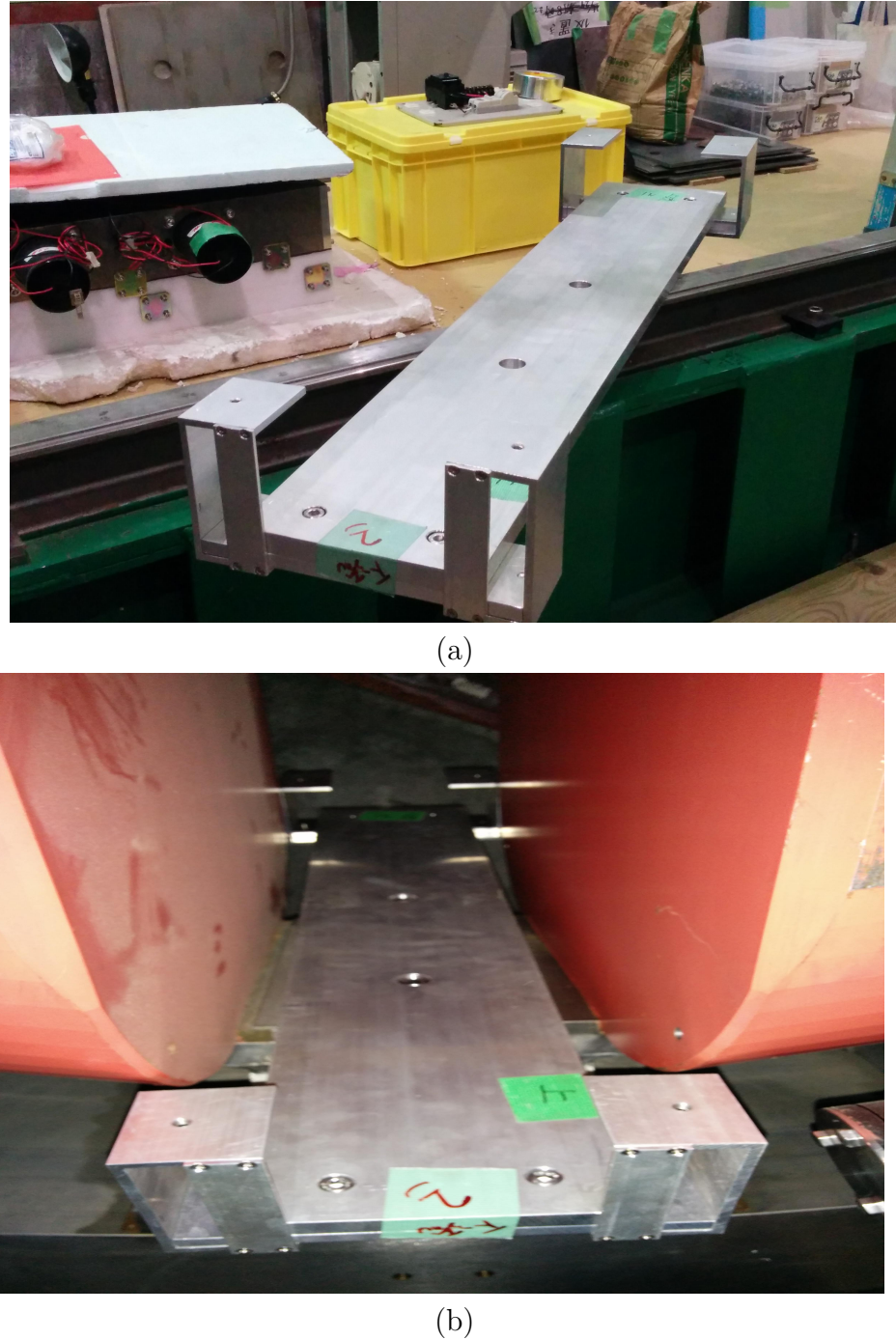
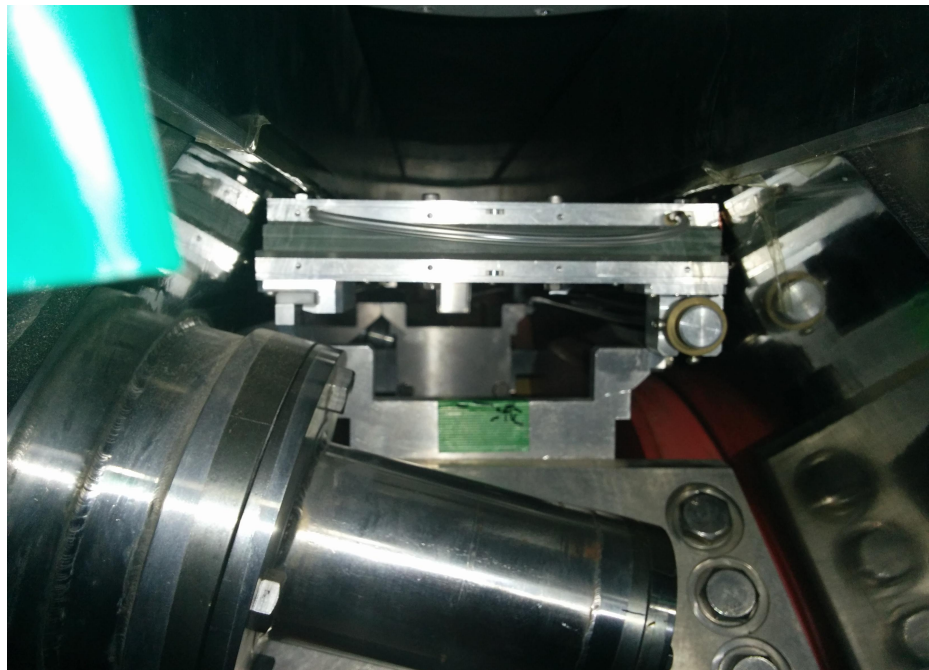


Figure B.2. Gap veto counter frame. An assembled GV counter frame (a) ready for mounting into the magnet gap. GV frame mounted into a magnet gap (b).

and were subsequently readjusted so as to remove this rotation, as shown in figure B.4 below.



(a)



(b)

Figure B.3. Dr. Shimizu Suguru (Osaka U.) and Mr. Satoshi Kodama (Chiba U.), mounting C2 onto the 6 'o clock rail.

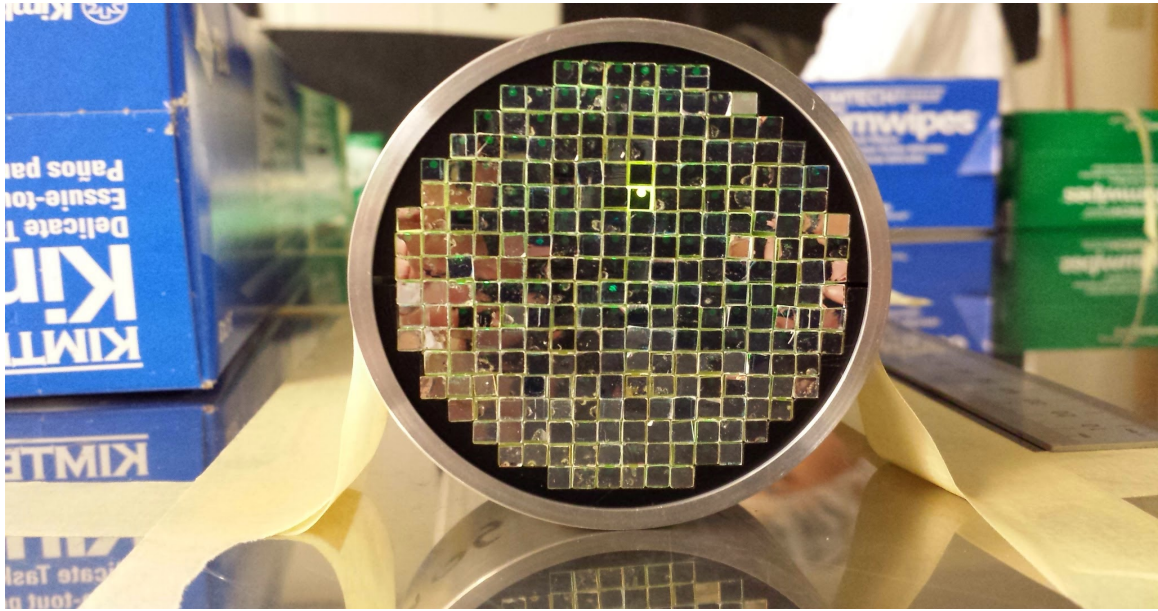


Figure B.4. Un-rotated scintillating fibers of the active target after correction.

B.3 Installation Day 3

Support frames for the TOF2 counters were assembled and built on the third day. The assembled TOF 2 frames were mounted onto the PGC wheel as shown in the figure B.5 below, in preparation for the mounting of the TOF2 counters.

Additional C2 chambers were mounted into their respective gaps, but some problems were encountered during the installation of the C2 in the 8 o'clock gap [123]. This was fixed by adjusting the C2 rail. The target rail was mounted into the experimental area in preparation for installing the target-SFT-TOF1-AC (CD) system.

B.4 Installation Day 4

The target rail mounting was completed on day 4 of installation [123]. The target rail was craned into the experimental area. This activity is shown in figure B.6. Problems were encountered with the alignment of the target rail and were subsequently fixed:

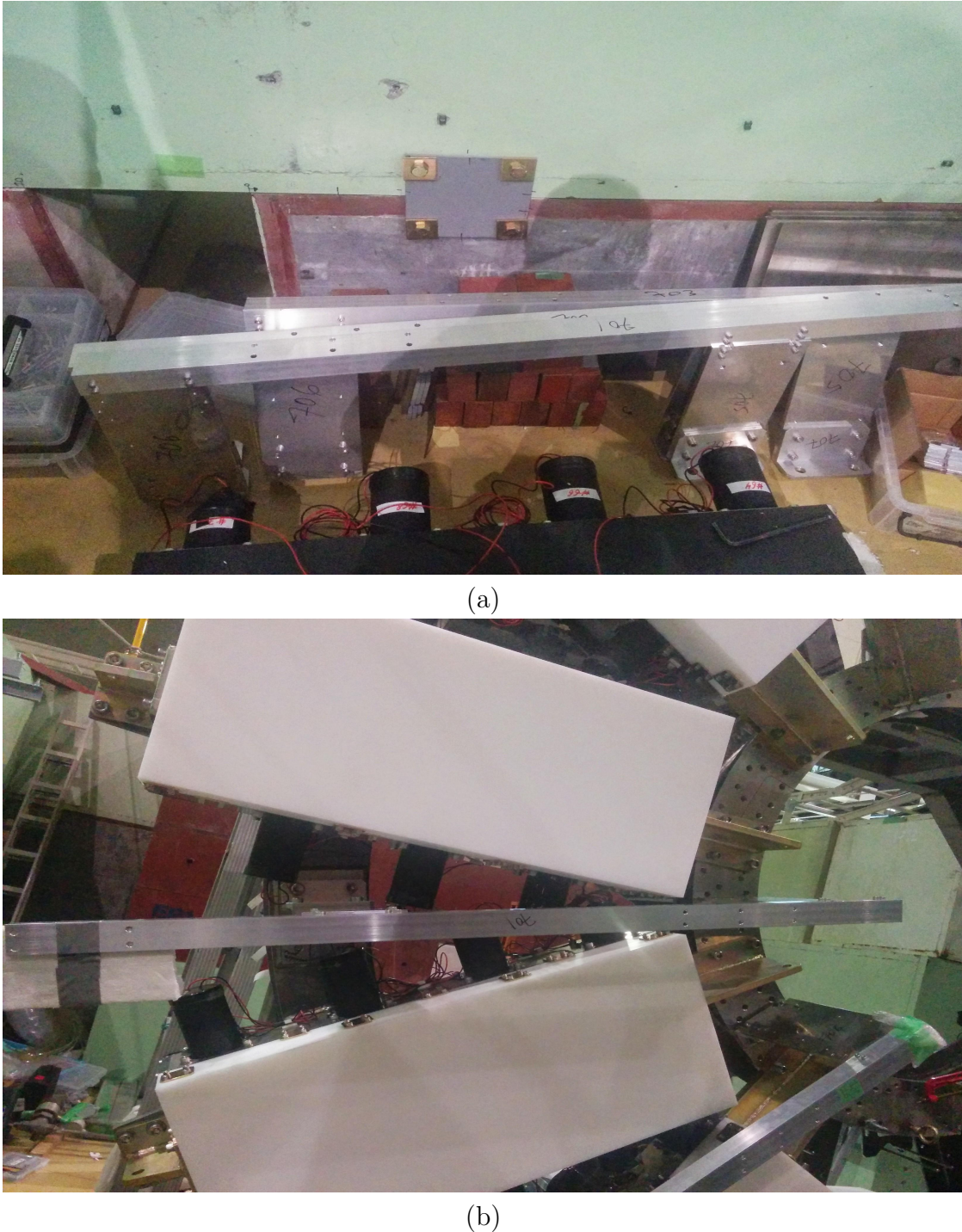


Figure B.5. TOF2 support frames. A TOF 2 support frame ready for mounting onto the PGC-wheel is shown in (a) and (b) shows mounted support frames in the 8 and 9 o'clock gaps.

- Loosened the bolts at the base of the rail support

- Adjusted the end of the target rail that attaches to the target support until alignment was reached
- Once alignment was reached, re-fastened the formerly loosened base bolts

Once the target rail was mounted and properly aligned, preparation for mounting the CD system was conducted at the end of the day. The CD system is shown in figure B.7, and the following procedure was used to prepare the CD system for installation into the CsI(Tl) detector [123]:

- Wrapped SFT in protective bubble wrap
- Neatly wound SFT around the ends of the CD

TOF2 frames were mass produced and prepared for mounting onto the PGC wheel.

B.5 Installation Day 5

The main tasks of the day were focused on mounting PGC counters onto the PGC-wheel and installing the CD system into the CsI barrel. Mounting of the gap 6 PGC counter was performed by hired specialist crane operators. Since a given PGC module weights 26.7 kg, a total stack of the six o'clock gap modules weights a combined 160.2 kg (6×26.7 kg). Only six modules were used for the six o'clock gap [123]. For this reason the PGC counter was craned and then mounted onto the PGC-wheel which can be seen in figure B.8 below [123]:

Installation of CD system followed suit after the installation of the PGC counter because these tasks could not be performed in concert. The CD system (excluding the target) was craned into the experimental area, mounted onto the target rail and was then inserted into the CsI barrel. Craning of the CD system was performed as follows [123]:

- Craned the CD system onto the rails
- Mounted the CD system onto the rails to enable sliding along the rails



Figure B.6. Target rail being craned and mounted.

- Slid the CD system into the CsI barrel

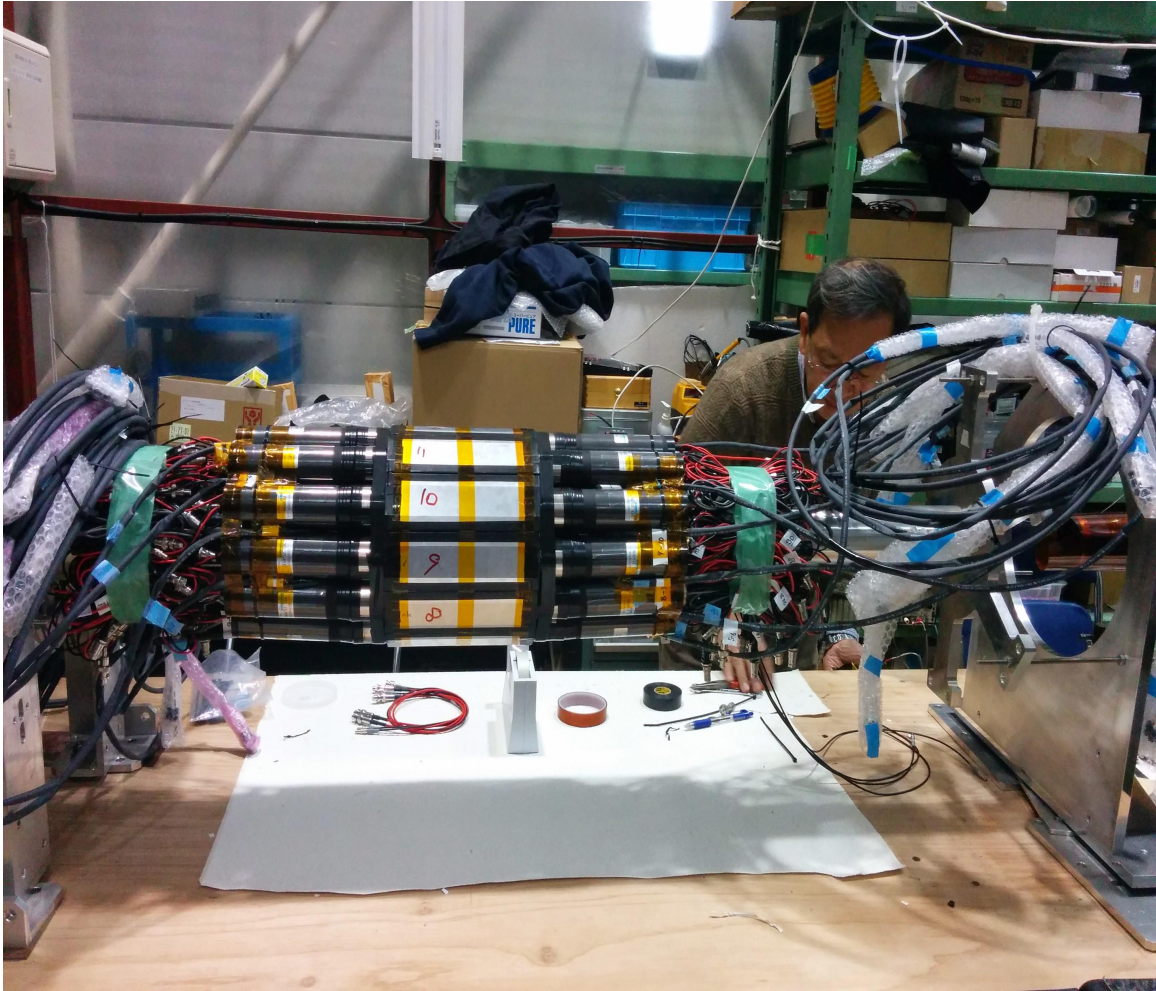


Figure B.7. The CD system prepared for installation.

B.6 Installation Day 6

The objective of the day was to mount the target onto the rails. Installation of the CD system from the previous day was carried out without the target. The target was transported from the Hadron Assembly Hall to the Hadron Hall. A crane was used to mount the target onto the rails. This is shown in figure B.10 below.

Once the target was mounted onto the rails, it was installed by sliding it along the rails. A target support frame was designed in a way such that the target could be adjusted both vertically and horizontally in order to be able to install the target into



Figure B.8. Mounting of the 6 o'clock PGC counter onto the PGC-wheel.

the Al column of the CD system. Below is a figure B.11 showing the target partially installed into the CD system.

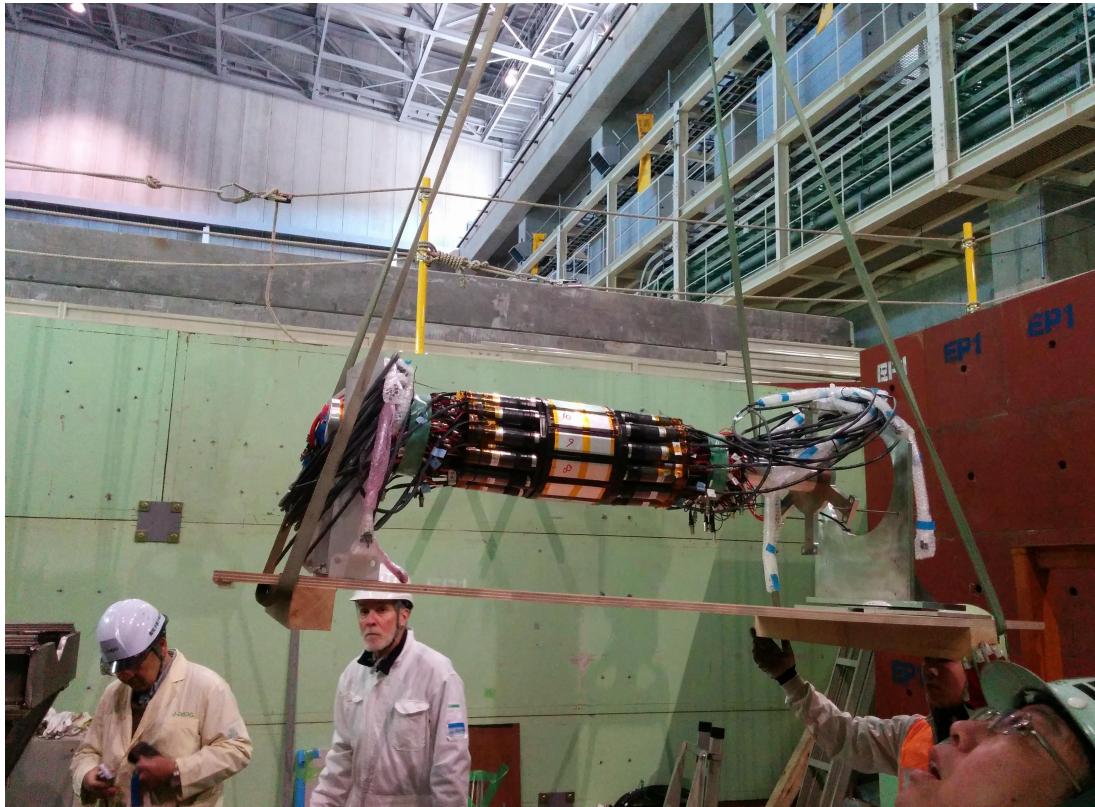


Figure B.9. Craning of the CD system (excluding the target) onto the rails to prepare for insertion into the CsI barrel.

Having confidence that the target could be inserted into the Al snout without difficulty, the entire target was removed from the CD system in order to free up space for the installation of other detectors as well as for cabling purposes. Upon removal the target showed no obvious signs of physical damage. There was however an ≈ 2 mm sag of SciFibers relative to the Al snout [123].

B.7 Installation Day 7

Some C2 chambers had long bolts that protruded and needed to be replaced [123]. The main task of the day was centered on replacing these long bolts with shorter ones in order to facilitate the installation of the C2s [123]. Upon completion of this task



Figure B.10. Target being craned onto the rails and prepared for installation.

three C2s were mounted and installed into gaps 1, 11 and 12 [123]. This brought the total number of installed C2s to 10 with only two chambers remaining to be installed.

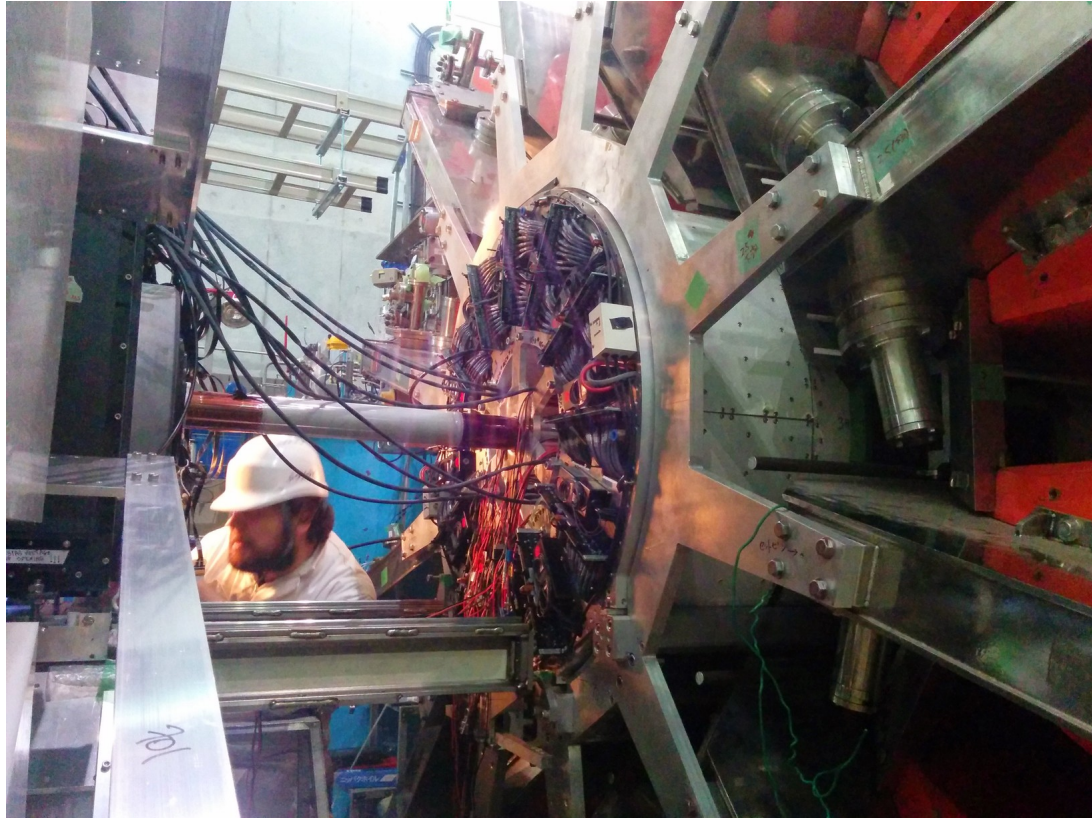


Figure B.11. Partially installed target into the Al snout of the CD system.

B.8 Installation Day 8

GV counters were installed into gaps 1, 2, 3 and 8. Preparations were made for the installation of C3 and C4 chambers at the exit of the magnet gaps. The C3-C4 transportation jig was complicated and was disassembled to enable the installation of the C3 chambers [123]. The jig was reassembled in order to install the C4 chambers. The main task was disassembling the transportation jig of the C3-C4 system [123]. This is jig is shown figure B.12 below.

B.9 Installation Day 9

Following the success of the previous day in disassembling the transportation jigs of the C3-C4 system, installation of the C3 chambers commenced and four chambers



Figure B.12. A pair of C3-C4 assembly jigs

were installed into gaps 2, 4, 8 and 9. This installation was very particular and is outlined as follows [123]:

- Removed the MWPC base plate from the transportation jig
- Used four spacers to mount the MWPC base plate onto magnet pole face
- Aligned MWPC base plate relative to the pole face of the magnet
- Mounted C3 chambers onto the MWPC base plates accordingly

Figure B.13 shows a mounted MWPC base plate onto the magnet pole face [123]. Following the successful mounting of the MWPC base plates onto the magnet pole faces, C3 chambers were mounted onto the base plates. This is shown the figure B.14 below. In addition GV counter frames were installed concurrently with the installation of the C3 chambers. All twelve GV counter frames were installed as of day 9 [123].

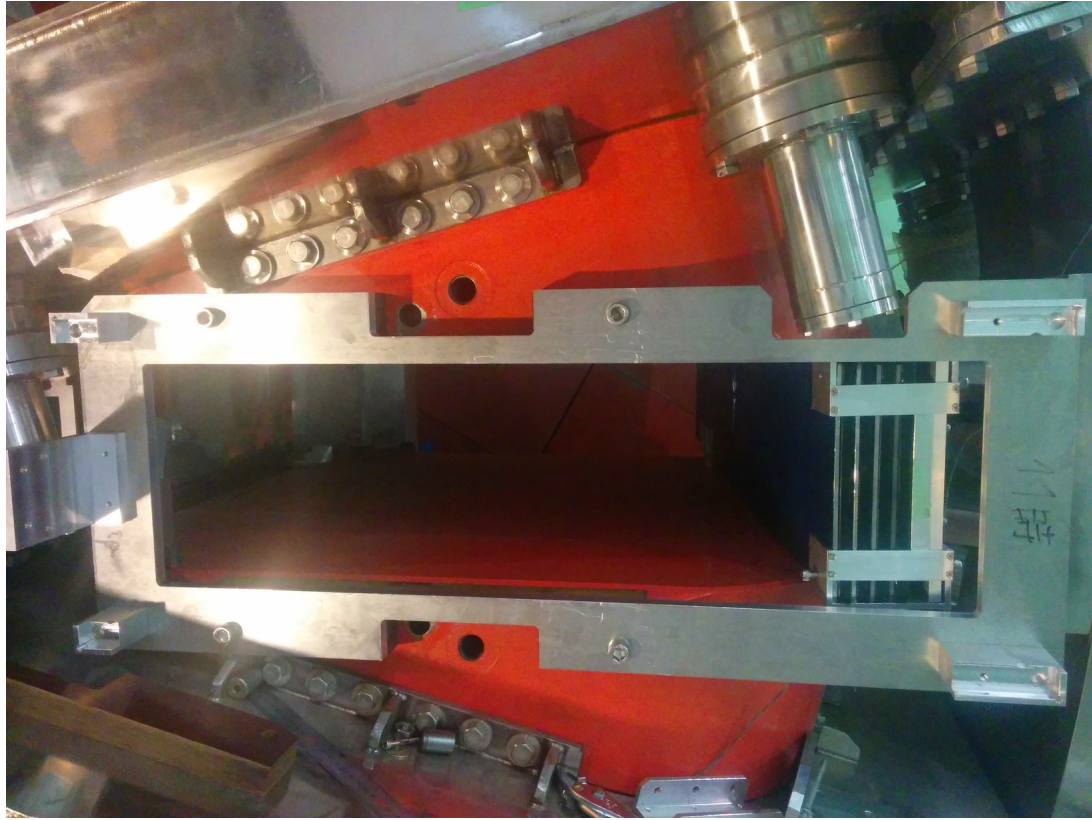


Figure B.13. A mounted MWPC base plate onto the pole face of the magnet.

B.10 Installation Day 10

Installation of the C3 chambers continued from the previous day and C4 chambers were installed into gaps 1 and 3. GV counters were also mounted into gaps 9 and 12. More C3 and C4 chambers were delivered to the Hadron Hall from the Hadron Assembly Hall and preparation procedures for installing these chambers commenced in accordance with the aforementioned procedure. Complete and partial installation of C3 and C4 chambers are shown in figure B.15 below [123].

B.11 Installation Day 11

All of the remaining GV counters were installed on the 11th day [123]. Upon completion of GV counter installation, PMTs were attached to the counters using

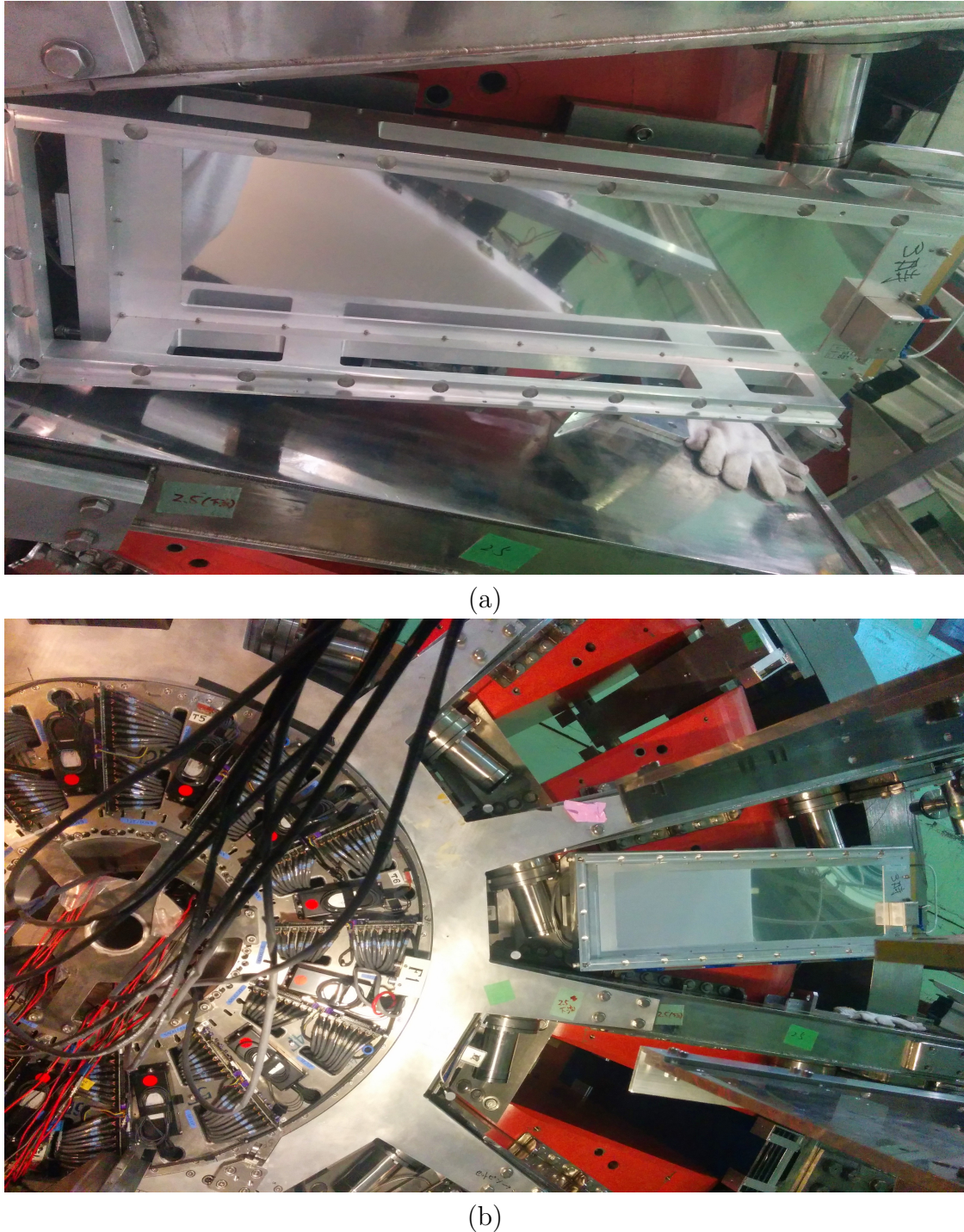


Figure B.14. A mounted C3 chamber onto a MWPC base plate.

optical glue. Figure B.16 below shows a given GV counter with a corresponding PMT attached [123]. The main task of the day was centered on aligning the MWPC

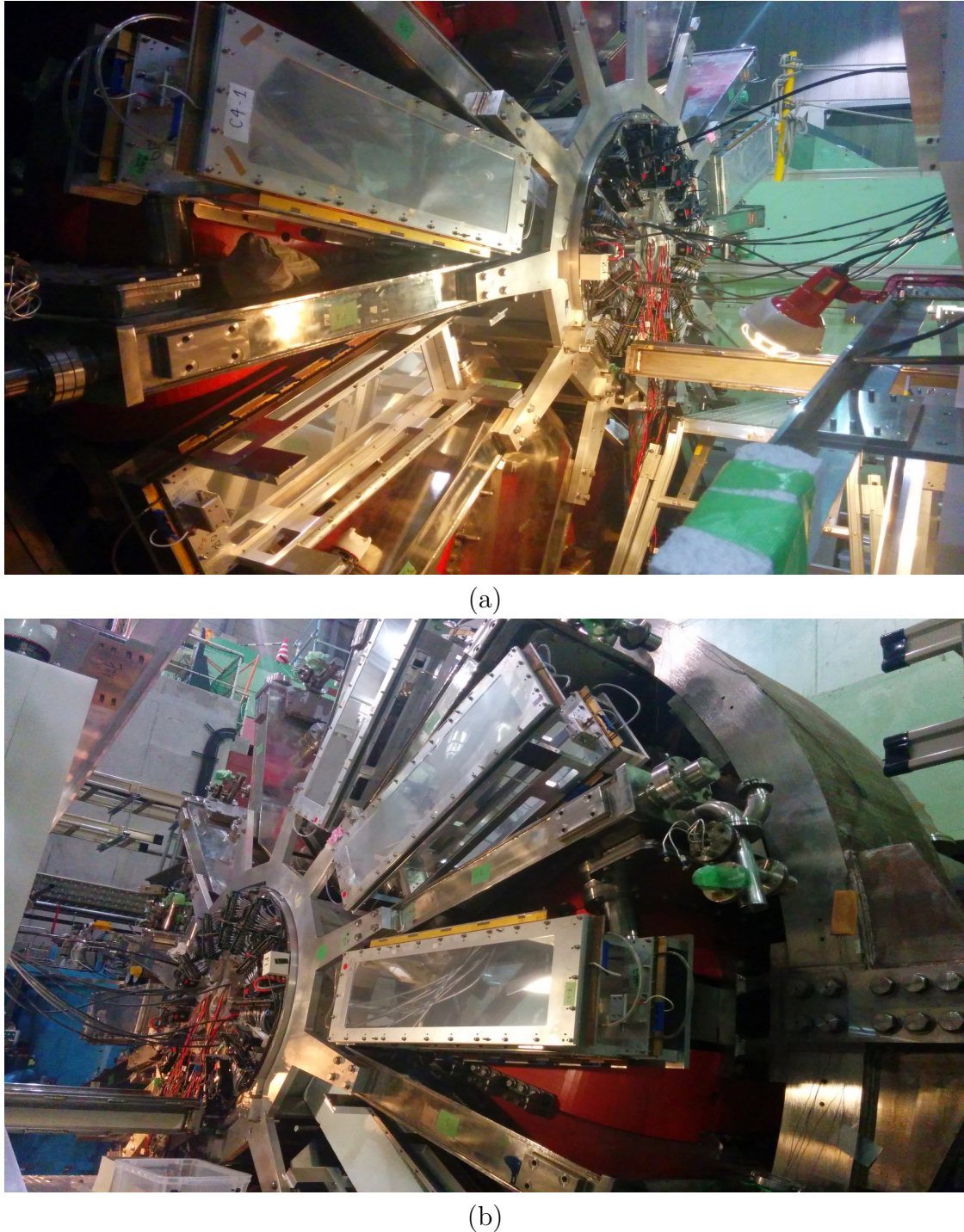


Figure B.15. Installed C3 and C4 chambers into gaps 1, 2, 3 and 9.

base plates with respect to the magnet pole faces. Following the installation of the

MWPC base plates, C3 chambers were installed into gaps 10, 11 and 12 [123]. A C4 chamber was installed into gap 12 [123].



Figure B.16. A PMT attached to the upstream of a GV counter.

B.12 Installation Day 12

On this day installation of a C3 chamber into gap 10 was completed and C4 chambers were installed into gaps 10 and 11. This brought the total number of installed C4 chambers to seven; and correspondingly the total number of installed C3 chambers to nine. Installation of the C3 and C4 chambers in gaps 5, 6 and 7 was halted in order to avoid damaging them, because they were closer to the floor level of the experiment area, and other tasks were being performed in concert. Below figure B.17 shows the results of C3 and C4 chamber installations.

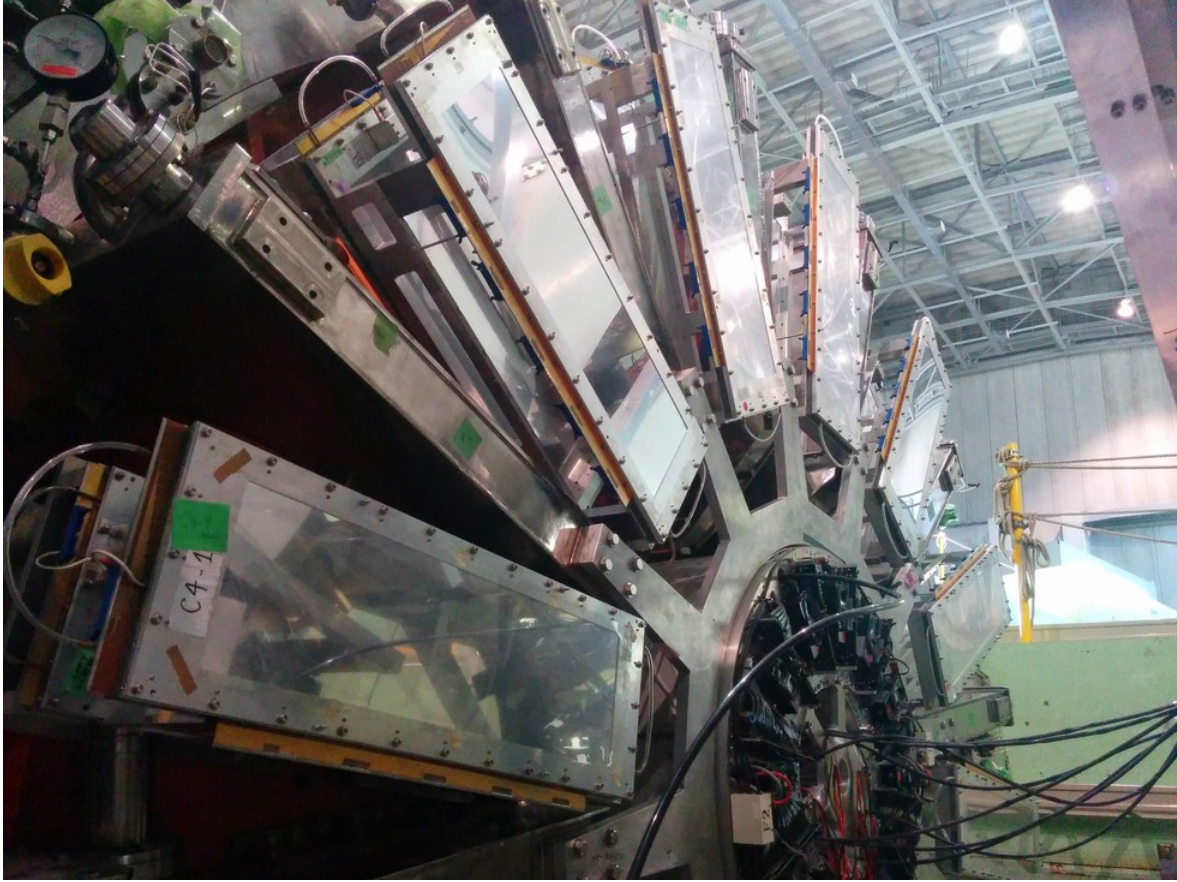


Figure B.17. Results of C3 & C4 installation, as of Dec 22. 2014, showing 7 installed C4s. This completes installation of C3 & C4 for the time being.

Assembly of TOF2 support frames was started and several TOF2 outside support plates were assembled and mounted onto the PGC-wheel [123]. These support plates differed from those used for gaps 5, 6 and 7. This is because the gap 5, 6 and 7, TOF2 counters were perpendicular to their respective PMTs and were shorter in length in comparison to the other counters [123]. Figure B.18 shows progress the of mounting TOF2 frame support plates onto the PGC-wheel [123].



Figure B.18. Installation of TOF2 outside support plates and several inside support plates as of Dec 22. 2014.

VITA

Dongwi Handiipondola Dongwi

bishoy.dongwi@gmail.com

Education

Doctor of Philosophy (August 2020)
Physics
Hampton University

Bachelor of Arts (May 2010)
Physics, Mathematics & Biochemistry
Westminster College

Honors and Awards

1. 1st Place: Emerging Researchers National (ERN) Conference Graduate Oral Presentation, Washington DC, February 2018
2. Winner: Electromagnetic Interactions with Nucleons and Nuclei (EINN) Poster Presentation, Paphos, Cyprus, November 2017

Publications and Presentations

1. “The stopped K^+ decay experiment TREK/E36 at J-PARC”
Colloquium - Lawrence Livermore National Laboratory, Livermore CA. (January 28, 2020)
2. “The stopped K^+ decay experiment TREK/E36 at J-PARC”
Presentation - American Physical Society, Division of Nuclear Physics, Arlington VA. (October 16, 2019)
3. “The stopped K^+ decay experiment TREK/E36 at J-PARC”
Colloquium - Thomas Jefferson National Accelerator Facility. (September 4, 2019)
4. “Dark Matter: Searching for light neutral bosons with Experiment E36 at J-PARC”
Colloquium - Science Day (Middle School Students), Ashburn VA. (May 4, 2019)
5. “Search for light neutral bosons in the experiment E36 at J-PARC”
Presentation - American Physical Society, Denver VA. (April 14, 2019)
6. D. H. Dongwi, Notes on post amplifier studies for E36, TREK/E36 technical note (2014).
7. D. H. Dongwi, Notes on post amplifier studies for E36, TREK/E36 technical note (2014).
8. D. H. Dongwi, Notes On E36 Detector Installation Process, TREK/E36 technical note (2014).
9. D. H. Dongwi, Momentum bite and target scan with Geant4 simulation, TREK/E36 technical note (2015).